

## INFORMATION TO USERS

This manuscript has been reproduced from the microfilm master. UMI films the text directly from the original or copy submitted. Thus, some thesis and dissertation copies are in typewriter face, while others may be from any type of computer printer.

**The quality of this reproduction is dependent upon the quality of the copy submitted.** Broken or indistinct print, colored or poor quality illustrations and photographs, print bleedthrough, substandard margins, and improper alignment can adversely affect reproduction.

In the unlikely event that the author did not send UMI a complete manuscript and there are missing pages, these will be noted. Also, if unauthorized copyright material had to be removed, a note will indicate the deletion.

Oversize materials (e.g., maps, drawings, charts) are reproduced by sectioning the original, beginning at the upper left-hand corner and continuing from left to right in equal sections with small overlaps. Each original is also photographed in one exposure and is included in reduced form at the back of the book.

Photographs included in the original manuscript have been reproduced xerographically in this copy. Higher quality 6" x 9" black and white photographic prints are available for any photographs or illustrations appearing in this copy for an additional charge. Contact UMI directly to order.

# UMI

A Bell & Howell Information Company  
300 North Zeeb Road, Ann Arbor MI 48106-1346 USA  
313/761-4700 800/521-0600



RICE UNIVERSITY

# Dynamics of Relativistic Electrons during Magnetic Storms

by

Hee-Jeong Kim

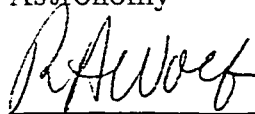
A THESIS SUBMITTED  
IN PARTIAL FULFILLMENT OF THE  
REQUIREMENTS FOR THE DEGREE

Doctor of Philosophy

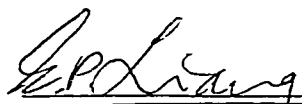
APPROVED, THESIS COMMITTEE:



Dr. A. A. Chan, Director  
Associate Professor of Space Physics &  
Astronomy



Dr. R. A. Wolf  
Professor of Space Physics & Astronomy



Dr. E. Liang  
Professor of Space Physics & Astronomy



Dr. M. Cottrill  
Professor of Physics

Houston, Texas

April, 1999

UMI Number: 9928550

---

UMI Microform 9928550  
Copyright 1999, by UMI Company. All rights reserved.

This microform edition is protected against unauthorized  
copying under Title 17, United States Code.

---

**UMI**  
300 North Zeeb Road  
Ann Arbor, MI 48103

## Abstract

# Dynamics of Relativistic Electrons during Magnetic Storms

by

Hee-Jeong Kim

Our society increasingly relies on spacecraft operations in the Earth's inner magnetosphere, particularly for communications. Long-duration high-intensity fluxes of relativistic electron are hazardous to spacecraft operational systems. Adverse effects of these energetic electrons on spacecraft has resulted in significant public interest and renewed efforts to advance our understanding and predictive capabilities of relativistic electron flux variations in the inner magnetosphere.

The flux variations are especially dynamic during geomagnetically disturbed times. It is often observed that fluxes of relativistic electrons in the Earth's inner magnetosphere decrease by orders of magnitude, followed by a substantial enhancement of up to two orders of magnitude above the pre-storm levels. This work primarily focuses on the investigation of two physical processes for the relativistic electron flux variations: The *fully-adiabatic* effect and the *delayed substorm injection* mechanism. We simulate fully-adiabatic variations of electron fluxes for the special case of equatorially mirroring electrons using Rice magnetic field models and a quiet-time electron flux model. The storm-time electron fluxes can be obtained by fully-adiabatically evolving pre-storm fluxes using Liouville's theorem. Our study shows that the fully-adiabatic effect can cause a flux decrease of up to almost two orders of magnitude for  $Dst = -100$  nT. We also simulate acceleration and injection of plasma sheet electrons during substorm dipolarization using a 3-D MHD field model. The test particle simulation shows that tens-of-keV plasma sheet electrons may be accelerated up to relativistic energies during a rapid substorm injection followed by a slow radial diffusion to the inner magnetosphere. Comparison with measurements shows that the mechanisms may contribute significantly to the observed flux variations.

## Acknowledgments

I would like to thank all of my committee members for their intellectual guidance and precious inputs in bringing this thesis to the world.

There are no words that can deliver how grateful I am to my advisors, Dr. Chan and Dr. Wolf for their invaluable encouragements and supports. It was my honor to have them as my advisors not only for the research, but also for my life.

Special thanks go to Don Brautigham for providing me with the CRRES data and Geoff Reeves for LANL data. I am indebted to Joachim Birn for his letting me use his model and numerical codes and for helpful discussions. I am also very grateful to Dr. Weisheit, Dr. Reiff, Dr. Liang, Dr. Freeman, and all other professors for their affectionate cares and supports.

My years at Rice has been such a joyful and memorable period of my life. It is all because I have been with my dear fellow graduate students and friends like Dana, David, Trevor, Dechun, Andrew, Parviz, Cindy, Tony, and Markus, Karen, Matthew Hei, and all others who have shared the years with me. Marie, Umbe, Norma, and Maria have helped me in countless ways in having finished up the Rice years successfully. I must thank all my Korean fellows who offered me so many supports and helps.

This dissertation is dedicated to my beloved family: my parents who have believed in me, my husband who has given the endless love and support, and my son who became a joy of my life.

# Contents

Abstract	ii
Acknowledgments	iii
<b>1 Introduction</b>	<b>1</b>
1.1 Motivation and objectives . . . . .	1
1.2 Observations of relativistic electron flux variations . . . . .	6
1.3 Physical mechanisms . . . . .	13
<b>2 Fully-adiabatic flux changes</b>	<b>21</b>
2.1 Introduction . . . . .	21
2.2 General description of fully-adiabatic response . . . . .	24
2.3 Adiabatic transformation of quiet-time electron flux . . . . .	28
2.4 Magnetic field models . . . . .	30
2.5 Quiet time electron flux profile . . . . .	36
<b>3 Simulation of the storm main phase flux decrease</b>	<b>42</b>
3.1 Calculation of fully-adiabatic electron flux variations . . . . .	42
3.2 Fluxes for an artificial storm . . . . .	45
3.3 Comparison with flux measurements . . . . .	49
3.4 Summary and discussion . . . . .	59
<b>4 Delayed substorm injection mechanism</b>	<b>62</b>
4.1 Introduction . . . . .	62
4.2 What is the delayed substorm injection mechanism? . . . . .	64
4.3 The resistive MHD field model . . . . .	67
4.4 The particle tracer . . . . .	70
<b>5 Results for the substorm injection mechanism</b>	<b>78</b>
5.1 Characteristics of sample electron orbits . . . . .	78

5.2	Estimation of the number of relativistic electrons generated in a substorm . . . . .	86
5.3	Summary and Discussion . . . . .	97
6	<b>Summary and Discussion</b>	<b>99</b>
	<b>Bibliography</b>	<b>102</b>

# Chapter 1

## Introduction

### 1.1 Motivation and objectives

In a world increasingly dependent on satellite operations, it has become well recognized that space environmental changes, so called “space weather”, outside the atmosphere can have serious effects on technology in space and in particular on communications. Changes in the magnetospheric populations of highly energetic particles is one of the leading areas of space weather research.

Two major particle populations in the inner magnetosphere are *ring current particles*, which are predominantly ions of a few hundred keV in energy, and *relativistic electrons* of energies  $\gtrsim 0.5$  MeV. It has been found that the magnetically trapped relativistic electrons consist normally of two zones of intense fluxes — the inner radiation belt (from the ionosphere to  $\sim 2R_E$  in the equatorial plane) and the outer radiation belt ( $3 \sim 8R_E$ ). The relativistic electrons in the outer radiation belt are weakly confined to the magnetic equatorial plane [Spjeldvik and Rothwell, 1985] and they exhibit large intensity fluctuations, especially during geomagnetically active times.

Many studies have been devoted to understanding the dynamical processes that drive the large variability of the outer radiation belt relativistic electrons, but it is still a major unsolved problem in magnetospheric physics, arguably one of the most important, particularly from the point of view of space weather. Understanding the mechanisms behind the flux variations is the main motivation for this thesis.

Geomagnetic activity is controlled by solar wind conditions, such as solar wind speed, number density, and orientation and strength of the interplanetary magnetic field (IMF) [e.g., Nishida, 1983]. A high solar wind density and an increase of solar wind speed can produce a sudden, dramatic increase in solar wind dynamic pressure. This compresses and greatly distorts the Earth’s magnetosphere. Combined with strong southward IMF, these changes can drive intense geomagnetic activity, such as magnetic storms and substorms. Abrupt enhancements of relativistic electron inten-

sity, so called “relativistic electron events”, often occur during such geomagnetically disturbed times.

An example of a relativistic electron event is shown in Figure 1.1, which displays relativistic electron flux variations at geosynchronous orbit for the storm of November 1–10, 1993 and the corresponding *Dst* values. The *Dst* index, constructed from magnetograms from all over the world, describes the average effect of storm-time magnetic field variations. This plot shows that electron fluxes for all four energy channels *decrease* by orders of magnitude as a magnetic storm develops, then *increase* to peak levels about  $10$ – $10^2$  times the pre-storm fluxes during the recovery phase, and then gradually decrease to the pre-storm level [Baker *et al.*, 1986, 1989; Williams, 1966].

Recently, great interest in the relativistic electron events has resulted from the observation that the large sustained enhancements of relativistic electron flux are linked to serious spacecraft functional anomalies [Baker *et al.*, 1994b; Gussenhoven *et al.*, 1991]. A high intensity of relativistic electron flux can damage sensitive electronic components of operational satellites through electric discharges which occur as a consequence of a process known as deep dielectric charging. The relativistic electrons linked to such spacecraft failures are often informally called *killer electrons*. Figure 1.2 illustrates how a high intensity of relativistic electrons can cause deep dielectric charging in insulators in spacecraft electronics.

For instance, in January 1994, enhanced fluxes of energetic electrons caused anomalies in three Canadian geosynchronous communications satellites, Intelsat-K, Anik E-1, and Anik E-2 (see Figure 1.3). All three suffered a loss of altitude control caused by a failure in their momentum wheel circuitry. Although none suffered permanent damage, television, radio, telephone, and satellite operations were affected for hours to days.

Showers of highly energetic electrons can also deliver heavy doses of radiation to humans who may be walking in space during an electron storm. Therefore the ability to forecast “space weather” has important health implications for astronauts and may have a significant effect on the men and women who will work in space to build the international space station. Overall, improved understanding and predictive

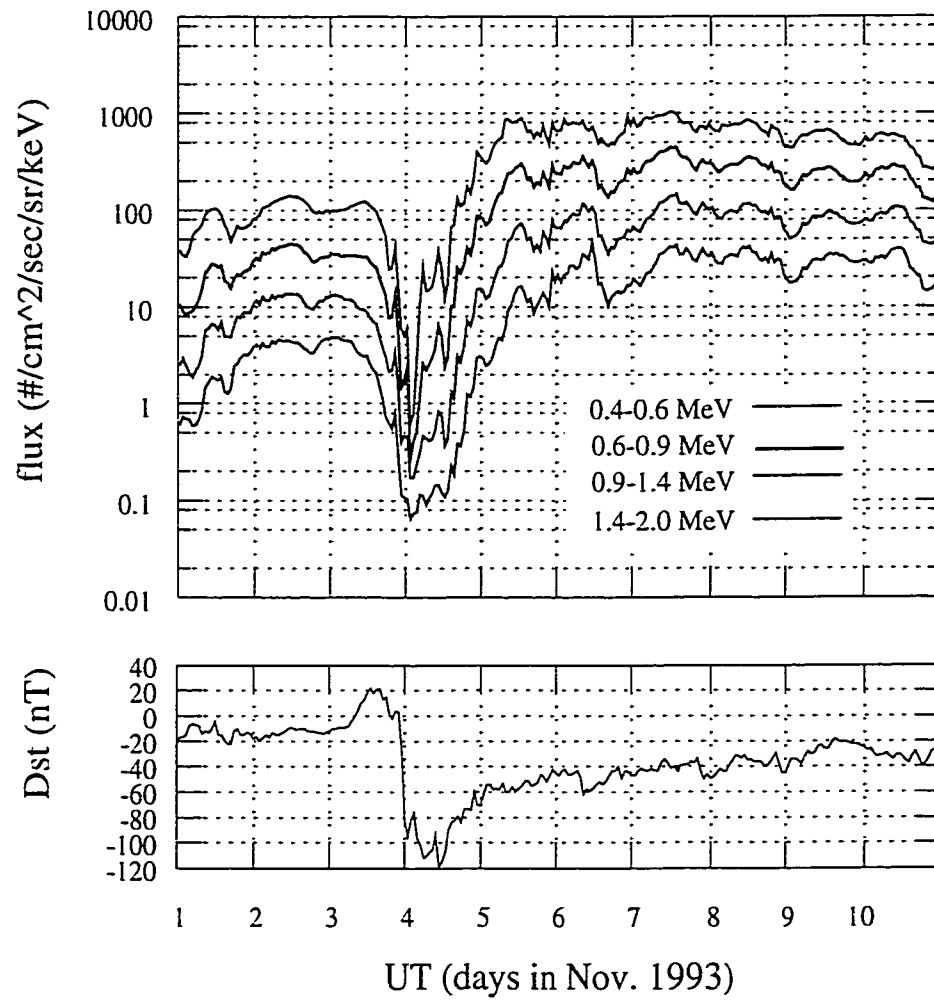


**Figure 1.1** Electron differential flux for November 1–10, 1993 measured by Los Alamos National Laboratory geosynchronous spacecraft SC 1984-129 (LT = UT+0.54), and corresponding  $Dst$  values.

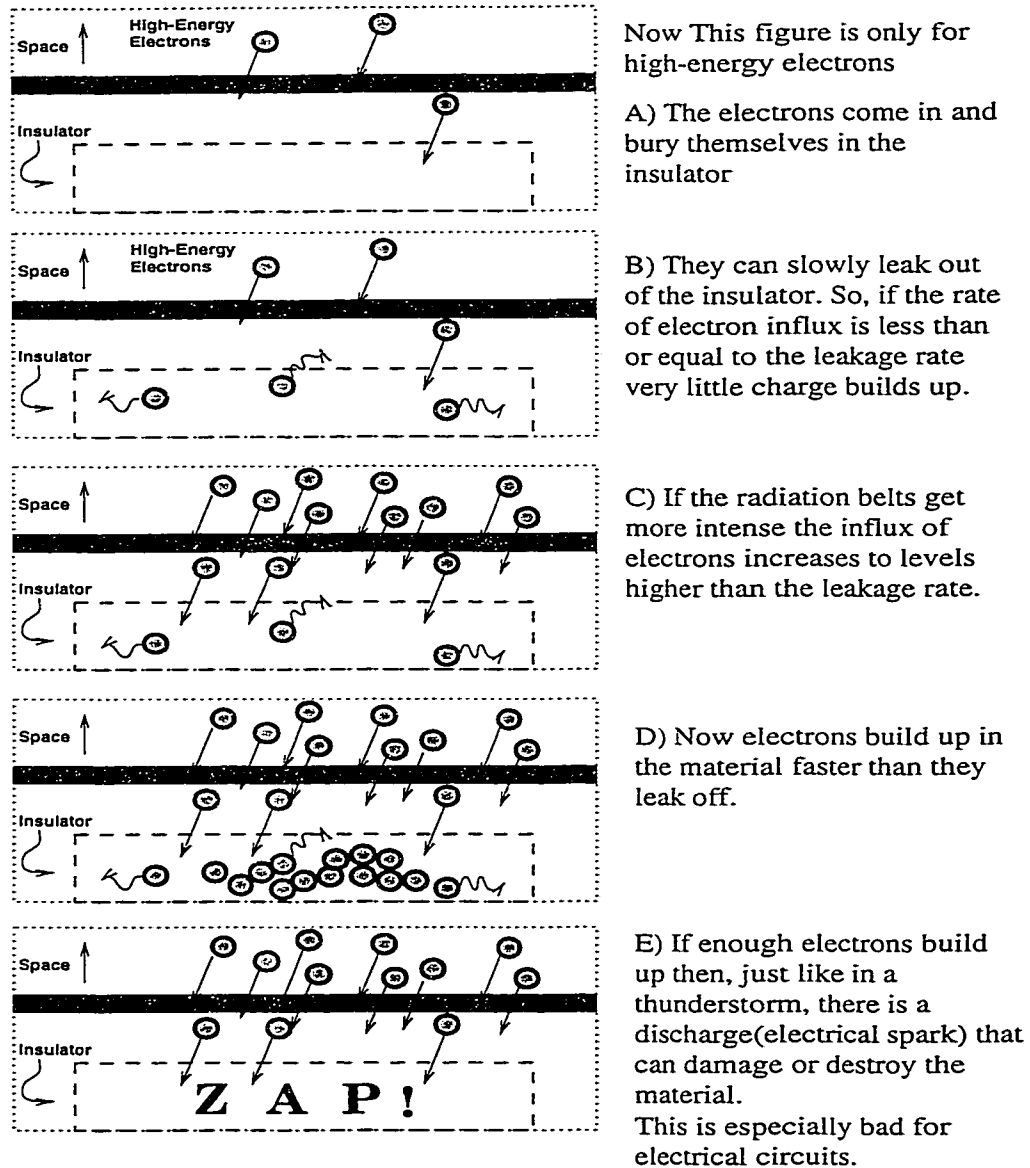


**Figure 1.2** This schematic illustrates how a high intensity of relativistic electrons can cause a deep charging effect in spacecraft electronics. Electrical discharges resulting from the charge buildup can lead to serious damage on spacecraft electronic systems (adapted from the ISTP web site (<http://www-istp.gsfc.nasa.gov/istp/news/9812/image.html>)).

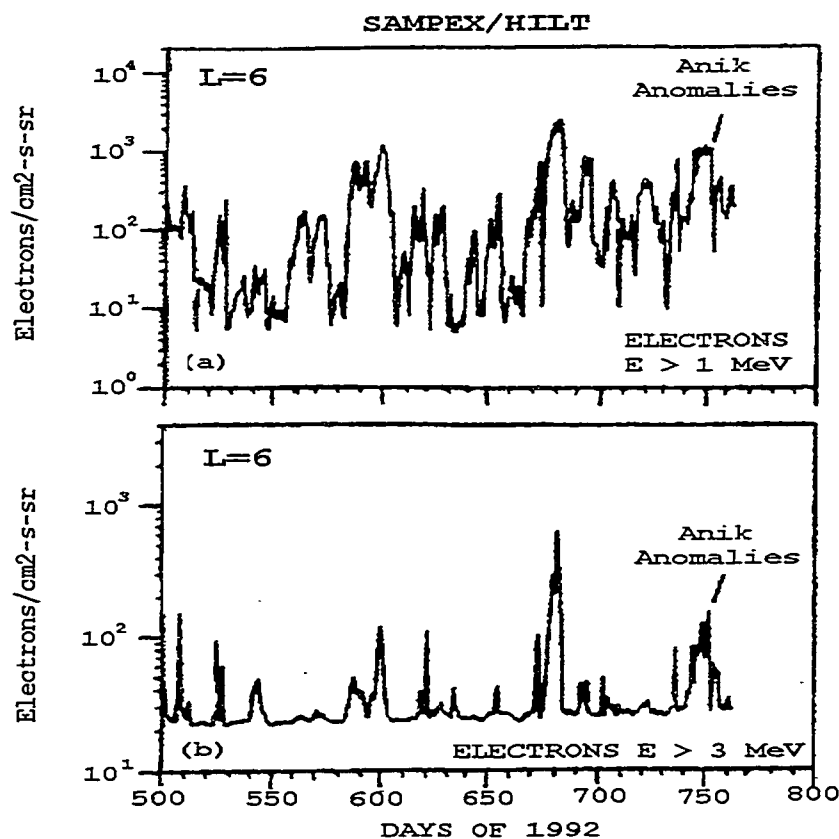


**Figure 1.3** Daily averages of electron flux measurements at  $L = 6$  (a) for  $E > 1$  MeV and (b) for  $E > 3$  MeV from SAMPEX spacecraft. The period covered is day 500 of 1992 to day 763. In the 1992 day-of-year scheme, January 20 1994 is day 751. It is evident that the Anik/Intelsat problem occurred when electrons for  $E > 1$  MeV and  $> 3$  MeV were near their highest values (adapted from *Baker et al.* [1994b]).

capabilities of relativistic electron flux variations can help satellite operators and astronauts prepare for the potential effects these events may have on space systems.

Motivated by their practical importance as well as by academic interest, it has recently become a hot topic in radiation belt physics to understand, specify, and forecast relativistic electron events.

The primary objective of the work described in this thesis is to advance our understanding of the physical processes responsible for the loss, energization, and transport of relativistic electrons in the outer radiation belt. We have mainly investigated two physical mechanisms: the *fully-adiabatic* effect and the *delayed substorm injection* mechanism. We simulate the fully-adiabatic response of relativistic electron flux using Rice magnetic field models and a quiet-time electron flux model. The delayed substorm injection mechanism is investigated using test particle simulation of plasma sheet electrons during substorm dipolarization using a 3-D MHD field model.

The following sections briefly review some of the observed characteristics of relativistic electron flux variations and discuss other physical mechanisms which have been suggested for the flux decreases and increases.

## 1.2 Observations of relativistic electron flux variations

### Classes of relativistic electron events

One can classify relativistic electron events according to the main driver of geomagnetic activity and characteristic variations of the relativistic electron intensities. The following briefly describes three classes of relativistic electron events.

#### *Events associated with high speed solar wind streams (or “one-day” relativistic events)*

It has often been observed that relativistic electron flux increases by a factor of ten or more, on a time scale of about one day at geosynchronous orbit, are often associated with recurrent high speed solar wind streams. The November 1993 storm (see Figure 1.1) is an example of this type of event. Characteristics of the electron flux variations for this event class are discussed in more detail later in this thesis (starting on page 8).

#### *Events associated with shock waves*

More rapid flux enhancements occur in the outer magnetosphere, as well as at lower radial distances. On March 21, 1991 the CRRES satellite observed the creation of a new ultra-relativistic ( $E > 15$  MeV) electron radiation belt. The new belt was produced in a few minutes in response to an interplanetary shock which propagated through the magnetosphere [Blake *et al.*, 1992; Li *et al.*, 1993; Hudson *et al.*, 1997]. It has recently been established that such rapid enhancements (in a matter of minutes) of energetic electron flux are associated with strong compression of the magnetosphere by fast interplanetary shocks [Li *et al.*, 1993, 1996] or by sudden interplanetary pressure pulses [Li *et al.*, 1998; Hudson *et al.*, 1998]. Such magnetic compressions can produce strong induced electric fields which can quickly energize electrons in the magnetosphere by moving them into stronger magnetic fields in a fraction of their drift periods.

#### *Events associated with coronal mass ejections (CMEs)*

Another class of events discovered more recently are associated with large non-recurrent geomagnetic storms which develop as a result of “coronal mass ejections”. These events are more likely to occur near solar maximum. At these times the Sun is increasingly likely to expel large clouds of matter from its corona. These move outward from the Sun and can have speeds in excess of 1000 km/s at the location of Earth [Kahler, 1992]. The shock waves preceding such plasma structures can accelerate interplanetary particles to high energies, sometimes up to several MeV. If the shock waves and “magnetic clouds” associated with CMEs strike the Earth’s magnetosphere, they can produce a geomagnetic storm and drive particle acceleration.

The magnetic storm of January 10-11, 1997 is one example of a magnetic cloud CME event (see Figure 1.4). This event was initiated by a CME, during which relativistic electron flux was enhanced after a long period of steady southward interplanetary magnetic field and following the arrival of a solar wind pulse [Baker *et al.*, 1998a]. This event seems to be linked to the catastrophic failure of a \$200 million AT&T communications satellite. In contrast to the slower (one-day) acceleration of relativistic electrons in the high speed stream associated events, the January 10-11, 1997 event demonstrated more rapid enhancements of relativistic electron fluxes

deeper in the magnetospheric trapping region.

This thesis focuses primarily on the “one-day” events. These events are arguably the most important for space weather applications because they are long-lasting and they are most likely to produce deep dielectric charging, as shown in Figure 1.2. They are also the least-well understood from a theoretical view point.

### Characteristics of “one-day” relativistic electron flux variations

We now summarize further characteristics of relativistic electron flux variations which occur on one-day time scales.

#### *Correlation with Solar Cycle*

Large, persistent increases in the relativistic electron population are found to be relatively infrequent (about 3–4/year) and sporadic around solar maximum, but more frequent (about 10–20/year) during the transition from solar maxima to solar minima [Baker *et al.*, 1986]; i.e., in the declining phase of the solar cycle.

Paulikas and Blake [1976,1979] suggested that high-energy electrons at synchronous orbit were modulated by passage of a sector boundary of the interplanetary magnetic field (IMF). However, subsequently it was found that the solar wind high-speed stream structures are better correlated with the electron flux increases. Specifically, during the transition period from solar maximum to solar minimum a prominent feature on the sun is the presence of solar coronal holes, regions of effectively ‘open’ magnetic flux which allow the solar wind to flow away from the sun at high velocities. When the coronal holes approach the solar equator the high speed stream ( $V_{sw} \gtrsim 600$  km/s) can lie in the ecliptic plane and can impact the Earth’s magnetosphere, initiating geomagnetic storms and often resulting in relativistic electron events.

#### *27-day periodicity*

Coronal holes rotate with the sun so they can produce high-speed streams in the solar wind which reappear with the 27-day solar rotation period. It has been observed that relativistic electron enhancements are well associated with the recurrent high

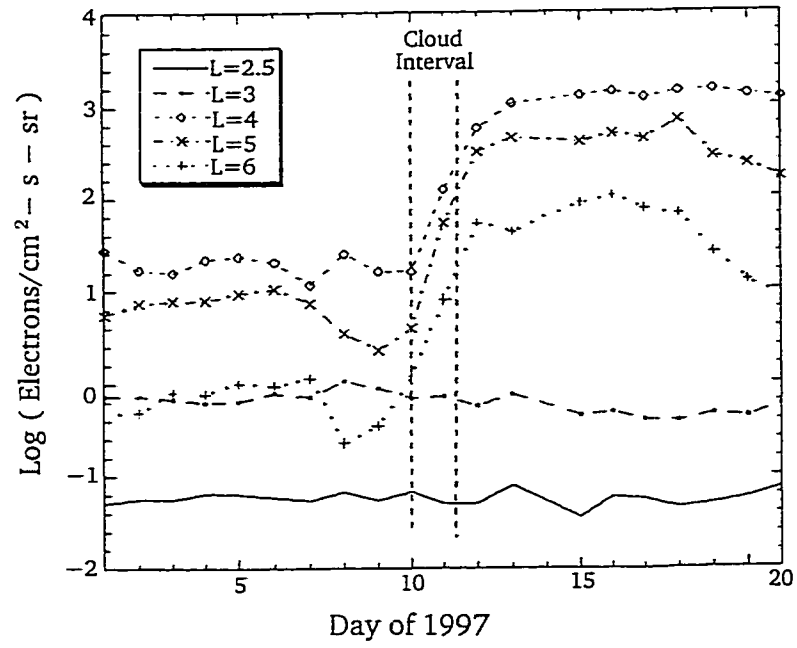


**Figure 1.4**  $L$ -sorted electron fluxes measured at low altitudes by SAMPEX instrumentation (2–6 MeV) for 1–21 January, 1997. A strong electron enhancements occurred during the cloud interval (adapted from *Baker et al.* [1998b]).

speed streams and they also occur with the regular 27-day periodicity during the transition period from solar maximum to solar minimum [Baker *et al.*, 1986].

Figure 1.5 shows the daily average of the counting rates in the 5 to 7 MeV energy channel for the time period from June 1979 to the end of October 1984. Note the strong contrast between the count rate prior to 1981 and afterward: numerous large flux increases were seen beginning in 1981, while only small, weak flux increases are seen prior to 1981. Another striking feature is the 27-day periodicity of the flux increase occurrence. This is very clearly seen in the 1982-1984 time period – see the small inset panel with the 27-day tick marks referenced to a large event (marked by the asterisk) which occurred in July 1984. Yearly averaged sunspot numbers are plotted in Figure 1.6 for reference.

#### *Correlation with Dst*

Reeves *et al.* [1998] examined the relationship between relativistic electron enhancements at geosynchronous orbit and magnetic storms, as measured by the *Dst* index. By correlating the maximum electron flux in each event with the minimum *Dst* value they found the maximum relativistic electron fluxes and maximum ring current intensity are roughly correlated but that there is considerable variation. While the correlation between the strength of a magnetic storm and the strength of the relativistic electron event is relatively low, the relativistic electron events were *only* observed during magnetic storms. Therefore, while one can conclude that the mechanism responsible for accelerating the relativistic electrons is not the same as the process that injects particles into the ring current, one can also conclude that the two processes act at nearly the same time.

On the shorter time scale of days, comparisons between relativistic electron fluxes and *Dst* variations shows that there is a strong similarity between the temporal variations of the *logarithm* of the electron fluxes and changes in *Dst*. See Figure 1.1 and Nagai [1988] for examples of this effect.

#### *Lifetimes*

Baker *et al.* [1986] made a superposed epoch analysis using data from geosynchronous spacecraft SC 1979-053 and SC 1982-019 and showed that energetic electron

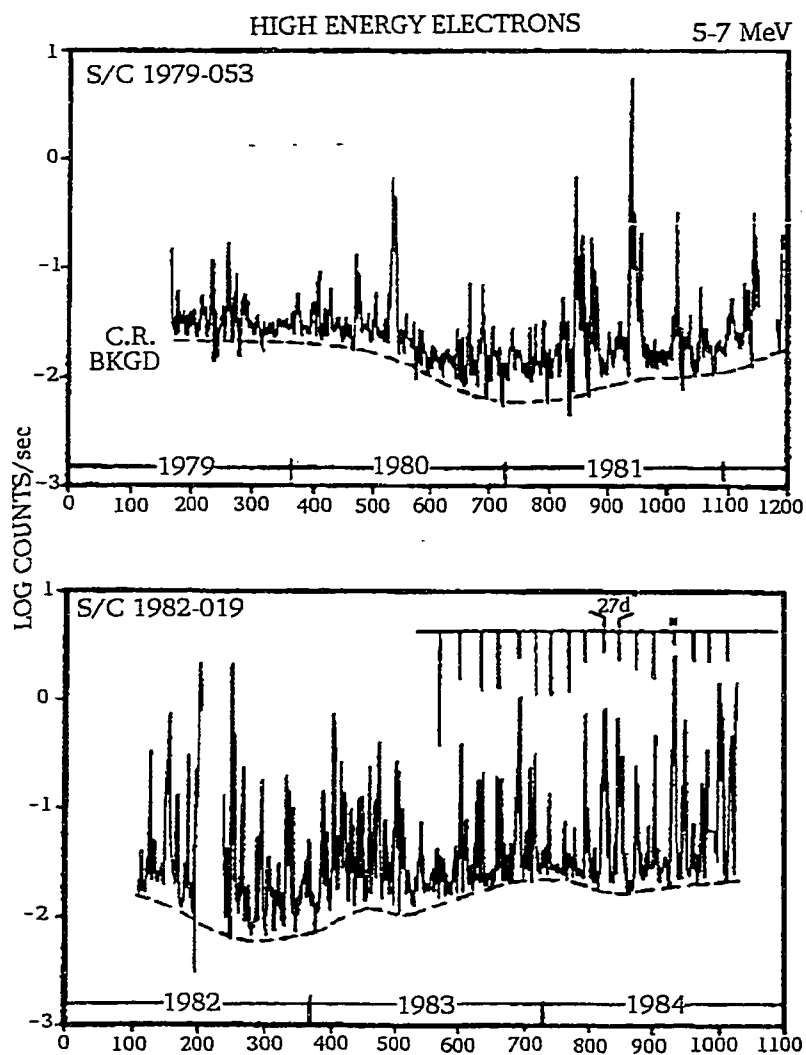


**Figure 1.5** High energy electron (5–7 MeV) daily count rate averages from June 1979 through October 1984. Data are from nearly identical instruments on board geosynchronous spacecraft 1979-053 (top panel) and 1982-019 (bottom panel). Note the periodic intensity enhancements illustrated by the inset in the right panel. The dashed line labeled ‘C.R. BKGD’ is the background counting rate due to galactic cosmic rays (adapted from *Baker et al.* [1986]).

( $> 3\text{MeV}$ ) fluxes at geosynchronous orbit typically rise on a 2–3 day time scale and decay back to prior levels on a 3–4 day time scale. Full width at half maximum time scales for typical events are  $\sim 2.5$  days. They concluded that average particle lifetimes and rise and decay time scales seem to be invariant as a function of time within the solar cycle. The geosynchronous observation of the high speed stream associated events showed that the relativistic electron fluxes tended to peak 2–3 days after the passage of the solar wind disturbance and the initial injection of an energetic (a few tens to hundreds keV) electron population [e.g., *Paulikas and Blake, 1979*].

### *Radial dependence*

*Williams et al.* [1968] observed that the  $L$ -values (i.e., the radial locations measured in Earth radii) where the large enhancements of relativistic electron flux initially appear decreases with decreasing  $Dst$  minimum. They also found that the energetic electrons associated with magnetic storms are observed to appear initially at  $L$  values well within the trapping regions and subsequently diffuse to lower and higher  $L$ .

*Baker et al.* [1994a] performed a superposed epoch analysis for eight energetic electron events from SAMPEX observations for July 1992 through July 1993. They showed that the energetic electron fluxes rise on a time scale of 1–2 days or less for  $2.5 \leq L \leq 5$ , being most abrupt for  $L \sim 3$ . The decay of the energetic electron fluxes is energy and  $L$  dependent and is exponential with a decay constant of 5 to 10 days. For a particular event for the November 1993 storm, *Li et al.* [1997b] showed from SAMPEX observations that the electron flux decreases occur at all  $L$ -values between 3 and 8 and the flux increases occur first at  $L = 4$ , followed by  $L = 3$  and  $L = 5$  at about the same time. *Hilmer and Ginet* [private communication, 1999] found that the phase space density increases at  $L = 6.6$ , then at  $L = 4$ , for almost all of the events studied.  $L$ -dependencies, however, exhibit relatively strong variability among relativistic electron events.

We have summarized some of the observed features of relativistic electron flux variations. One should note, however, that not all of the relativistic electron events fit neatly into the above categories. There is still a great deal of work remaining in order to fully characterize the observations of relativistic electron flux variations during

magnetic storms. Much work also remains to understand the physical mechanisms responsible for the observed variations.

### 1.3 Physical mechanisms

We now briefly discuss some of the physical mechanisms which may contribute to the observed main phase flux decrease and the large flux enhancement for the storm recovery phase.

#### Mechanisms for the flux decreases

Mechanisms which have been proposed for the flux decreases include:

- Loss by pitch-angle scattering into the atmospheric loss cone.

*Thorne and Kennel* [1971] suggested that pitch angle scattering by electromagnetic ion cyclotron waves may drive precipitation of relativistic electrons to the atmosphere. There is some observational support for this mechanism [*Vampola*, 1971]; however often there is no clear sign of enhanced precipitation leading to the observed flux decreases [Li 1996, personal communication].

- Loss by particle drift motion to the magnetopause.

Large scale changes in the magnetospheric configuration may cause previously-trapped particles to drift into the magnetopause and be lost. In some cases the dayside magnetopause is compressed and moved inside geosynchronous orbit, resulting in the magnetopause loss of relativistic electrons which (before the compression) drifted in the closed path near geosynchronous orbit.

- Fully-adiabatic flux changes (also known as the *Dst effect*).

There are three adiabatic invariants, associated with particle motion in a magnetic field. They are  $\mu(= p_{\perp}^2/2mB)$  for gyromotion about the magnetic field,  $J(= \oint p_{\parallel} ds)$  for bounce motion along the field line, and  $\Phi$  (the magnetic flux linked by the particle drift orbit) for drift motion about the source of the field. All three adiabatic invariants are conserved in this mechanism, and particles

move radially and change energy due to changes in the magnetic field configuration. When changes in the magnetic field are slow compared to the particle drift period, the particle drifts outward or inward in order to conserve the third adiabatic invariant. Because of gradients in the particle phase-space density the number of electrons that are detected in a given energy channel by a geosynchronous spacecraft typically decreases during the storm main phase. This mechanism will be examined in detail in the next chapter.

A combination of these three loss mechanisms seems to contribute to the observed flux decreases. In cases of strong magnetic activity, for which some of the closed drift path of relativistic electrons become open, the loss to the magnetopause becomes significant. On the other hand, the fully-adiabatic effect always makes a contribution to some extent, as long as the magnetic field changes are slow compared to the particle drift period.

### Mechanisms for the flux increases

Mechanisms which have been proposed for the flux increases can be divided into two categories, depending on whether the energy source is *external* or *internal* to the magnetosphere. Energetic solar wind particles and Jovian electrons can be the external sources for the relativistic electrons in the inner magnetosphere. Figure 1.7 illustrates the heliospheric transport of Jovian electrons to the inner part of the solar system and also illustrates the possible recurrent geomagnetic activity effects that could result from coronal hole structures as solar minimum is approached. More recently *Li et al.* [1997a] have shown that external sources are probably not dominant because the phase-space density of source electrons in the solar wind is too low to supply the observed flux increases.

Internal source mechanisms which have been proposed include:

- The recirculation model [*Nishida*, 1976; *Fujimoto and Nishida*, 1990].

In the recirculation model transport and energization takes place in four steps: (1) inward radial diffusion which violates the third invariant, (2) pitch angle diffusion in the inner magnetosphere which moves the particle mirror point to lower altitudes, (3) outward radial diffusion occurring on the low-altitude

portions of the field lines and conserving only the first invariant, and (4) pitch angle diffusion which isotropizes the pitch angle distribution. A schematic in Figure 1.8 illustrates these four steps. The recirculation model is qualitatively consistent with several features of the observed relativistic events. However, more work is needed to understand the mechanism, particularly on the source and nature of the low-altitude waves which are proposed to drive the outward, energy conserving diffusion.

- Cyclotron-resonant heating by whistler-mode waves.

Wave-particle interactions of electrons with whistler waves may be invoked to explain the local heating of trapped radiation belt electrons [*Temerin et al.*, 1994]. *Summers et al.* [1998] argued that a combination of energy diffusion by whistler mode chorus and pitch angle scattering by electromagnetic ion cyclotron waves could provide a viable mechanism to account for the gradual local stochastic acceleration of electrons from a few hundred keV to above 1 MeV in the outer magnetosphere ( $L \approx 4$  to  $L \approx 5$ ) during the recovery phase of a storm. However, detailed calculations including bounce-averaged rates of diffusion are required to establish the time scales for this resonant heating process. *Summers et al.* [1998] also pointed out that the electromagnetic ion cyclotron wave can provide a source of scattering loss for relativistic electrons during the main phase of a storm [*Thorne and Kennel*, 1971].

- Diffusion of trapped energetic electrons from the cusp.

*Sheldon et al.* [1998] reported that the POLAR spacecraft observed trapped MeV electrons in the Earth's cusp, and that these distributions are consistent with their simulations of trapped particles in the outer cusp region. They proposed that the particles are accelerated at the location of the outer cusp and they are potential source population for diffusion into the dipole radiation belts. However, diffusion in pitch-angle as well as in  $L$ -shell would be required to transport these particles from the outer cusp to the radiation belts, since the radiation belt pass is at a higher magnetic latitude which maps the trapped flux into the wide loss cones of the outer cusp.

- Interaction with ULF pulsations.

*Rostoker et al.* [1998] have shown that enhanced ULF wave activity is correlated with large relativistic electron flux increases in the region near geostationary orbit. They argued that the compressional waves caused by the action of the Kelvin-Helmholtz instability along the morning-side magnetopause can accelerate electrons to energies of the order of MeV in a matter of few hours. *Hudson et al.* [1998] have simulated an impulsive enhancement of relativistic electron flux on January 10, 1997, correlated with an observed increase in ULF wave activity commensurate with electron drift periods. They suggested that multiple drift-resonance between electrons and the enhanced power in the radial electric field can accelerate particles to energies from hundreds keV to MeV range [*Chan and Hudson*, 1998]. ULF wave enhancements often seem to accompany both CME-related electron events [*Baker et al.*, 1998b] and high speed solar wind stream events [*Rostoker et al.*, 1998].

- Fully-adiabatic flux increases during storm recovery phase.

A magnetic storm recovers typically on few-day time scales, which is slow compared to the drift period of relativistic electrons. Therefore the fully-adiabatic response of relativistic electrons during the recovery phase can make some contribution to the observed flux increases. However, non-adiabatic acceleration process(es) are also important to explain the sharp (faster than recovery of magnetic fields) flux enhancements observed especially in the early recovery phase.

- Delayed substorm injection.

In this mechanism electrons from the magnetotail are rapidly injected during substorm dipolarization into an outer trapped region (around  $10 R_E$ ) and are further transported to within synchronous orbit on time scales of about a day. Plasma sheet electrons with tens of keV energy can be energized substantially during the transport to the inner magnetosphere, possibly contributing to the observed enhancement of MeV electron fluxes. It has been suggested that the acceleration process may provide sufficient number of MeV electrons for an observed flux increase at geosynchronous orbit, although this number is strongly

dependent on the particle initial conditions, the plasma sheet phase-space density, and the intensity of the substorms. This mechanism will be discussed in detail in Chapters 4 and 5.

It is not yet clear which of these mechanisms are most important for explaining the observed large enhancements of relativistic electron fluxes in the inner magnetosphere. Much further theoretical and observational work is required to resolve this issue.

This thesis mainly focuses on the relativistic electron events which are associated with the recurrent high speed streams and so exhibit a relatively slow increase of relativistic electron flux (typically days after the passage of the solar wind disturbance). We investigate two fundamental physical processes: *fully-adiabatic* flux changes and the *delayed substorm injection* mechanism.

Chapters 2 and 4 give introductory information on the two mechanisms and describe the methods used in the studies. Chapters 3 and 5 present the simulation results and discuss how effectively each mechanism can contribute to the observed fluxes.

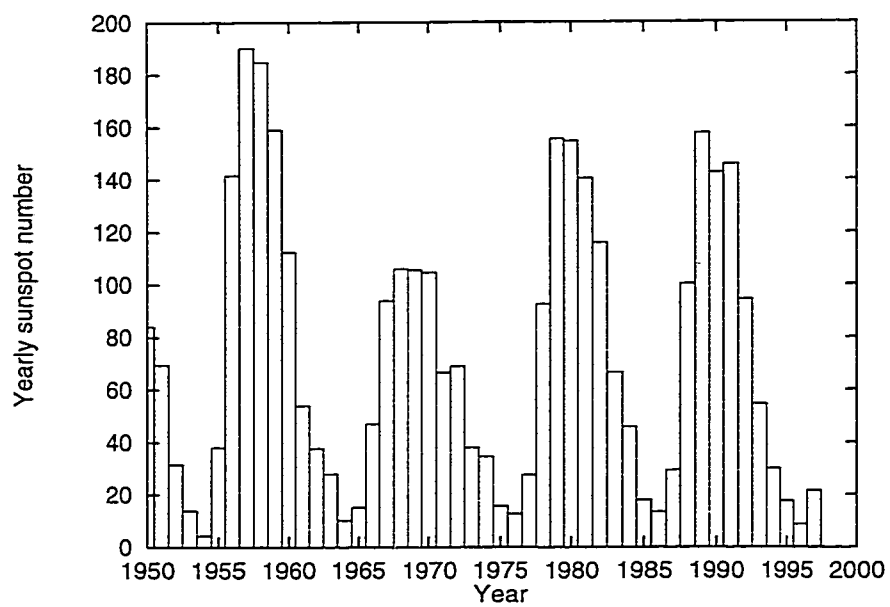


**Figure 1.6** Yearly sunspot numbers from 1950 to 1997 (Data obtained from NOAA National Geophysical Data Center). The next declining-phase period will be about year 2002 to 2007.

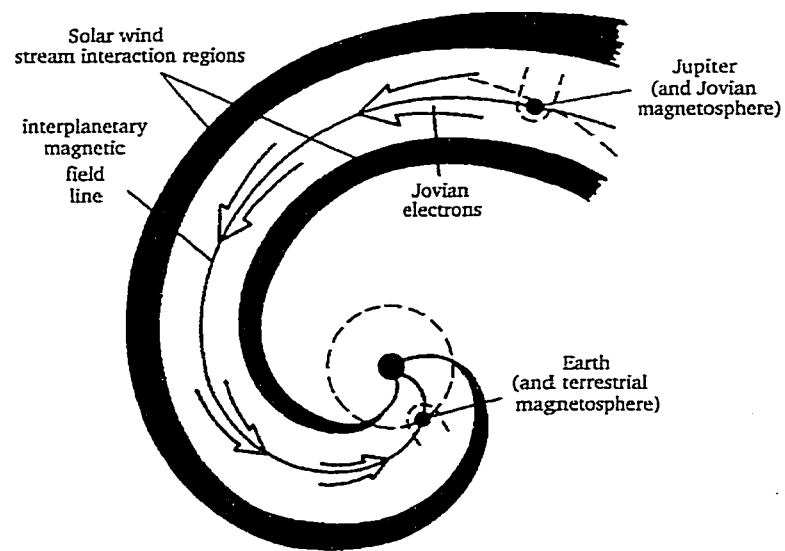


**Figure 1.7** View from above the north ecliptic pole showing the orbits of Earth and Jupiter, plus a pair of corotating interaction regions (CIR's) produced by high-speed solar wind streams (adapted from *Baker et al.* [1986]).

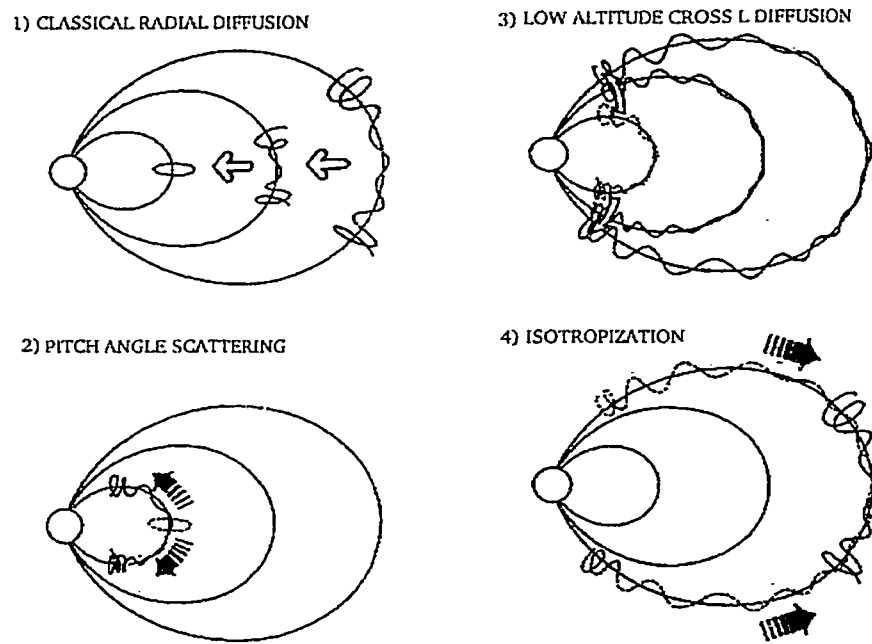


**Figure 1.8** This schematic shows the four transport processes in the recirculation model. (1) Classical inward radial diffusion, accelerating electrons and making the pitch angle distribution pancake-like. (2) Pitch angle scattering in the inner magnetosphere, lowering the particle mirror point. (3) Outward radial diffusion at low altitudes, almost conserving particle energy. (4) Isotropization of pitch angles. Adapted from *Fujimoto and Nishida [1990]*.

## Chapter 2

### Fully-adiabatic flux changes

#### 2.1 Introduction

When the coupling of the solar wind to the magnetosphere becomes strong the geomagnetic field can be significantly disturbed, often resulting in so-called magnetic storms. Studies of the spatial distribution of the disturbance of the geomagnetic field during the main phase of a storm indicate that it is nearly uniform over the entire Earth and is directed parallel to the Earth's dipole axis (i.e., southward) [e.g., *Burton et al.* [1975]]. The electric current responsible for the magnetic field disturbance is called the ring current. The ring current is primarily created by particles drifting around the Earth at distances of about 3–5  $R_E$ .

The development of a magnetic storm is usually characterized by the  $Dst$  index.  $Dst$  is a “storm-time disturbance” index constructed from a set of low-latitude magnetograms. It gives an indication of the average reduction of the horizontal component of the geomagnetic field due to the ring current. When the ring current is enhanced  $Dst$  is negative and a larger negative  $Dst$  means a more intense storm. Figure 2.1 displays a time series of the  $Dst$  index for a typical magnetic storm. A storm often begins with a sudden positive increase in magnetic field that may last for several hours. This initial phase is produced when an increase in solar-wind dynamic pressure forces the magnetopause currents closer to the earth and increases their strength. The magnetic field perturbation at the surface is northward, resulting in the positive  $Dst$  index as seen in Figure 2.1. A rapid and often highly irregular decrease in  $Dst$  is observed following the initial phase. The period of decreasing  $Dst$  is called the storm main phase. In the subsequent recovery phase,  $Dst$  recovers back to its initial value. The recovery is often rapid at first, but then slows to a time scale of 1–3 days. Storm durations are typically 1–5 days. Recovery is caused by a loss of ring current particles principally by charge exchanges with neutral hydrogen atoms. The main phase decrease in  $Dst$  is often a delayed response to an interval of strongly southward interplanetary magnetic field [*Burton et al.*, 1975].

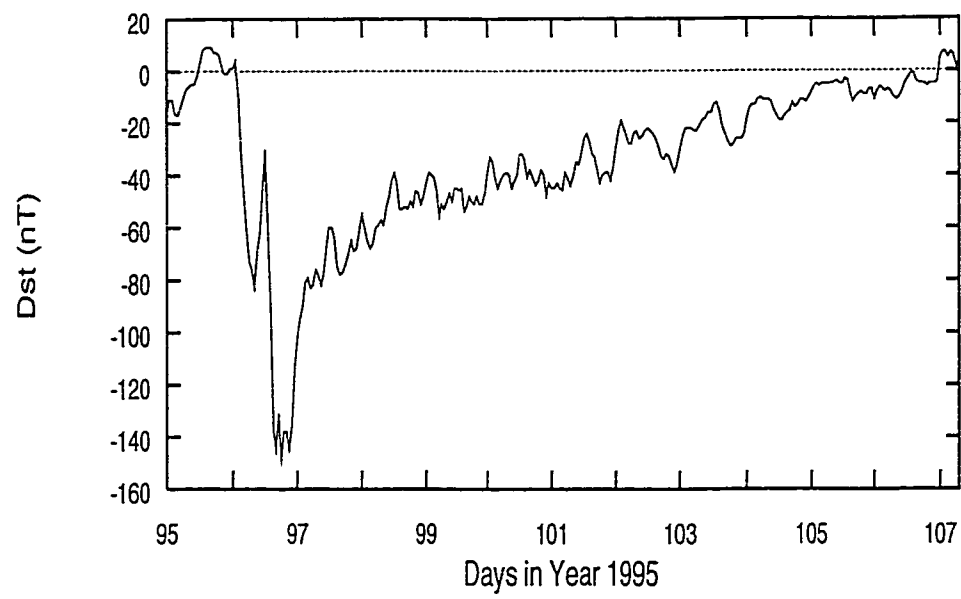


**Figure 2.1** A time series of  $Dst$  index for a magnetic storm. Data obtained from NOAA National Geophysical Data Center.

As the time scale for changes of the magnetic field configuration during magnetic storms is larger than an hour or so, high energy particles whose drift period is less than a hour may move inward or outwards conserving all three adiabatic invariants in response to magnetic configuration changes. This phenomena has been called the “*Dst* effect” or the “fully-adiabatic response”. It has been suggested that the fully-adiabatic response of relativistic electrons to changes in the storm-time geomagnetic field configuration can account for some of the observed flux variations [*Dessler and Karplus*, 1961; *McIlwain*, 1966; *Rinaldi et al.*, 1994].

*Rinaldi et al.* [1994] analyzed the storm-time energetic electron response to changes in *Dst* based on the adiabatic transformation of radial profiles and energy spectra observed between storms. They found that the adiabatic response to a model perturbed ring current magnetic field can account for from zero to 100% (but typically less than half) of the observed storm-time decrease as *Dst* decreases. Unfortunately, the CRRES electron flux data used in their study was later found to be unreliable [M. Schulz, personal communication, 1996].

The main purpose of Chapters 2 and 3 is to investigate the fully-adiabatic relativistic electron flux changes for equatorially mirroring electrons. We estimate the extent to which this effect can account for temporal variations in relativistic electron intensities observed during a magnetic storm. We also note departures of the measured fluxes from the fully-adiabatic values to help identify when non-adiabatic process are important and we seek explanations for observed features such as larger electron flux decreases for lower energies and the similarity between the variations in the *logarithm* of the electron fluxes and *Dst* changes. In this work, fully-adiabatic flux changes are calculated in a very systematic way and we are able to effectively simulate the flux variations of relativistic electrons for magnetic storms.

Section 2.2 gives a general description of the fully-adiabatic process for relativistic electrons and Section 2.3 derives the fully-adiabatic relationship between the pre-storm electron flux and the storm-time electron flux for a given energy and *L*-value. In Section 2.4 the magnetic field models are described, and in Section 2.5 a quiet-time electron flux profile,  $j(E, L)$ , is constructed from CRRES data. Chapter 3 presents simulation results of the fully-adiabatic response of storm-time electrons for

a model storm driven by an artificial *Dst* and for the November 1993 storm, including comparisons with measured electron fluxes.

## 2.2 General description of fully-adiabatic response

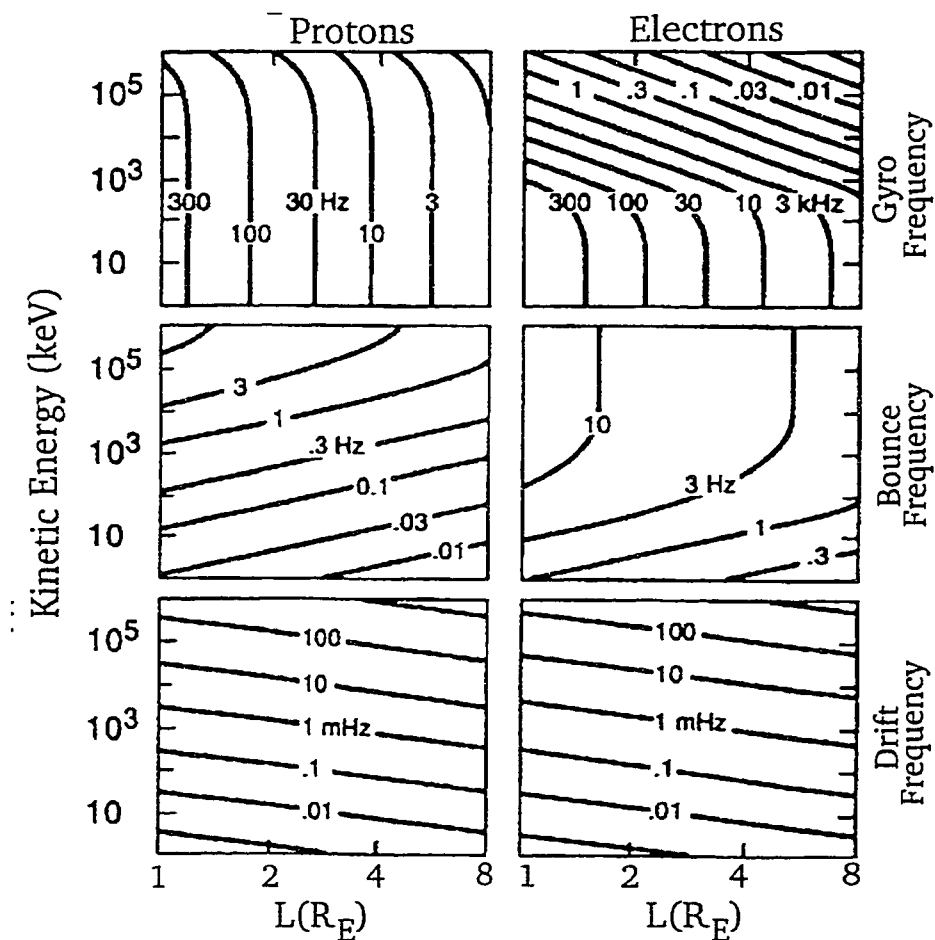
During the main phase of a storm the increase in ring current intensity causes a decrease in the magnetic field strength in the inner magnetosphere and a reduction in the magnetic flux  $\Phi$  enclosed within any given area of the inner magnetospheric equatorial plane [Roederer, 1970]. As long as the time scale of the magnetic field change is slow compared to an electron drift period ( $\tau \equiv |\partial \ln B / \partial t|^{-1} \gg \tau_d$ ), the electron changes its drift path while conserving all three adiabatic invariants,  $\mu = p_\perp^2 / 2mB$ ,  $J = \oint p_\parallel ds$ , and  $\Phi$ .

For reference, Figure 2.2 displays gyro-frequencies ( $\tau_c^{-1}$ ), bounce frequencies ( $\tau_b^{-1}$ ), and drift frequencies ( $\tau_d^{-1}$ ) for equatorially mirroring protons and electrons in a dipole field. Periods of gyro, bounce, and drift motion for a 1 MeV electron with  $90^\circ$  pitch angle in the dipole field for  $L = 6.6$  and  $L = 2.0$  are as follows:

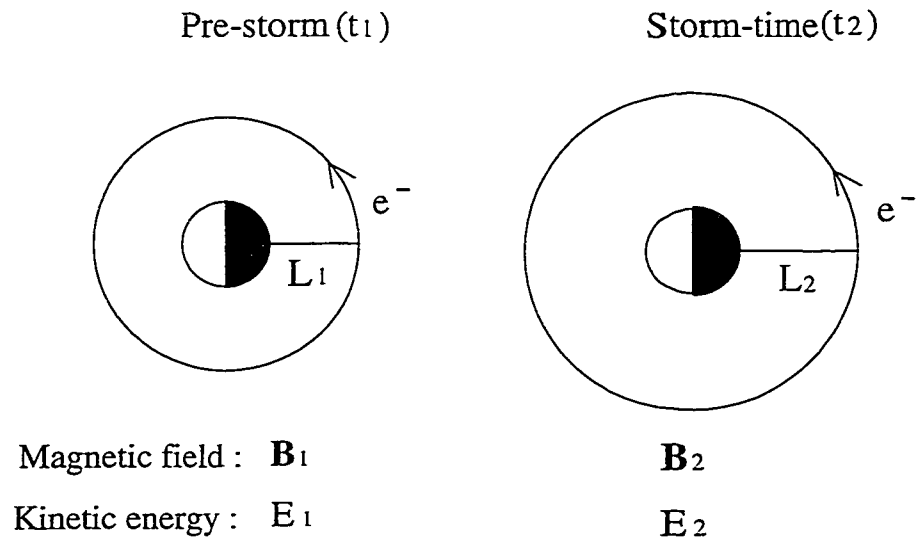
1 MeV	$\tau_d$	$\tau_b$	$f_c$
$L=6.6$	601 s	0.440s	1.02 kHz
$L=2.0$	1980 s	0.133 s	36.6 kHz

Figure 2.3 illustrates an adiabatic inflation of an equatorially-mirroring ( $J = 0$ ) electron drift shell during the main phase of a geomagnetic storm. The subscripts 1 and 2 denote pre-storm and storm-time quantities, respectively. If the magnetic field is azimuthally symmetric the electron drift shell is a circle with radius  $L$  Earth radii. If the magnetic field is not azimuthally symmetric we define the  $L$ -value as a radial distance of the drift shell at midnight. Although this definition of the  $L$  parameter is not conventional, it provides a simple convenient description of drift shell changes. Figure 2.4 shows that this definition of  $L$ -shell differs from the McIlwain  $L$ -shell ( $L_m$ ) by only a few percent in the  $L$  range of interest. Here  $L_m$  is calculated using the Ding-Toffoletto-Hill magnetic field model (see Section 2.4).

Referring again to Figure 2.3, at time  $t_1$  an electron drifts in the  $L_1$ -shell with magnetic field strength  $B_1$  and kinetic energy  $E_1$ . The corresponding pre-storm elec-



**Figure 2.2** The gyration, bounce, and drift frequencies for equatorially mirroring particles moving in the Earth's dipole field, as a function of  $L$  and particle kinetic energy (adapted from *Schulz and Lanzerotti* [1974]).



**Figure 2.3** Inflation of an electron drift shell ( $L_1 \rightarrow L_2$ ) in the equatorial plane for an axially symmetric magnetic field case. By changing its drift path an electron conserves the third adiabatic invariant during a slow decrease in the magnetic field ( $|\mathbf{B}_1| > |\mathbf{B}_2|$ ).

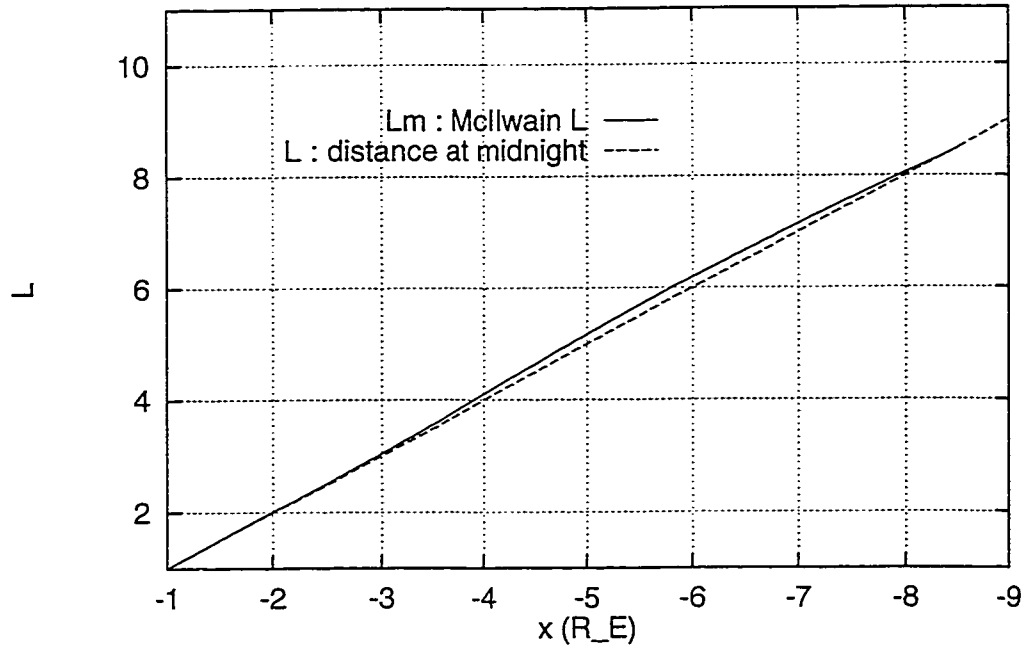


**Figure 2.4** Comparison of the  $L$ -values obtained from two definitions: a radial distance at midnight ( $L$ , used in this thesis) and the McIlwain parameter ( $L_m$ ).  $L_m$  is calculated using Ding-Toffoletto-Hill field model for quiet-time field configuration with  $Dst = 0$ . See section 2.4 for the field model and see Figure 2.9 for the parameter values used in the DTH model.

tron flux is denoted as  $j_1 = j(E_1, L_1; t_1)$ . As the storm-time ring current develops, the magnetospheric magnetic field configuration changes from  $B_1$  to  $B_2$ , decreasing the magnetic flux inside the pre-storm electron drift path. In order to conserve the third adiabatic invariant (the flux invariant,  $\Phi$ ) the electron  $L$ -shell increases from  $L_1$  to  $L_2$ , and because of conservation of the first invariant  $\mu$  the electron energy decreases from  $E_1$  to  $E_2$ . The corresponding storm-time electron flux is denoted as  $j_2 = j(E_2, L_2; t_2)$ .

### 2.3 Adiabatic transformation of quiet-time electron flux

Application of Liouville's theorem gives a simple equation for the fully-adiabatic transformation of the particle fluxes at different times. Liouville's theorem states that the phase space density is constant along a particle trajectory; in this case

$$f(\mu_1, J_1, \Phi_1; t_1) = f(\mu_2, J_2, \Phi_2; t_2). \quad (2.1)$$

We use the fact that the differential flux of particles with kinetic energy  $E$  and pitch angle  $\alpha$  at location  $\mathbf{r}$  is related to  $f(\mu, J, \Phi)$ , apart from constants, as follows:

$$j(E, \alpha, \mathbf{r}) \propto p^2 f(\mu, J, \Phi). \quad (2.2)$$

Here  $p$  is the relativistic momentum and  $j$  is the number of particles per unit area, time, energy and solid angle [*Schulz and Lanzerotti, 1974*].

Equation (2.2) is specialized to the case of the equatorially-mirroring particles by requiring  $p_{\parallel} = 0$  ( $\alpha = \pi/2$ ), and using the definition of  $\mu$ , so that

$$j_{\perp}(E, \mathbf{r}) \propto 2mB\mu f(\mu, J = 0, \Phi). \quad (2.3)$$

Then from Equations (2.1) and (2.3) the equatorially-mirroring storm-time electron flux,  $j_2$ , is related to the pre-storm electron flux,  $j_1$ , as follows:

$$j(E_2, L_2; t_2) = \frac{B_2(L_2)}{B_1(L_1)} j(E_1, L_1; t_1). \quad (2.4)$$

Here  $B_1(L_1)$  and  $B_2(L_2)$  are magnetic field strengths on the electron drift shells at time  $t_1$  and  $t_2$ , respectively, and from now on we drop the  $\perp$  subscript on  $j$ . Thus the storm-time electron flux  $j(E_2, L_2; t_2)$  is given in terms of the quiet-time electron flux  $j(E_1, L_1; t_1)$  multiplied by the magnetic field strength ratio,  $B_2(L_2)/B_1(L_1)$ .

Since we are especially interested in the relativistic electron flux variation at geosynchronous altitude for a fixed energy channel, we set  $L_2 = 6.6$  and choose values of  $E_2$  between 0.5 MeV and 2.0 MeV. The corresponding pre-storm values  $L_1$  and  $E_1$  are calculated using conservation of the first and third adiabatic invariants in the following subsection.

### Calculation of pre-storm values $E_1$ and $L_1$ .

The relation between the pre-storm  $L$ -shell,  $L_1$ , and storm-time  $L$ -shell,  $L_2$ , is obtained from the conservation of the magnetic flux linked by the particle orbit, i.e.,

$$\oint_1 \mathbf{B}_1 \cdot d\mathbf{S} = \oint_2 \mathbf{B}_2 \cdot d\mathbf{S}. \quad (2.5)$$

For a given storm-time electron drift path, the pre-storm  $L$ -shell,  $L_1$ , is obtained by solving Equation (2.5) for  $L_1$ .  $L_1$  can be calculated either analytically or numerically, depending on the magnetic field model.

The relation between the storm-time kinetic energy  $E_2$  and the pre-storm energy  $E_1$  (for an equatorially-mirroring electron) is obtained from the constancy of the first adiabatic invariant:

$$\frac{p_1^2}{2mB_1(L_1)} = \frac{p_2^2}{2mB_2(L_2)}, \quad (2.6)$$

and the relation between relativistic momentum and kinetic energy,  $p^2c^2 = E^2 + 2mc^2E$ . Solving Equation (2.6) in terms of  $E_1$ , we have

$$E_1 = -mc^2 + \sqrt{(mc^2)^2 + \frac{B_1(L_1)}{B_2(L_2)}(E_2^2 + 2mc^2E_2)}. \quad (2.7)$$

When  $E_2$  is given,  $E_1$  depends only on  $B_1(L_1)/B_2(L_2)$ . Note that this is also the inverse of the field strength ratio which appeared in Equation (2.4). Since the pre-storm magnetic field strength  $B_1$  is greater than the storm-time value  $B_2$ , Equation (2.7) shows that  $E_1$  is greater than  $E_2$ . Hence an electron loses kinetic energy when it drifts out to a larger  $L$ -shell during a geomagnetic storm.

In summary, given a series of storm-time magnetic field models, we can calculate  $L_1$  using Equation (2.5) and  $E_1$  using Equation (2.7). Then, given a pre-storm particle flux,  $j(E_1, L_1; t_1)$ , we can calculate the storm-time flux,  $j(E_2, L_2; t_2)$ , using Equation

(2.4). Next we describe the magnetic field models and the quiet-time electron flux model which are used as inputs to our calculations.

## 2.4 Magnetic field models

We use magnetospheric magnetic field models which have been developed at Rice University by *Hilmer and Voigt* [1995] and by *Ding* [1995]. These models are flexible and modular and can provide magnetic field values in the inner magnetosphere for a range of levels of geomagnetic activity. The magnetospheric magnetic field configuration is represented as  $\mathbf{B} = \mathbf{B}_{dip} + \Delta\mathbf{B}$ , where  $\mathbf{B}_{dip}$  is the Earth dipole field and  $\Delta\mathbf{B}$  is a magnetic field due to three major current systems: the ring current, the cross-tail current, and the magnetopause current. Since the magnetic field perturbation associated with the ring current is expected to be dominant in the inner magnetosphere (our region of interest), we construct our magnetic field models in two stages. First we assume the magnetic field model consists of only a vacuum dipole field plus a symmetric ring current field. For this we use an analytic ring current field model devised by *Hilmer and Voigt* [1995]. Second, we add to this symmetric model asymmetric magnetopause current and cross-tail current fields using the results of *Ding* [1995]. By comparing our results for the two field models we can separately evaluate the effects of the simple symmetric ring current field and the more complicated, more realistic asymmetric fields.

In both field models we assume a zero tilt for the Earth dipole field and we consider  $\Delta\mathbf{B}$  changes corresponding to the geomagnetic index  $Dst$ . The quiet-time magnetic field configuration is described by the magnetic field vector associated with zero  $Dst$ .

### The Hilmer-Voigt symmetric ring current field model

Assuming the storm-time magnetic field distortion results entirely from the ring current, the magnetic field may be expressed as  $\mathbf{B} = \mathbf{B}_{dip} + \mathbf{B}_{rc}$ . The analytic, azimuthally symmetric ring current field model developed by *Hilmer and Voigt* [1995] takes the following form in the equatorial plane:

$$B_{rc,z}(r) = 4B_+r_+^3 \frac{8r_+^2 - r^2}{(r^2 + 4r_+^2)^{5/2}} + 4B_-r_-^3 \frac{8r_-^2 - r^2}{(r^2 + 4r_-^2)^{5/2}}. \quad (2.8)$$

The quantities  $B_+$ ,  $B_-$ ,  $r_+$ , and  $r_-$  are the ring current parameters. The first term describes an eastward-traveling current system with characteristic radius  $r_+$  which produces a maximum northward magnetic deflection of size  $B_+$  at the center of the Earth. The second term describes a westward-traveling current distribution with characteristic radius  $r_-$  and a maximum southward magnetic deflection  $B_-$ .  $B_+$  and  $B_-$  are expressed in nano Tesla (nT) and  $r_+$ ,  $r_-$ , and  $r$  are in units of Earth radii. The models can provide a wide range of realistic ring current magnetic field configurations by varying the four parameters  $B_+$ ,  $r_+$ ,  $B_-$ , and  $r_-$  [Hilmer, 1989].

In the typical situation with  $|B_-| > |B_+|$  and  $|r_-| > |r_+|$ , the magnetic field in the equatorial plane,  $B_{rc,z}$  varies as shown in Figure 2.5. The quantity  $B_{rc,z}$  is negative near the Earth, reaches a minimum around  $r = 3R_E$  and recovers to small positive values before diminishing again with greater radial distance.

Following Hilmer and Voigt [1995] we use empirical relations between the magnetic field strength at given locations and  $Dst$  to help determine the four parameters of the ring current model [Sugiura, 1973; Su and Konradi, 1975; Hilmer, 1989]. Namely:

$$B_{rc,z}(r = 1) = -19.0 + Dst \quad (2.9)$$

$$B_{rc,z}(r = 3) = -45 + 0.83Dst \quad (2.10)$$

$$\frac{2.9B_{rc,z}(r = 1) - B_{rc,z}(r = 3)}{2} = B_+ + B_- \quad (2.11)$$

For a given  $Dst$ , the solutions to this set of nonlinear equations can be found as follows: for a given value of  $r_+$  and  $r_-$ , Equations (2.9) and (2.11) are reduced to linear equations for  $B_+$  and  $B_-$ . Varying  $r_+$  and  $r_-$  over a range of physically valid values while remembering that  $r_-$  must always be greater than  $r_+$ , we calculate  $B_+$  and  $B_-$  and iterate until the set of four parameters satisfies Equation (2.10). For a more negative  $Dst$ , the sum  $B_+ + B_-$  is made more negative and  $r_-$  decreases relative to  $r_+$ .

Figure 2.6 shows the resulting equatorial  $\Delta B$  profiles as a function of position along the Sun-Earth axis for three different  $Dst$  values. As  $Dst$  decreases, the minimum of ring current field moves Earthward and gets deeper, resulting in a greater geomagnetic field depression in the inner regions. Because our ring current model is, by design, consistent with the empirical relations of Equations (2.9) to (2.11) the  $\Delta B$  profiles shown in Figure 2.6 should be in reasonable agreement with observed values.

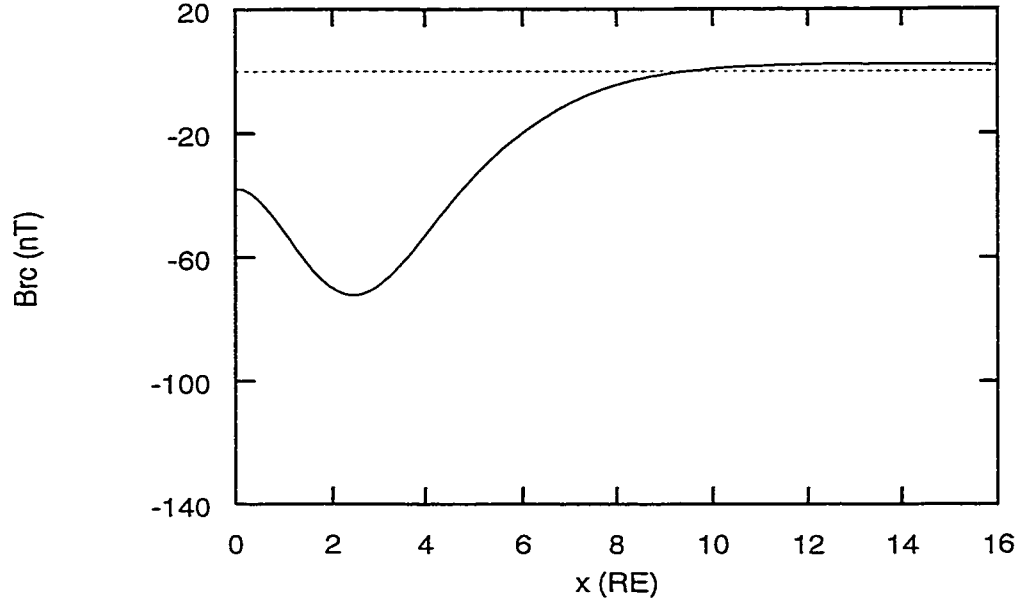


**Figure 2.5** Magnetic field strength of the ring current as a function of radial distance in the dipole equatorial plane,  $B_{rc,z}(r, z = 0)$ . The combination of eastward and westward traveling currents results in a maximum negative contribution near  $r = 3R_E$ . The model ring current has input parameters  $B_- = -310$  nT,  $B_+ = 272.2$  nT,  $r_- = 2.8R_E$ , and  $r_+ = 2.1R_E$ .

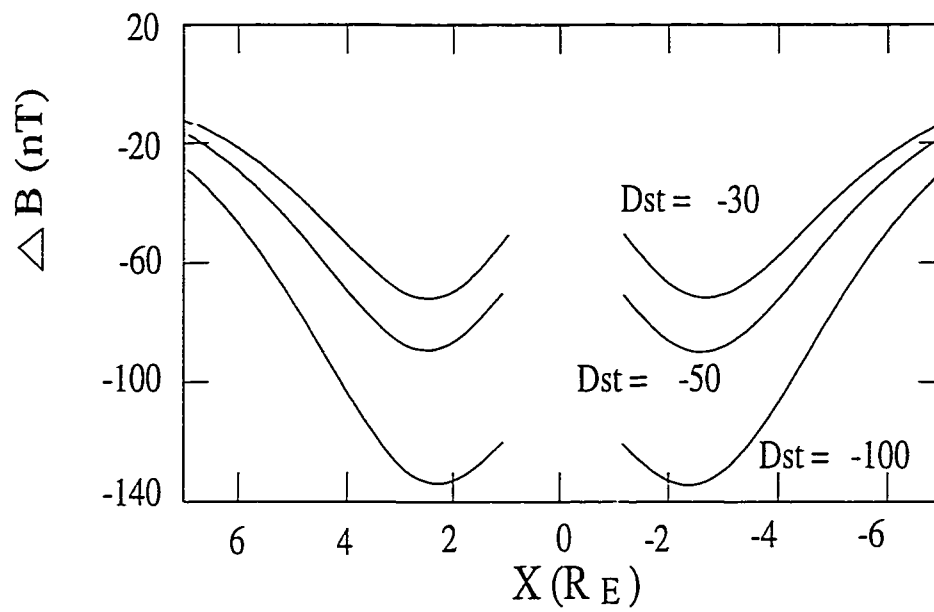


**Figure 2.6** Equatorial  $\Delta B$  profiles as a function of position along the Sun-Earth axis for the Hilmer-Voigt ring current field model for  $Dst = -30$ ,  $-50$ , and  $-100$  nT.

### The Ding-Toffoletto-Hill field model

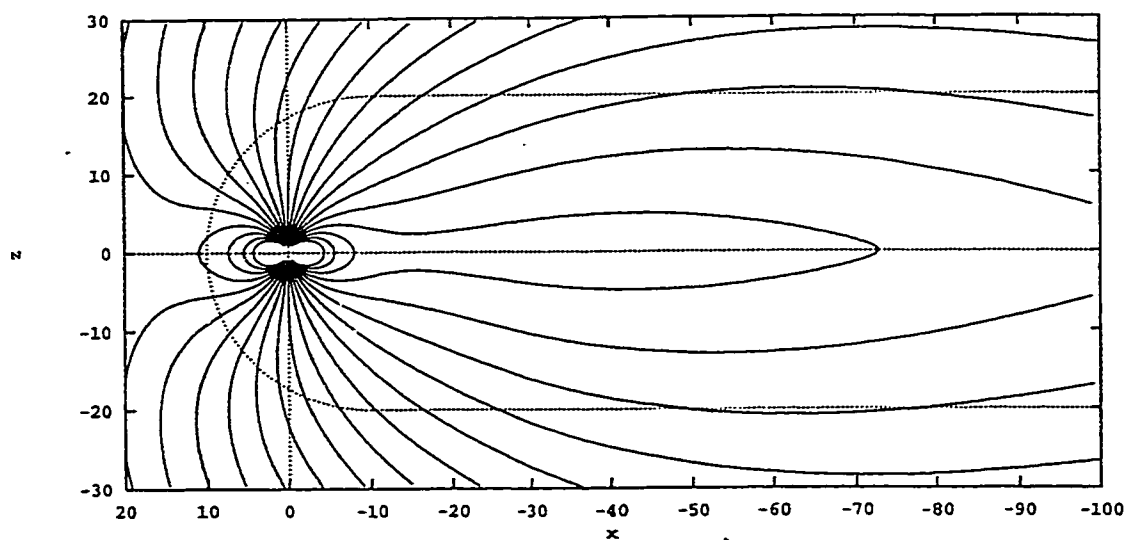
Although a strong ring current magnetic field contributes most of the magnetic perturbations in the inner magnetosphere, other magnetospheric current systems, such as the cross-tail and the magnetopause currents, should be included in the field model for a more realistic representation of the geomagnetic field. Also, we wish to evaluate the effect of the corresponding magnetic field asymmetry on the electron fully-adiabatic response. An appropriate magnetic field model has been developed by Ding, Toffoletto, and Hill [Ding, 1995; Ding et al., 1996] (hereafter the DTH model).

In the DTH model, the magnetic field is given as

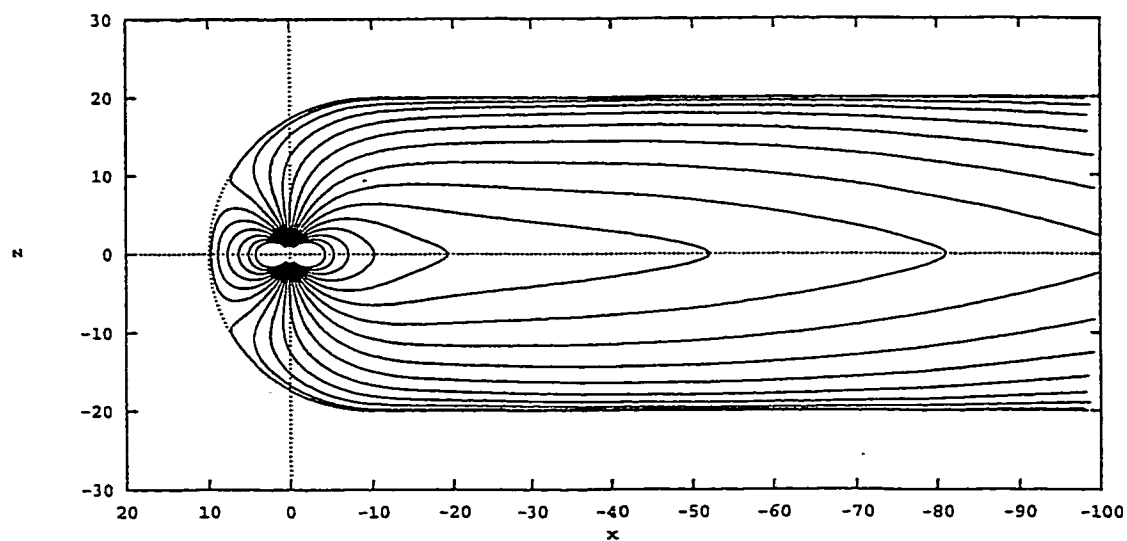
$$\mathbf{B} = \mathbf{B}_{dip} + \mathbf{B}_{rc} + \mathbf{B}_{mc} + \mathbf{B}_{tc}. \quad (2.12)$$

The tail current configuration is represented by cross-tail segments consisting of an infinite number of adjacent diffuse magnetic filaments. As geomagnetic activity increases the ring current and the tail current strengthen. While changing the ring current magnetic field strength as described previously, we control the tail current field strength by adjusting the current sheet configurations as follows. As magnetic activity increases, the current sheet moves Earthward, the intensity of the inner edge current sheet increases, the ratio of magnetic field strength at the far tail to the inner edge decreases, and the current sheet thins. We change the necessary parameters roughly linearly with  $Dst$  from quiet-time values to stretched and magnetically active configurations.

Assuming a closed magnetopause, the magnetopause current field is calculated by the boundary condition that the field component of the magnetopause current that is perpendicular to the magnetopause has to be equal and opposite to the field component of the interior field. The total magnetic field is therefore parallel to the magnetopause. The DTH model assumes the magnetopause shape is a hemisphere attached to a cylinder. We set the cylinder radius to  $20 R_E$  and the distance from the center of the Earth to the nose of the magnetopause to  $10 R_E$ . For simplicity, these parameters don't change with changes in  $Dst$  values, so the present work does not include magnetic field changes associated with motion of the dayside magnetopause. Figure 2.7 illustrates the shielded and the unshielded magnetic field produced by the dipole, the ring current and the tail current.



(a)



(b)

**Figure 2.7** (a) The unshielded magnetic field produced by the dipole, the ring current and the tail current. (b) The shielded field configuration after including the effect of the Chapman-Ferraro current. Adopted from *Ding* [1995].

The solid lines in Figure 2.8 show the equatorial  $\Delta B$  profiles for the DTH model as a function of position along the Sun-Earth axis. The magnetopause current flowing from dawn to dusk in the day-side magnetosphere gives a positive magnetic field deflection inside the magnetopause. Along with the enhancement of the nightside field distortion by the cross-tail current, the magnetopause current increases the asymmetry in the  $\Delta B$  profile. Except for the day-night asymmetry, the overall profile is similar to the ring current field model (dashed lines). Again, this is because the ring current accounts for most of the field depression in the inner magnetosphere.

## 2.5 Quiet time electron flux profile

To obtain a quiet-time electron flux profile as a function of energy and  $L$ -value, i.e.,  $j(E, L)$  in Equation (2.4), we used the differential electron flux data from the High Energy Electron Fluxmeter (HEEF) instrument flown on the Combined Release and Radiation Effects Satellite (CRRES) [Brautigam *et al.*, 1992]. One of the major scientific objectives of CRRES was to elucidate the dynamics of the high energy electrons in the outer-radiation belt with modern particle detectors [Gussenhoven *et al.*, 1991; Vampola *et al.*, 1992; Brautigam *et al.*, 1992].

The CRRES satellite was launched on 25 July 1990 and measured near-Earth particle populations over a wide energy range for fourteen months, as it traversed the radiation belts in a highly eccentric (perigee 350 km, apogee 33584 km), approximately equatorial ( $18^\circ$  inclination) orbit. Within a period of about 10 hours, the satellite made at least four transits through the outer zone each day. The High Energy Electron Fluxmeter (HEEF) measures 0.8 to 8 MeV electrons in ten differential energy channels every 0.5 seconds. The instrument and its extensive pre-flight calibration are described in detail in Dichter and Hanser [1989].

For the construction of an equatorially-mirroring electron flux profile, the data of  $90^\circ$  and  $85^\circ$  pitch angle bins were added together to obtain better statistics and the fluxes were averaged over 10 orbits (orbits 430–439) executed during a relatively quiet period (18–22 January 1991). The values of  $|Dst|$  remain less than 15 nT for this period. Figure 2.9 compares the measured magnetic field values by CRRES for the 10 orbits (symbols) and the quiet-time magnetic field strength associated with

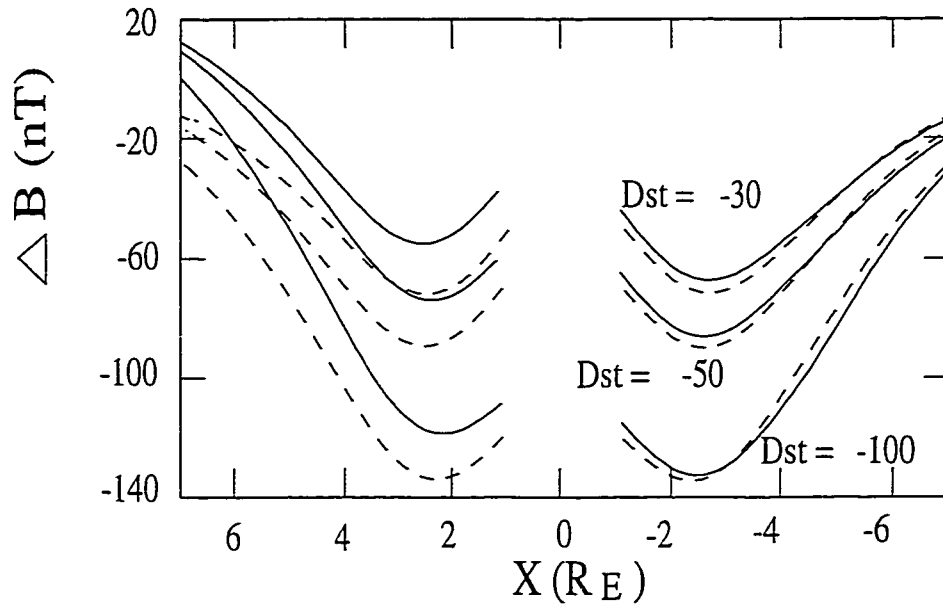


**Figure 2.8** Equatorial  $\Delta B$  profiles for the Ding-Toffoletto-Hill field model (solid lines) along the Sun-Earth axis for  $Dst = -30, -50$ , and  $-100$  nT. Except for the day–night asymmetry, the overall profile is similar to the Hilmer-Voigt ring current field model (dashed lines). The used parameter values for the DTH model are as follows: For  $Dst = -30$  nT,  $r_- = 2.7$ ,  $B_- = -701.86$ ,  $r_+ = 2.39$ ,  $B_+ = 665.76$ ,  $r_I = -6.0$ ,  $r_F = -200$ ,  $j_I = 6.0$ ,  $j_{frac} = 0.19$ ,  $Dy = 9.0$ ,  $\Delta = 2.17$ . For  $Dst = -50$  nT,  $r_- = 2.74$ ,  $B_- = -1104.69$ ,  $r_+ = 2.51$ ,  $B_+ = 1047.89$ ,  $r_I = -6.0$ ,  $r_F = -200$ ,  $j_I = 6.0$ ,  $j_{frac} = 0.19$ ,  $Dy = 9.0$ ,  $\Delta = 2.17$ . For  $Dst = -100$  nT,  $r_- = 2.93$ ,  $B_- = -1335.12$ ,  $r_+ = 2.67$ ,  $B_+ = 1226.57$ ,  $r_I = -5.0$ ,  $r_F = -200$ ,  $j_I = 15.0$ ,  $j_{frac} = 0.17$ ,  $Dy = 9.0$ ,  $\Delta = 1.0$ . See Figure 2.9 for the meanings of the tail current parameters.

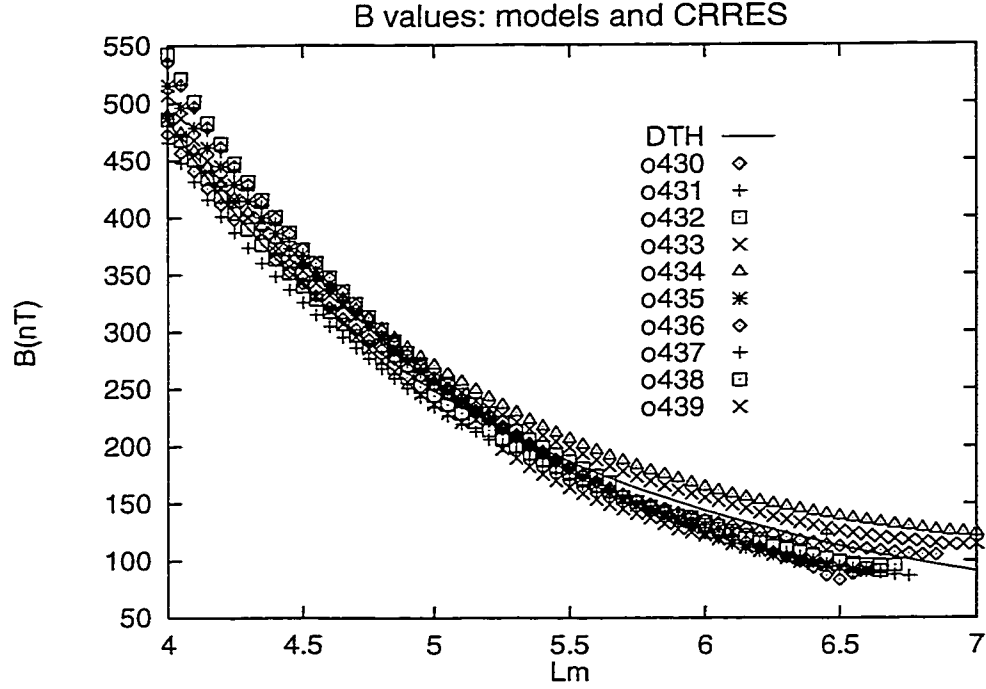


**Figure 2.9** Magnetic field values measured by CRRES for 10 orbits and quiet time magnetic field strength, corresponding to  $Dst = 0$  nT, calculated from DTH model. For DTH model, the used ring current parameters are  $B_+ = 272.2$ ,  $r_+ = 2.1$ ,  $B_- = -310$ ,  $r_- = 2.8$ , and the tail current parameters are the distance to inner edge of plasma sheet ( $r_I = -7.5$ , current sheet strength at inner edge ( $j_I = 2.5$ , distance to far tail edge ( $r_F = -200$ , the fraction of current sheet strength remaining in far tail ( $j_{frac} = 0.25$ , the characteristic distance for changes in the  $y$ -direction  $\Delta y(Dy) = 9.0$ , and the characteristic magnetic filament half thickness ( $\Delta = 3.5$ .

$Dst=0$  nT calculated from the DTH model (solid curve). The difference between the field strength measurement and the magnetic field model is acceptable.

Rather than seeking a global fit to the CRRES flux data, we confined the  $L$  value range to within  $5.0 \sim 7.5 R_E$ , the most relevant  $L$  values for this calculation. We made a quadratic exponential fit of the form

$$j(E, L) = e^{a(E)L^2 + b(E)L + c(E)}. \quad (2.13)$$

We first treat  $L$  as an independent variable and use a least square method to minimize fitting errors; then the parameters  $a(E)$ ,  $b(E)$ , and  $c(E)$  for different energy values are fitted as a quadratic function of  $E$  using least square fits. At fixed energy value  $E_o$ , the coefficient  $a(E_o)$ ,  $b(E_o)$  and  $c(E_o)$  are chosen to minimize the fitting error,

$$\epsilon_1 = \sum_i (a(E_o)L_i^2 + b(E_o)L_i + c(E_o) - \log j(L_i, E_o))^2, \quad (2.14)$$

and the coefficients  $a$ ,  $b$  and  $c$  are again fitted by quadratic polynomials of the energy, minimizing errors of the form

$$\epsilon_a = \sum_i (a(E_i) - a_1 E_i^2 - a_2 E_i - a_3)^2. \quad (2.15)$$

This fitting procedure gives:

$$a(E) = 0.1581E^2 - 0.5371E - 0.7035 \quad (2.16)$$

$$b(E) = -1.5495E^2 + 4.6898E + 8.3803 \quad (2.17)$$

$$c(E) = 4.6338E^2 - 17.3861E - 13.5071 \quad (2.18)$$

Figure 2.10 illustrates the CRRES electron flux data (symbols) and the exponential fit,  $j(E, L)$  (solid lines) for the relevant  $L$  ranges. The  $L$ -value where the electron flux is maximum is around  $5R_E$  in each energy channel and at higher  $L$ -values the electron fluxes decrease exponentially with increasing energy. This behavior is also seen in a plot of the electron flux fit  $j(E, L)$  versus energy for three  $L$  values in Figure 2.11. Although the electron flux decreases exponentially with energy, the slope is smaller for larger energy in the range of 0.5 MeV–3.5 MeV, a fact which we will use in Chapter 3. Also, the  $L$  dependence of the electron flux is relatively weak compared with the energy dependence. We emphasize that the fitted fluxes, as given by Equation (2.13), are reliable only for the restricted energy and  $L$ -values mentioned above.

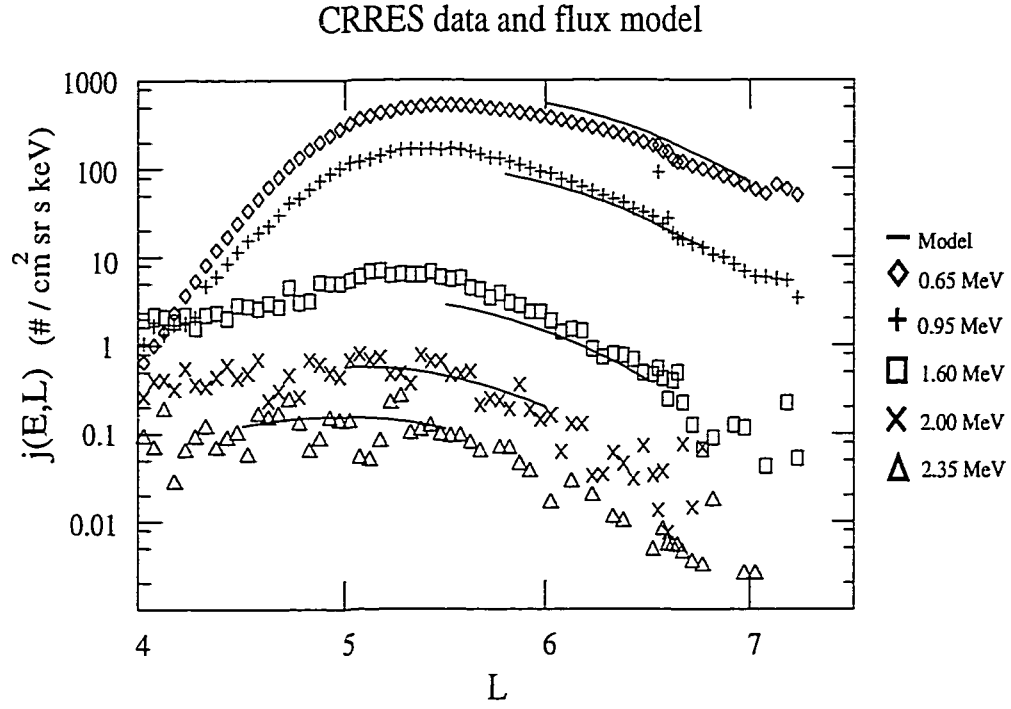


**Figure 2.10** CRRES quiet time ( $|Dst| < 15$  nT) electron flux data (symbols) and the exponential fits  $j(E, L)$  (lines) in the relevant  $L$  ranges. The electron fluxes decrease exponentially with energy at higher  $L$  values.

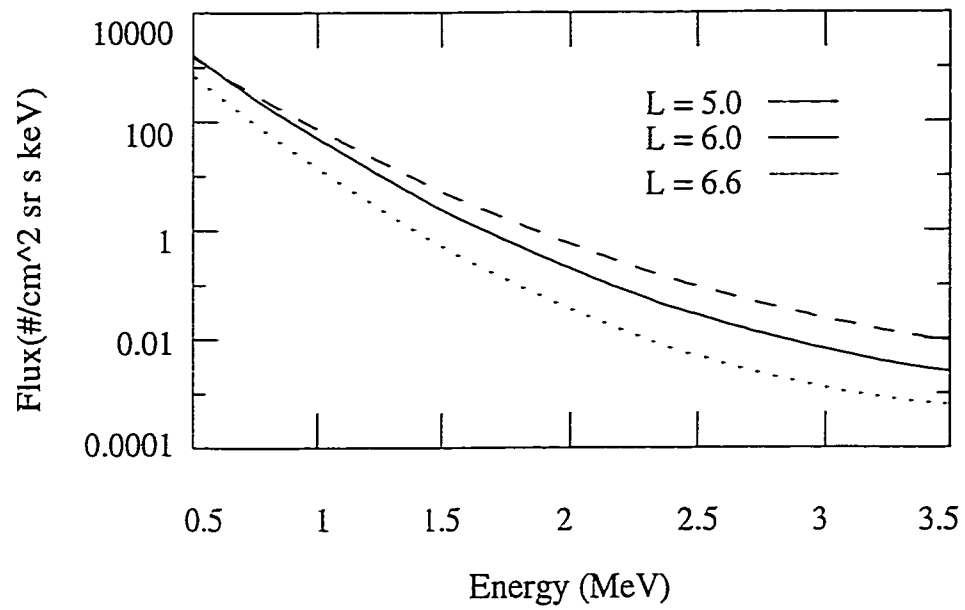


**Figure 2.11** Values of model electron fluxes for three different  $L$  values,  $L=5.0$ ,  $6.0$ , and  $6.6$ . The  $L$  dependence of the electron flux is relatively weak in comparison with the energy dependence.

## Chapter 3

### Simulation of the storm main phase flux decrease

#### 3.1 Calculation of fully-adiabatic electron flux variations

Using the magnetic field models and the quiet-time electron flux model described in the previous chapter as inputs, we can calculate the fully-adiabatic storm-time electron flux variations for a given change in  $Dst$ .

Quantities related to calculations of 1 MeV electron fluxes at synchronous orbit are plotted in Figure 3.1. We set  $L_2 = 6.6$  and  $E_2 = 1.0$  MeV for  $Dst$  values from 0 nT to  $-100$  nT. Recall that the pre-storm  $L$ -shell and energy,  $L_1$  and  $E_1$ , are calculated from Equations (2.5) and (2.7). Then the pre-storm electron flux  $j_1$  is obtained from the quiet-time electron flux distribution given in Equation (2.13) and the storm-time electron flux  $j_2$  is obtained by multiplying  $j_1$  by the magnetic field ratio,  $B_2(L_2)/B_1(L_1)$  as in Equation (2.4). Figures 3.1(a) to 3.1(e) show the quantities  $L_1$ ,  $E_1$ ,  $j_1$ ,  $B_2(L_2)/B_1(L_1)$ , and  $j_2$ , respectively. Solid lines represent values obtained using the Hilmer-Voigt symmetric ring current field model and dashed lines give values for the Ding-Toffoletto-Hill (DTH) field model.

In Figures 3.1(a) and 3.1(b),  $L_1$  monotonically decreases with decreasing  $Dst$  while  $E_1$  increases, starting from  $L_1 = L_2$  and  $E_1 = E_2$  at  $Dst = 0$  nT, for both magnetic field models. This demonstrates that the pre-storm electron which drifts on a lower  $L$ -shell with higher energy appears at synchronous orbit with lower kinetic energy, as expected. Figure 3.2 shows the change in drift shells for the DTH field model. The inner and outer solid contours are the pre-storm drift paths,  $L_1$ , corresponding to  $Dst = -100$  and  $-60$  nT respectively, and the dashed contour shows synchronous orbit. This figure illustrates that electrons from lower  $L$ -shells appear at geosynchronous region for lower  $Dst$ . The rate of change of  $E_1$  and  $L_1$  with  $Dst$  is slightly larger for the symmetric field model than the DTH model. This is because the magnetic flux changes associated with the storm-time magnetic field are less for the DTH model because the magnetopause current weakens the day-side field perturbation.

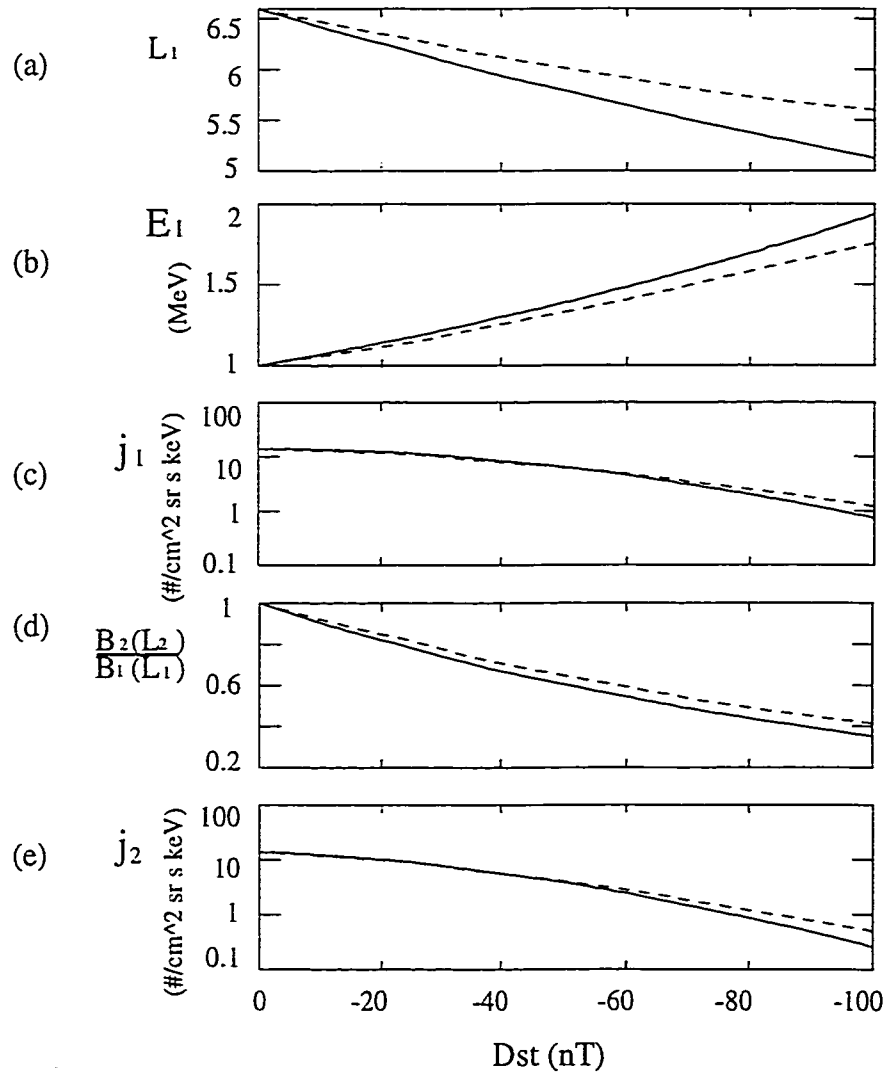


**Figure 3.1** (a) Pre-storm  $L$  value,  $L_1$  from Equation (2.5). (b) Pre-storm energy from Equation (2.7). (c) Pre-storm electron flux,  $j_1(L_1, E_1)$  from flux model in Equation (2.13). (d) Magnetic field ratio at pre-storm and storm time drift shells,  $B_2(L_2)/B_1(L_1)$ . (e) Storm time electron flux,  $j_2(L_2, E_2)$  from Equation (2.4). Solid lines represent the results for the Hilmer-Voigt ring current field model, dashed lines represent the results for the Ding-Toffoletto-Hill field model.

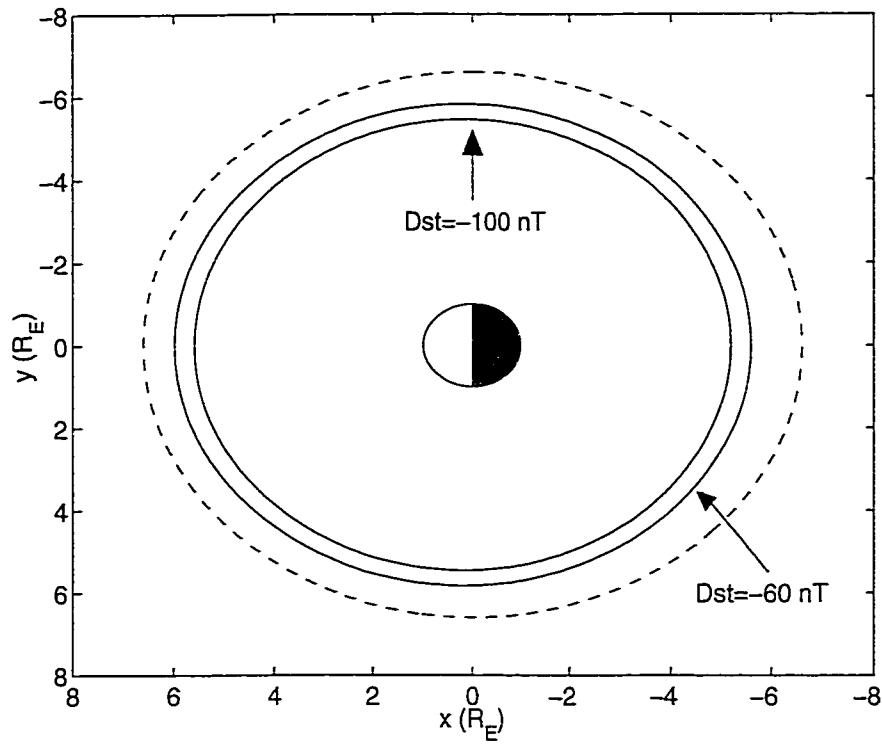


**Figure 3.2** Adiabatic change of drift shells for the DTH field model: the inner and outer solid contours are the pre-storm drift paths ( $L_1$ ) of an electron that moves out to  $L_2 = 6.6$  when  $Dst = -100$  and  $-60$  nT, respectively. The dashed contour denotes geosynchronous orbit.

In Figure 3.1(c) the pre-storm electron flux,  $j_1$ , decreases monotonically with decreasing  $Dst$ . This is attributed to the combined effect of the variation of  $E_1$  with  $Dst$  (Figure 3.1(b)) and the quiet-time electron flux energy dependence.

The ratio of the magnetic field strengths of the electron drift shells after and before the storm,  $B_2(L_2)/B_1(L_1)$ , is plotted in Figure 3.1(d). Figure 3.3 shows the  $L$ -dependence of magnetic field strength for  $Dst = 0, -60$ , and  $-100$  nT for the DTH model. It is evident that the magnetic field weakens as the magnetic storm increases ( $Dst$  increases negatively). Triangles on the  $Dst = -60$  nT and  $-100$  nT curves mark the storm-time magnetic field strength at  $L_2 = 6.6$ , which gives  $B_2(L_2)$ . Circles on the  $Dst = 0$  nT curve indicate magnetic field values at pre-storm drift shells, namely  $L_1 = 5.64$  and  $5.12$ , which are associated with  $Dst = -60$  nT and  $-100$  nT, respectively; these points yield values of  $B_1(L_1)$ . Because the pre-storm magnetic field is stronger than the corresponding storm-time values, the ratio of magnetic field strengths at storm-time to pre-storm is less than 1.0 for  $Dst < 0$  nT, as shown in Figure 3.1(d). As  $Dst$  decreases,  $L_1$  decreases and so the pre-storm magnetic field strength  $B_1$  increases due to the dominant term of  $1/r^3$  in the dipole field, while  $B_2(L_2)$  changes only a small amount. Overall, the magnetic field ratio  $B_2(L_2)/B_1(L_1)$  becomes smaller when the magnetic activity becomes stronger. Compared with the DTH model, the value of  $B_2(L_2)/B_1(L_1)$  is smaller for the symmetric field model because it gives smaller  $L_1$  for the same  $Dst$  and so larger  $B_1(L_1)$ .

Figure 3.1(e) shows the storm-time electron flux  $j_2$ . Since  $B_2(L_2)/B_1(L_1)$  is smaller than 1.0 for  $Dst < 0$  nT, the storm-time electron flux is smaller than the pre-storm electron flux, as expected. The storm-time flux,  $j_2$ , is slightly larger for the DTH model because the effect of symmetric ring current field has been reduced by the dayside magnetopause currents.

### 3.2 Fluxes for an artificial storm

In Figure 3.4 we plot fully-adiabatic electron fluxes for 1 MeV and 2 MeV electrons at synchronous altitude for an artificial  $Dst$  time series. The artificial  $Dst$  is fabricated to reproduce the main phase and the recovery phase of a typical magnetic storm, but it is free of the “noise” present in the real  $Dst$  data and so the corresponding changes in

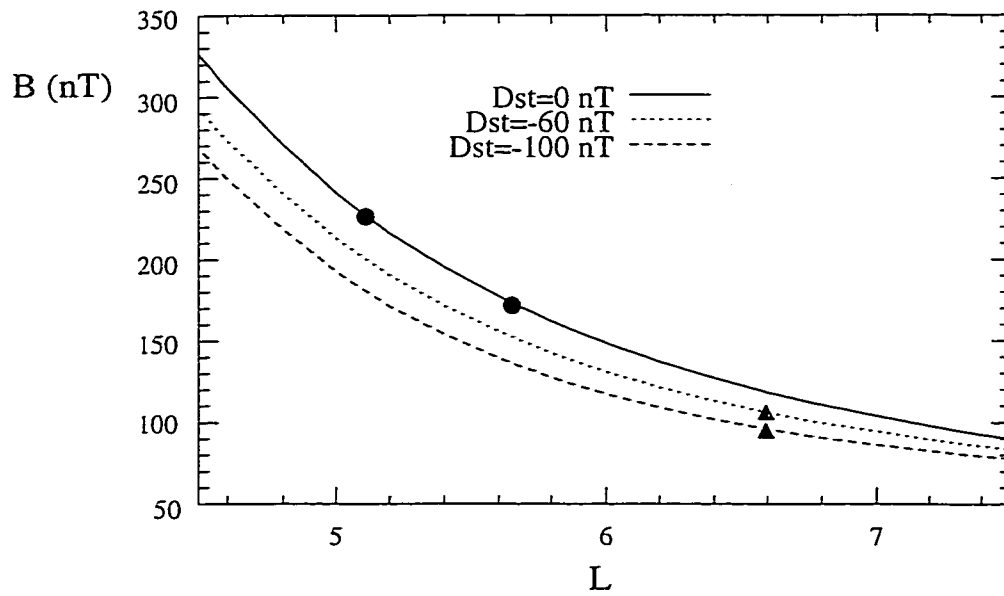


**Figure 3.3** Magnetic field strength as a function of  $L$  for  $Dst = 0, -60$ , and  $-100$  nT. Triangles on the  $Dst = -60$  nT and  $-100$  nT curves indicate the storm-time magnetic field strength at  $L_2 = 6.6$ . Circles on the  $Dst = 0$  nT curve indicate magnetic field values at pre-storm drift shells, i.e.,  $L_1 = 5.64$  for  $Dst = -60$  nT and  $L_1 = 5.12$  for  $-100$  nT.

electron flux are easier to interpret. The solid and dashed lines show fluxes calculated using the symmetric Hilmer-Voigt and the DTH magnetic field models, respectively.

As expected, the storm-time relativistic electron flux variation tracks the pattern of changes in  $Dst$  with the same time scale. The similarity between the variation in  $Dst$  and the *logarithm* of electron flux appears naturally for fully-adiabatic flux changes as follows: the pre-storm values  $L_1$  and  $E_1$  change roughly linearly with decreasing  $Dst$  (as shown in Figures 3.1(a) and 3.1(b)), so from Equation (2.4) and the exponential energy dependence of the quiet-time electron flux, the storm-time electron flux  $j_2$  decreases exponentially with  $Dst$ ; thus changes in the logarithm of  $j_2$  will be similar to changes in  $Dst$ .

When  $Dst = -100$  nT the electron fluxes decrease by a factor of  $\sim 15$  for the 2 MeV electrons and a factor of  $\sim 55$  for the 1 MeV electrons, compared to the pre-storm values. Thus our calculations also reproduce the observed energy dependence of the size of the electron flux drop at the minimum of  $Dst$ ; namely, larger flux drops occur for lower energies (see Figure 1.1). This is due primarily to the electron flux energy dependence shown in Figure 3.1(b).

Comparison of the results for the symmetric Hilmer-Voigt and the DTH magnetic field models (the solid and dashed curves) shows that the asymmetry of the DTH model produces a small effect in the fully-adiabatic fluxes, a result which is expected from the discussion of Figure 3.1. However, there is an important difference in the recovery-phase fluxes for the two models. In the symmetric Hilmer-Voigt model the electron fluxes can recover reversibly to the pre-storm levels but the presence of the magnetopause in the DTH model introduces a trapping boundary (i.e., a last closed drift orbit) which can prevent this. This trapping boundary effect is discussed in the following section.

In order to quantify the energy dependence of the electron flux drop at synchronous orbit in a given energy channel, we calculate the ratio of the electron flux before the storm at synchronous orbit to the storm-time flux at synchronous orbit for a given  $Dst$ . By using Equation (2.4) we can express this ratio,  $R_j \equiv j(E_2, L_2, t_1)/j(E_2, L_2, t_2)$  as follows:

$$R_j \equiv \frac{j(E_2, L_2; t_1)}{j(E_2, L_2; t_2)} = \frac{j(E_2, L_2; t_1) B_1(L_1)}{j(E_1, L_1; t_1) B_2(L_2)} \quad (3.1)$$

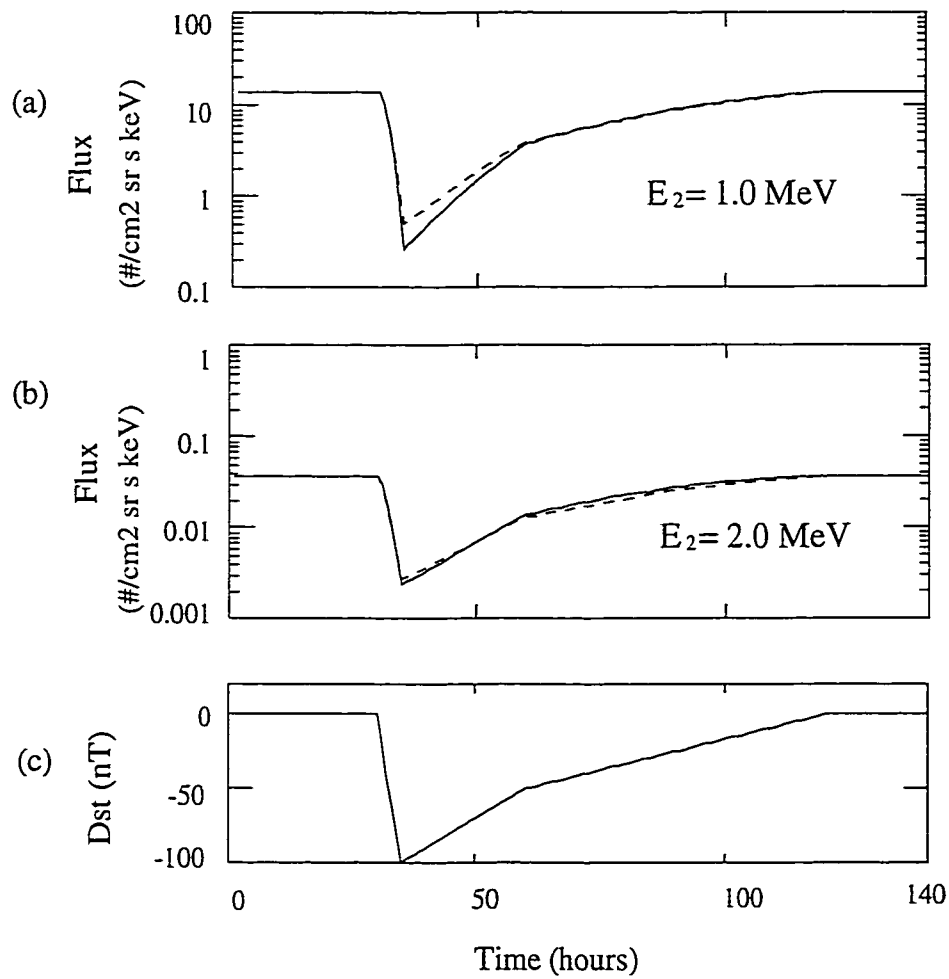


**Figure 3.4** Electron flux variations for (a) 1.0 MeV and (b) 2.0 MeV electrons for (c) an artificial *Dst* time series. Solid lines represent the results for the Hilmer-Voigt ring current field model, and dashed lines represent the results for Ding-Toffoletto-Hill field model.

When  $L_2 = 6.6$ , the pre-storm  $L$ -value is  $L_1 = 5.1$  for  $Dst = -100$  nT, say, thus we compute  $R_j$  as follows for this case:

$$R_j = \frac{j(E_2, 6.6; t_1) B_1(5.1)}{j(E_1, 5.1; t_1) B_2(6.6)} \quad (3.2)$$

Figure 3.5 illustrates the calculation of  $R_j$  for the cases of  $E_2 = 1$  MeV and 2 MeV when  $Dst = -100$  nT. Figure 3.5(a) displays pre-storm electron fluxes relevant to the calculation of  $R_j$ . The quiet-time electron flux  $j(E, L; t_1)$  versus  $E$  is plotted for  $L = 5.1$  and 6.6. Note that the pre-storm energy corresponding to  $E_2 = 1$  MeV and 2 MeV are  $E_1 = 1.99$  and 3.54 MeV for  $Dst = -100$  nT. A' and B' in Figure 3.5(a) indicate electron fluxes  $j(1, 6.6; t_1)$  and  $j(1.99, 5.1; t_1)$  for  $E_2 = 1$  MeV, and  $j(2, 6.6; t_1)$  and  $j(3.54, 5.1; t_1)$  for  $E_2 = 2$  MeV. Multiplying  $B_1(5.1)/B_2(6.6)$  to the ratio of these fluxes gives  $R_j$  for  $Dst = -100$  nT. The  $R_j$  for 1 and 2 MeV storm-time energies are indicated as A and B in Figure 3.5(b).

In Figure 3.6 we plot the ratio  $R_j$  versus electron energy at synchronous orbit for several  $Dst$  values. For ease of calculation the Hilmer-Voigt magnetic field model was used. For a given storm with a given  $Dst$  minimum, Figure 3.6 can be used to estimate the factor by which the fully-adiabatic effect decreases 1 MeV to 2 MeV electron fluxes at synchronous orbit.

### 3.3 Comparison with flux measurements

Electron fluxes measured by a geostationary satellite exhibit significant local-time variations due to the day-night asymmetry of the magnetosphere, the so-called *diurnal effect*. Figure 3.7 shows the fluxes measured by two geostationary satellites, SC1989-046 and SC1986-129, separated by about 12 hours in local time, during the 2–10 November 1993 storm. The local time is related to the universal time as  $LT = UT + 0.51$  for SC 1984-129 and  $LT = UT + 11.5$  for SC 1989-046. The spacecrafts measure higher fluxes at local noon with one day periodicity.

The diurnal effect is attributed to the fact that geosynchronous spacecraft measure predominantly near-equatorial electrons at lower  $L$ -shells near noon, and energetic electron fluxes are generally larger on lower  $L$ -shells. Figure 3.8 presents two  $L$ -shells adjacent to geosynchronous orbit (which is shown with the dashed line): one at noon and the other at midnight. These  $L$ -shells are calculated using the DTH field

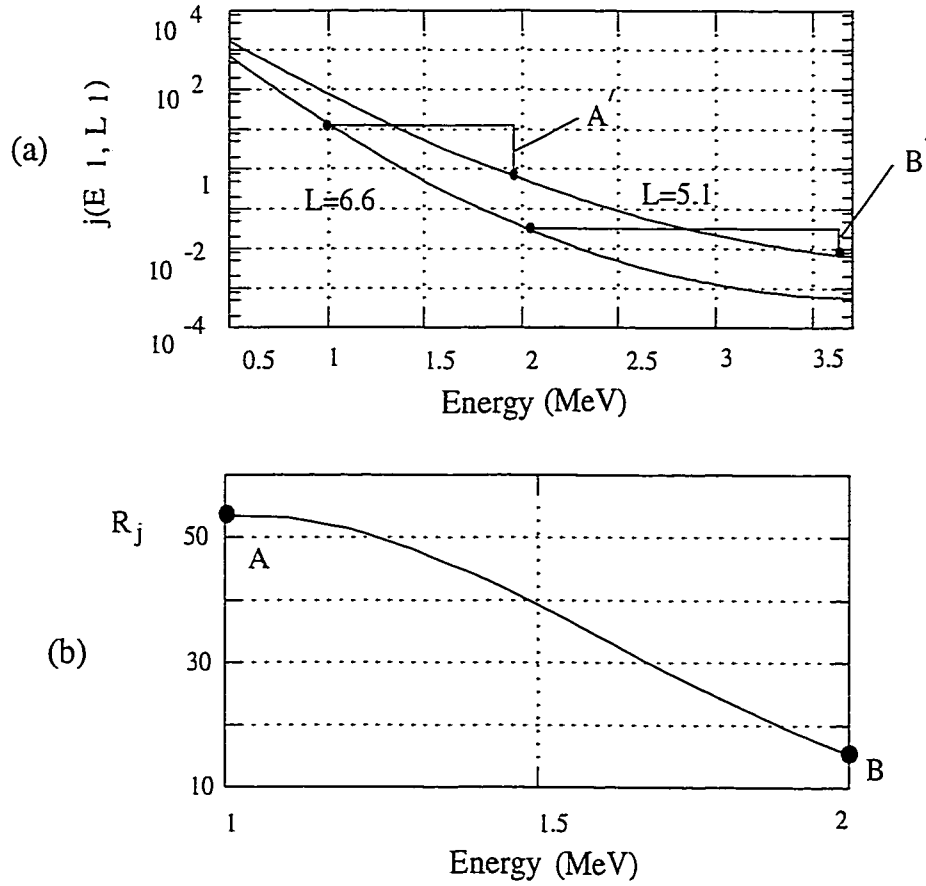


**Figure 3.5** (a) Quiet time electron flux  $j(E, L, t_1)$  versus energy for  $L_1 = 5.1$  and 6.6 when  $Dst = -100$  nT. Note that the pre-storm energies corresponding to storm-time energy  $E_2 = 1$  and 2 MeV are  $E_1 = 1.99$  and 3.54 MeV, respectively. A' and B' indicate the relevant electron fluxes to calculate  $R_j$  for the case of  $E_2 = 1$  and 2 MeV. (b)  $R_j$  versus energy for  $Dst = -100$  nT. A and B indicate  $R_j$  values for storm-time energies, 1 MeV and 2 MeV.

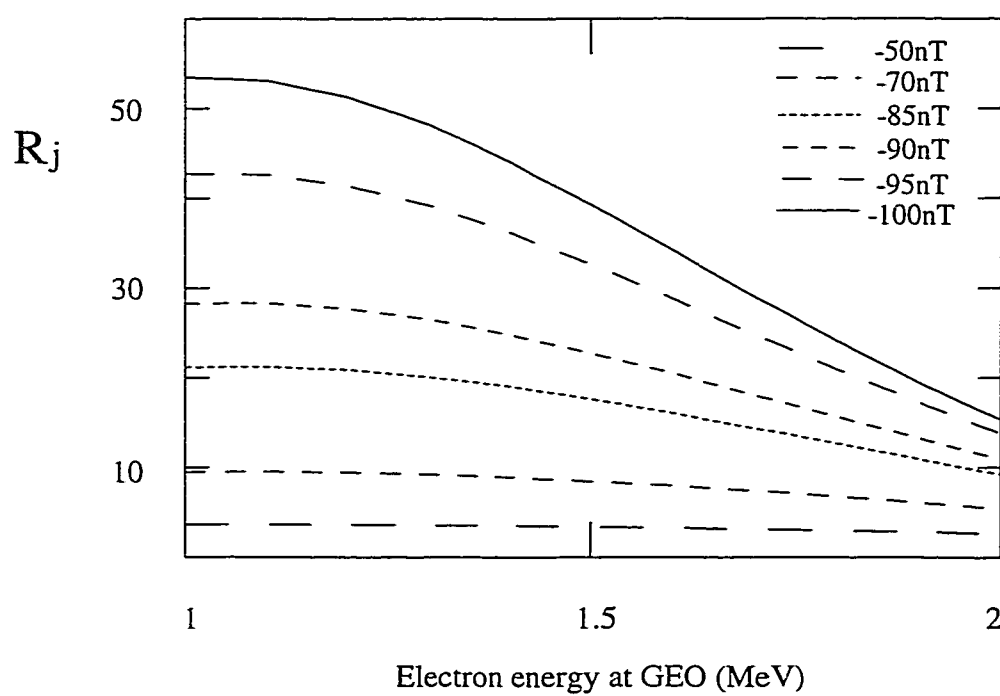


**Figure 3.6** Ratio of quiet-time flux to storm time flux,  $R_j$ , versus storm-time energy at synchronous orbit for several  $Dst$  values.

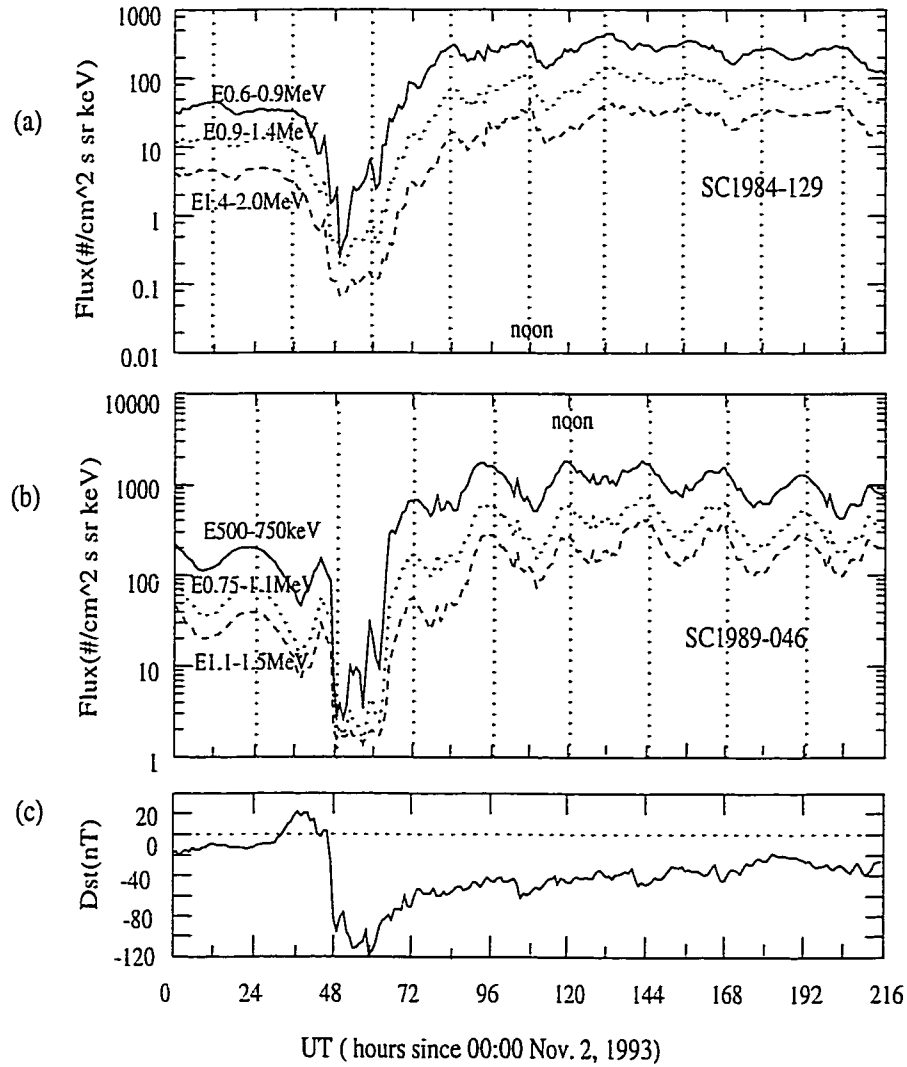


**Figure 3.7** Fluxes measured by two geostationary satellites separated by about 12 hours in local time: (a) SC1984-129 with  $LT = UT + 0.51$ , (b) SC1989-046 with  $LT = UT + 11.5$ , both during the 2–10 November 1993 storm. The corresponding hourly-averaged  $Dst$  values are plotted in (c).

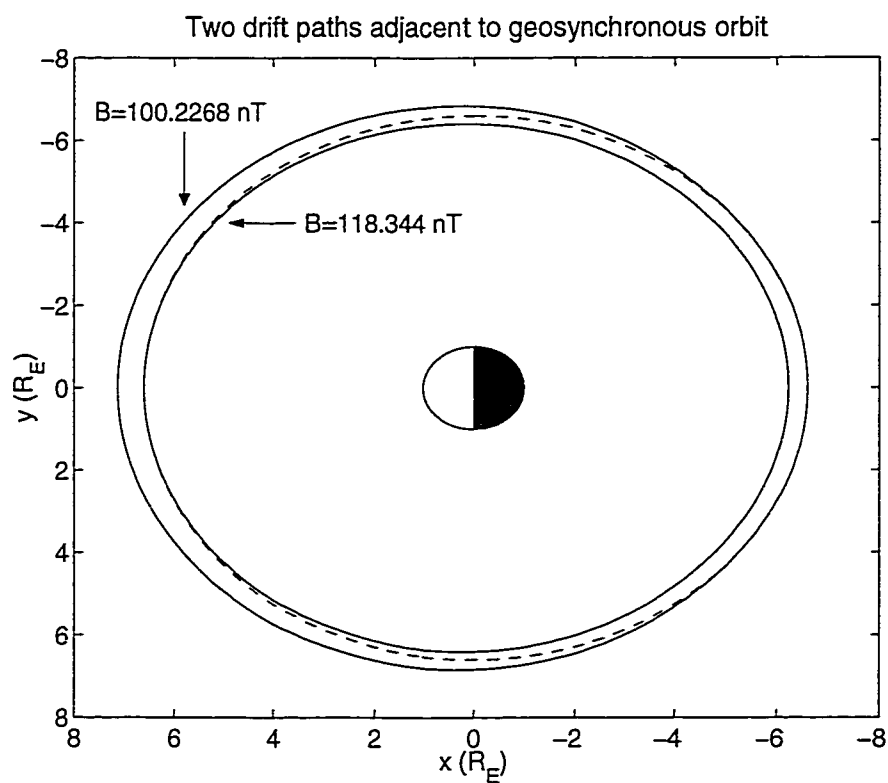


**Figure 3.8** Two  $L$ -shells adjacent to geosynchronous orbit: one at noon with magnetic field strength  $B = 118.3 \text{ nT}$  and the other at midnight with  $B = 100.1 \text{ nT}$  for DTH field model associated with  $Dst = 0 \text{ nT}$ .

model. Note the different magnetic field strengths for the two  $L$ -shells. The day-night asymmetry of the geomagnetic field results from day-side compression and night-side extension of the geomagnetic field (see Section 3.4). Figure 3.9 illustrates changes of  $L$ -values of drift shells adjacent to geosynchronous orbit for different local times (LT). Apparently, a geosynchronous spacecraft detects electrons on a lower  $L$ -shell when it passes near local noon. This leads to a large flux measurement due to the radial profile of energetic electron flux, as shown in Figure 2.10.

For comparison with measured fluxes we have calculated fully-adiabatic fluxes using  $Dst$  values for the storm of November 2–5, 1993. Figure 3.10(b) and 3.10(a) show the simulation results with and without taking the diurnal effect into account, along with the LANL measurements. The calculated electron fluxes are averaged over the energy range for each channel and normalized by the pre-storm value at UT = 0. This normalization accounts for the fact that the magnitudes of the pre-storm fluxes for the 1993 storm are slightly different from the CRRES fluxes which were used for our fit (by less than a factor of two for this event) and it facilitates the comparison of the calculated and measured fluxes.

As expected, variations in the calculated fluxes track changes in  $Dst$ . The calculations which include the diurnal effect remarkably reproduce the diurnal variations in the observed electron fluxes. Comparing the time series of the observed and calculated fluxes from UT=0 onward in time, we first notice that, just before the storm main phase (UT $\approx$ 45), the observed fluxes decrease significantly more than the simulation, indicating a non-adiabatic loss mechanism. The non-adiabatic loss is probably due to the drift shell of the synchronous orbit electrons intersecting the magnetopause, so those electrons are lost to the dawnside magnetopause and effectively replaced by lower fluxes of electrons from the duskside magnetopause. Generally, this can occur either because the magnetopause is compressed or because of the expansion of the synchronous orbit drift shell, or both.

Information on the standoff distance for the November 1993 storm can help verify whether the dayside magnetopause moved inside geosynchronous orbit at any time during the magnetic storm. Unfortunately, during the time of this event there were no direct measurements of solar wind conditions. The GEOTAIL data was used as a proxy, shifted in time using the solar wind speed. Using the available solar wind

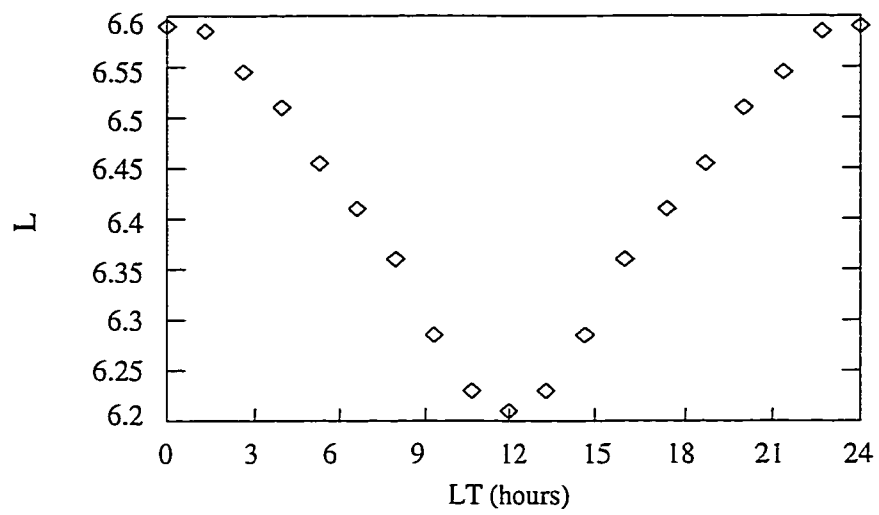


**Figure 3.9** Changes of  $L$ -values adjacent to geosynchronous orbit for different local times (LT).

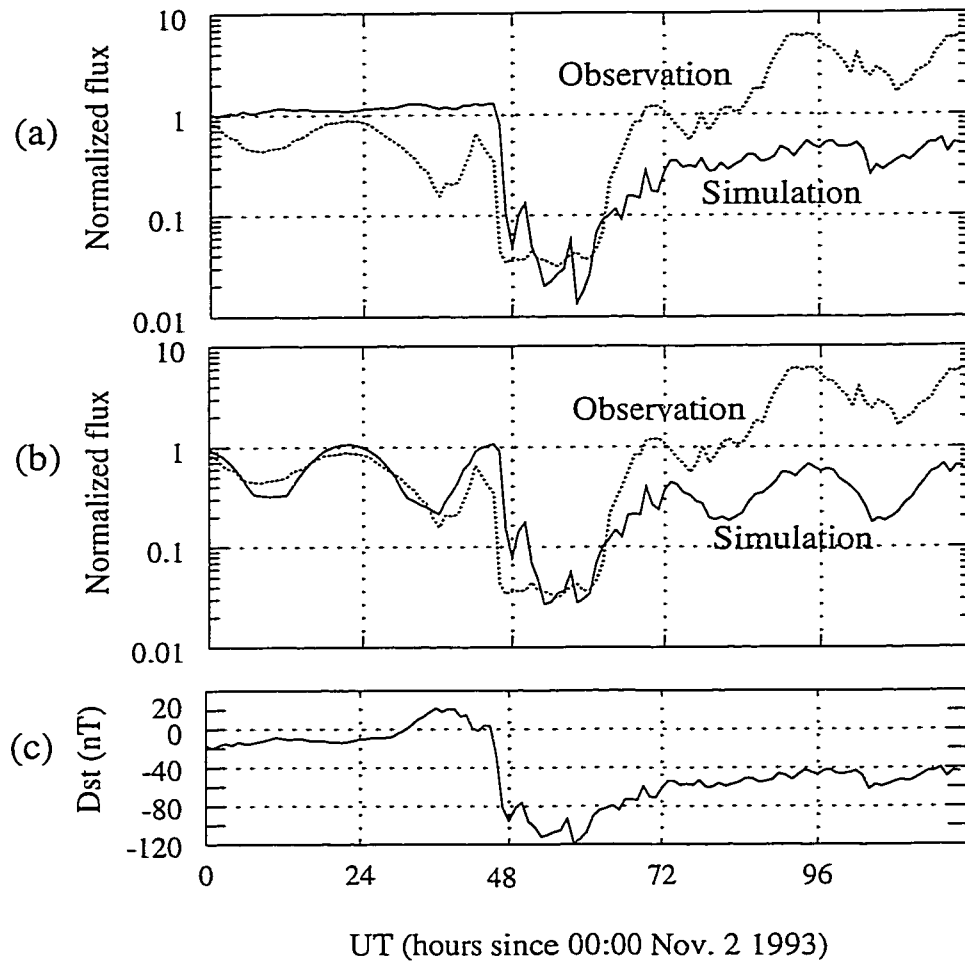


**Figure 3.10** Simulation results (a) without and (b) with taking the diurnal effect into account, along with the LANL measurements. (c) Corresponding *Dst* values.

conditions the standoff distance is calculated from the formula [Voigt, 1979]:

$$R_s = \left[ \frac{f B_0^2}{2\pi \rho_{sw} v_{sw}^2} \right]^{\frac{1}{6}} \quad (3.3)$$

where  $f = 1.35$ ,  $B_0$  the magnetic field strength in gauss at the equator on the Earth,  $\rho_{sw}$  is the solar wind mass density in  $\text{g/cm}^3$ , and  $v_{sw}$  is the solar wind velocity in  $\text{cm/s}$ . Figure 3.11 shows solar wind density, velocity, and the calculated standoff distance for  $30 < \text{UT} < 72$ , and the corresponding  $Dst$  for longer time period. At early main phase, there are times when the standoff distance is smaller than 6.6, indicating that the magnetopause moved inside geosynchronous orbit. Therefore if we assume the solar wind parameters used in this calculation are reliable, the pre-main phase decreases of electron flux are due to magnetopause loss.

During the main phase, although the magnitude of the decrease in the calculated fluxes is comparable to the overall decrease in the observed fluxes, it is not clear how much of the observed decrease is due to the dayside magnetopause loss and how much is possibly due to the fully-adiabatic effect. We plan to incorporate this magnetopause loss mechanism in future calculations but we specifically exclude it in this work, partly for simplicity and partly to isolate the flux-decrease effect of the fully-adiabatic response. Without taking the magnetopause loss into account the magnitude of the simulated flux in the early recovery phase ( $\text{UT} \approx 50-60$ ) seems to agree with the observation, but this is probably because the observed flux has dropped to the background level of the detector (without the background the observed flux would be lower than the simulation).

After the minimum at  $\text{UT} \approx 60$ , the observed electron fluxes steadily increase, apart from the diurnal variation. A feature which is seen in both the observed fluxes and  $Dst$  is the higher rate of increase between  $\text{UT} \approx 60$  and  $\text{UT} \approx 72$ , compared to  $\text{UT} \gtrsim 72$ . Overall, although the dominant mechanisms for the observed flux changes are non-adiabatic, for this event there is good evidence for significant adiabatic,  $Dst$ -driven flux changes.

As pointed out by *Freeman et al.* [1998], there is a notable energy dispersion in the recovery phase flux enhancement; the lowest-energy electron flux recovers to its pre-storm value first, followed by higher-energy fluxes. According to *Freeman et al.* [1998] the observed energy dispersion may result from the energy dependence of the gradient

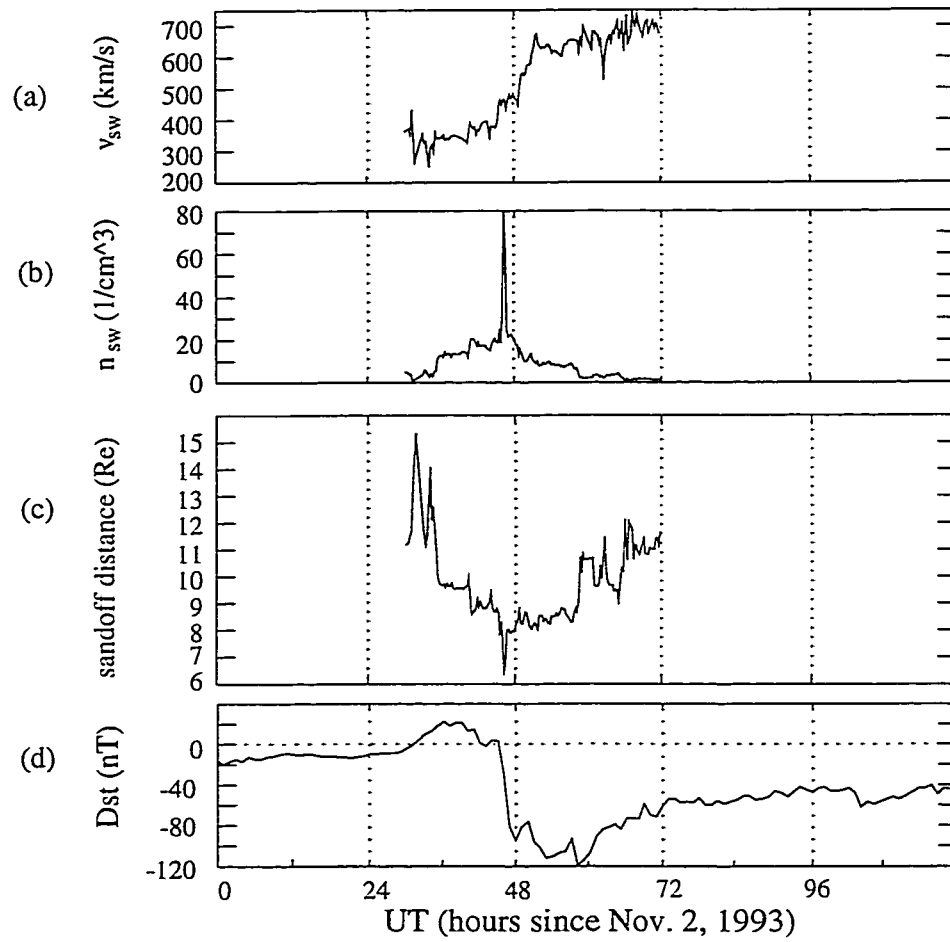


**Figure 3.11** (a) Solar wind velocity  $v_{sw}$ . (b) Solar wind density  $n_{sw}$ . (c) Standoff distance. (d) Corresponding  $Dst$  values.

and curvature drifts: the gradient and curvature drift gives larger azimuthal drift to higher energy electrons, so lower energy electrons arrive first at geosynchronous orbit due to the  $\mathbf{E} \times \mathbf{B}$  drift before their longitudinal drift by the gradient and curvature drifts becomes significant, resulting in a dispersion in energy.

During the recovery phase the fully-adiabatic electrons which appear at geosynchronous orbit have come from larger  $L$ -shells at earlier times; if it turns out that one of those  $L$ -shells would have been outside the trapping boundary then those electrons would be lost and effectively replaced with electrons from the trapping boundary distributions. We note that a similar effect can occur if the actual storm-time particle distribution on a large  $L$ -shell is significantly different from the adiabatically-evolved pre-storm distribution, even if it is within the trapping boundary. Thus, there is a time in the recovery phase beyond which the fully-adiabatic fluxes are not the pre-existing synchronous orbit fluxes which we use in our calculation. This time can be calculated by asking for what value of  $Dst$  the synchronous orbit magnetic flux surface first intersects the DTH trapping boundary at the minimum of  $Dst$  for a given storm. We then use the  $Dst$  time series to find the corresponding recovery-phase time. We find that the electrons that appear at geosynchronous orbit for  $Dst = -94$  nT have drifted on the last closed constant  $B$  contour for the minimum  $Dst = -119$  nT.  $Dst = -94$  nT corresponds to a recovery-phase time of UT  $\sim 61$ ; hence the calculated flux values for UT  $\gtrsim 61$  should be disregarded or (better) replaced with fluxes corresponding to the trapping boundary distribution. Since this process could occur quite early in the recovery phase (in agreement with the conventional wisdom that synchronous orbit can be close to the trapping boundary, especially during storms) we conclude that any calculation of the fully-adiabatic evolution of pre-existing inner-magnetospheric particle fluxes, such as this work, is primarily applicable to the main phase flux decrease and the very early recovery phase only.

### 3.4 Summary and discussion

We have systematically investigated the fully-adiabatic response of relativistic electrons to changes of the magnetic field configuration during a storm. Specifically, we have calculated equatorially-mirroring relativistic electron fluxes by adiabatically evolving pre-storm electron fluxes during a geomagnetic storm. We use Liouville's

theorem and the conservation of the first and the third adiabatic invariants. For an electron with given storm-time energy and  $L$ -value, the corresponding pre-storm values are calculated for different levels of geomagnetic activity corresponding to different  $Dst$  values. The pre-storm electron fluxes are obtained from a fit to CRRES measurements of differential flux as a function of energy and  $L$ -value,  $j(E, L)$ . The CRRES data was fitted as an exponential function of quadratic polynomials of energy and  $L$  for a restricted range of energy and  $L$ .

For a given storm-time energy at geosynchronous orbit, the pre-storm energy increases roughly linearly with decreasing  $Dst$ , while the pre-storm  $L$ -value decreases roughly linearly with decreasing  $Dst$ . Because the quiet-time electron flux decreases exponentially with energy, the calculated fully-adiabatic fluxes showed the observed similarity between the logarithm of electron flux and  $Dst$ . The fully-adiabatic electron fluxes also reproduce the observed energy dependence of the size of the storm-time electron flux decreases. Larger flux decreases occur for lower energies with strong dependence on the strength of geomagnetic activity. Figure 3.6 shows calculated flux decreases for 1–2 MeV electron fluxes at synchronous orbit for a range of  $Dst$  values.

From comparison with measured electron fluxes for the November 1993 storm (Figure 3.10) we conclude that the fully-adiabatic effect may account for a significant fraction of the observed electron flux decrease at the storm main phase, but other effects such as loss to the magnetopause may also contribute. Because drift trajectories at synchronous orbit can become open during a storm, especially near the end of the main phase and the early recovery phase, the fully-adiabatic evolution of pre-storm trapped particle distributions should not generally be used to predict recovery phase fluxes, although this may be possible for weaker storms. Rather, the recovery-phase fluxes are expected to be from a storm-time outer-magnetosphere distribution, with contributions from the duskside magnetopause and the magnetotail. This raises the interesting possibility that the fully-adiabatic radial motion of electrons from these outer-magnetosphere distributions can contribute to the observed MeV electron flux increases at synchronous orbit. Calculation of this effect requires a careful treatment of the magnetopause, models of outer-magnetosphere electron fluxes and further comparisons with energetic electron flux measurements.

In order to make detailed comparisons with geosynchronous spacecraft measurements there are two further effects which should be included in our calculations: the effect of solar wind conditions (we used a fixed standoff distance, neglecting variations of solar wind conditions), and the effect of the tilt of the Earth's magnetic field (we neglected the difference between the magnetic and the geographic equatorial planes). In future work we plan to incorporate these effects and compare fully-adiabatic fluxes with measured fluxes for a number of storms. Such comparisons will help to determine when and where non-adiabatic processes are occurring. The methods of this work can also be extended to non-equatorially-mirroring electrons, allowing comparison with observed pitch-angle distributions. Finally, the identification of the physical mechanisms responsible for flux increases to values well above the pre-storm levels is an important remaining question which will be addressed in following chapters.

## Chapter 4

### Delayed substorm injection mechanism

#### 4.1 Introduction

Many studies have been devoted to understanding the mechanism(s) accounting for the strong enhancements of relativistic electron flux in the outer-radiation belt. Some of the proposed mechanisms were briefly reviewed in Section 1.3. In this work, we investigated one potential acceleration mechanism, so-called “delayed substorm injection and acceleration of plasma sheet electrons”. Large MeV electron flux increases with a characteristic time scale of about one day are of particular interest [*Baker et al.*, 1994b, 1997a; *Li et al.*, 1997b] (refer Section 1.2). The plasma sheet is a region of potentially strong electron acceleration because of its relatively high density of energetic electrons ( $\sim$  tens of keV) and the active field dynamics in the magnetotail during disturbed times.

Substorm-associated energetic particle injections are a well-known phenomena and have been extensively studied [*Sergeev et al.*, 1998, and references therein]. It has been established that sharp flux increases of electrons with energies of tens to hundreds of keV at synchronous orbit are associated with the onset of the substorm expansion phase [*Belian et al.*, 1981]. Except on very rare occasions, flux increases of MeV electrons at synchronous orbit are not observed at the same time as the increases of the fluxes of electrons with tens to hundreds of keV that appear to be direct product of substorm activity [*Baker et al.*, 1978; *Nishida*, 1983]. In this work we examine whether the substorm associated acceleration followed by a delayed injection process can account for the flux enhancements of MeV electrons that are observed to occur on one-day time scales in the geosynchronous region during magnetic storms. We specifically consider substorm acceleration of energetic plasma sheet electrons followed by inward radial transport on a one-day time scale.

*Birn et al* [1997,1998] have investigated acceleration and injection of both proton and electrons, using test particle traces in three-dimensional MHD fields. These simulations include tail reconnection, plasmoid ejection, and collapse of the inner tail. The

*Birn et al* [1997,1998] test particle simulations were able to explain the main features of the initial rise of the particle injection at geosynchronous orbit. They found that most energization results from betatron acceleration, as particles are transported into a strong magnetic field region by a time dependent electric field that is predominantly in the dawn-to-dusk direction. This work focused on the prompt dispersionless injection of electrons with tens to hundreds of keV, within minutes of substorm onset. In our study we use similar methods to investigate the effects of a substorm on electrons in the high-energy tail of the plasma sheet that can be transported to trapped orbits, then subsequently transported to synchronous orbit on one-day time scales. Like *Birn et al* [1997,1998] we trace test particle trajectories in the three-dimensional dynamic MHD fields from *Birn and Hesse* [1996], but we consider plasma sheet electrons with about ten times higher energy, and we use a more sophisticated particle tracing code. More specifically, we are interested in the substorm acceleration of plasma sheet electrons to energies of a few hundred keV at  $r \sim 10R_E$ , which corresponds to  $\sim 1$  MeV at geosynchronous orbit, if the first invariant is conserved. The particle tracer [*Birn et al.*, in preparation] can follow particles of any pitch angle by integrating either the full equation of motion or the guiding center equation, depending on a validity condition for the drift approximation. (The test-particle tracer of *Birn et al.* [1998] assumed equatorially-mirroring particles). Use of the enhanced particle tracer is especially important for our situation, because electrons near the neutral sheet can break the first adiabatic invariant, especially in the region near the X-line.

We integrate electron orbits until they reach the boundary of the simulation box or the final state of the MHD field simulation. Electron test particles in our energy range are usually not transported from  $\sim -20R_E$  to geosynchronous orbit in the single injection. Rather, when an electron reaches  $x \sim -10R_E$  before drifting out to the boundary, we assume that it has a good chance of subsequent earthward transport to geosynchronous orbit. Some kind of wave-induced radial diffusion may be invoked for the subsequent earthward transport. The detailed investigation of the subsequent radial transport is outside the scope of this thesis.

In this study, we concentrate primarily on two questions:

- Can substorms accelerate plasma sheet electrons that can potentially contribute to relativistic electrons at the geosynchronous region?

- Can this process produce enough particles to provide the observed sharp increases of electron fluxes?

The following sections briefly describe the particle tracer and the dynamic electric and magnetic fields from the three-dimensional MHD simulation of the substorm. Chapter 5 then presents the results of the test particle trajectory studies and estimates the relativistic electron flux in the inner magnetosphere that can be produced by the substorm injection.

## 4.2 What is the delayed substorm injection mechanism?

The magnetospheric substorm is a basic dynamic process of the magnetosphere. Substorms occur frequently, often just a few hours apart. On Earth the most visible sign of a substorm is a great increase of polar auroras in the midnight sector. A substorm occurs in the magnetosphere and ionosphere after the interplanetary magnetic field (IMF) turns southward and increased energy flows from the solar wind into the magnetosphere. The combination of high speed solar wind and strong southward IMF drives intense substorm activity at the leading edge of the solar wind stream. This produces energetic electrons in the energy range of tens to a few hundreds of keV in the outer radiation belt [see *Baker et al.*, 1978; *Nishida*, 1983, and references therein]. *Baker et al.* [1997b] noted that the energy spectra of outer-belt electrons hardens some days after the substorm activity peaks, as illustrated in Figure 4.1. The solid line shows the enhancement of relatively low energy electrons in response to the substorm activity and the dashed line shows the spectral hardening when the solar wind speed decreases. The intense relativistic electrons appear some days after the leading edge of the solar wind stream has passed the Earth (see Figure 4.2). This suggests that a substorm-associated acceleration process may act to produce the relativistic electrons in the outer-radiation belt.

A possible explanation for the delayed arrival of relativistic electrons in the outer belt is that substorms accelerate plasma sheet electrons to energies of hundreds of keV and inject them to  $r \sim 10R_E$ , where they may execute trapped orbits about the Earth. Once on a trapped orbit and able to stay in the magnetosphere for an extended period, an electron may be transported earthward and further accelerated

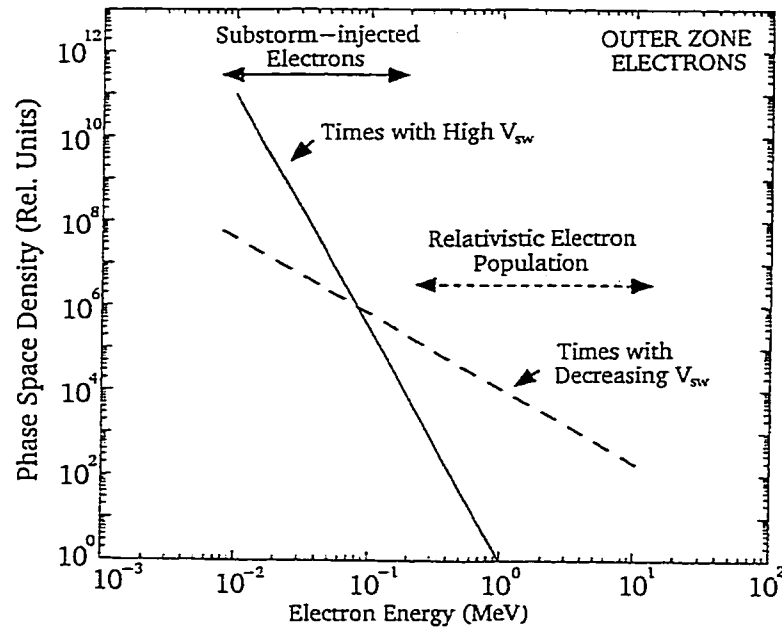


**Figure 4.1** A schematic representation of the electron phase space density variations seen during recurrent solar wind stream events. The outer zone energetic electron spectrum systematically shifts during the time that solar wind speed peaks and then subsides. Substorms initially produce many relatively low energy electrons, some of which subsequently get boosted to higher energies (adapted from *Baker et al.* [1998b]).

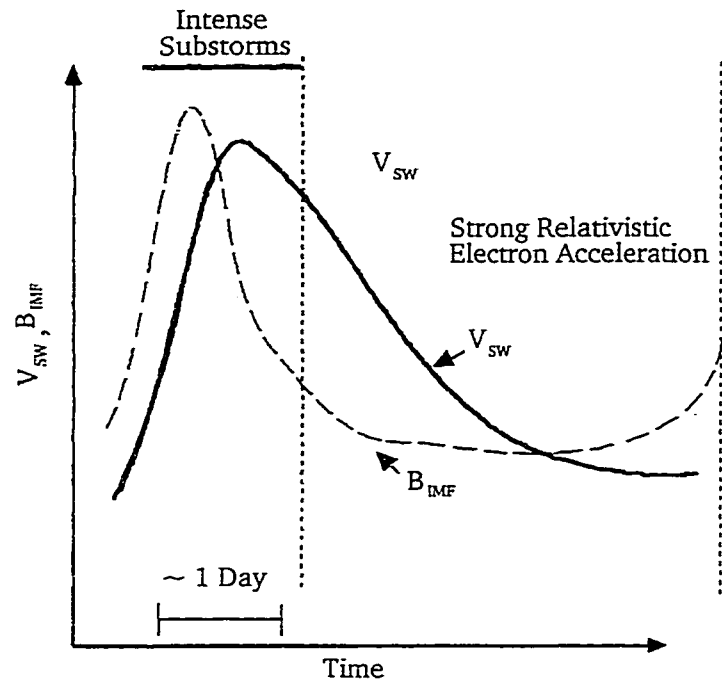


**Figure 4.2** A schematic showing a typical high-speed solar wind ( $V_{sw}$ ) profile (solid curve) and the associated interplanetary magnetic field ( $B_{IMF}$ ) profile (dashed curve). The combination of high  $B$  and large  $V_{sw}$  at the leading edge of the stream can drive strong substorm activity. In the time period of declining  $V$ , there is strong acceleration of relativistic magnetospheric electrons (adapted from *Baker et al.* [1998b]).

by a slower diffusive process. The central question with regard to this mechanism is the following: Can a plasma sheet electron be transported to the inner magnetosphere and, in the process, be accelerated to relativistic energies?

A region of strong induction electric field develops in association with the collapsing magnetic fields in the tail during a substorm. When encountering the strong westward induction electric fields, energetic ( $\sim$  tens of keV) plasma sheet electrons can undergo substantial earthward radial transport by the enhanced  $\mathbf{E} \times \mathbf{B}$  drift. If the radial transport is “faster” than bounce-averaged cross-tail drift, the electrons can be injected to the trapped region before drifting out to the magnetopause. A simple betatron acceleration would give up to a factor of  $\sim 100$  energy gain for an injection from  $r \sim 20R_E$  with a 1 nT field to  $r \sim 6.6R_E$  with a 100 nT field. Figure 4.3 illustrates a sample trajectory of a plasma sheet electron that could contribute to inner-magnetospheric fluxes. Test particle simulations will be used to investigate how effectively this mechanism can produce the outer-belt MeV electrons.

### 4.3 The resistive MHD field model

Theory and simulations of the dynamic magnetotail are often based on resistive magnetohydrodynamics (MHD), including compressibility. The field simulation solves the non-linear time dependent MHD equations:

$$\frac{\partial \rho}{\partial t} = -\nabla \cdot (\rho \mathbf{v}) \quad (4.1)$$

$$\frac{\partial \rho \mathbf{v}}{\partial t} = -\nabla \cdot \left( p + \frac{B^2}{2\mu_0} \right) - \nabla \cdot \left( \rho \mathbf{v} \mathbf{v} - \frac{\mathbf{B} \mathbf{B}}{\mu_0} \right) \quad (4.2)$$

$$\frac{\partial p}{\partial t} = -\nabla \cdot (p \mathbf{v}) - (\gamma_s - 1)p \nabla \cdot \mathbf{v} + (\gamma_s - 1)\eta j^2 \quad (4.3)$$

$$\frac{\partial \mathbf{B}}{\partial t} = -\nabla \times (\mathbf{v} \times \mathbf{B} - \eta \mathbf{j}) \quad (4.4)$$

Here standard international (SI) units and standard notations are used :  $\rho, p, \mathbf{v}$ , and  $\mathbf{B}$  represent the plasma density, pressure, velocity, and the magnetic induction, respectively;  $\eta$  denotes the resistivity and  $\gamma_s$  the ratio of specific heats. For an isotropic pressure in the absence of heat flux,  $\gamma_s = 5/3$ .

Rather than attempting global simulations of the entire magnetosphere/solar-wind/ionosphere system, the MHD simulation of *Birn and Hesse [1996]* focuses on

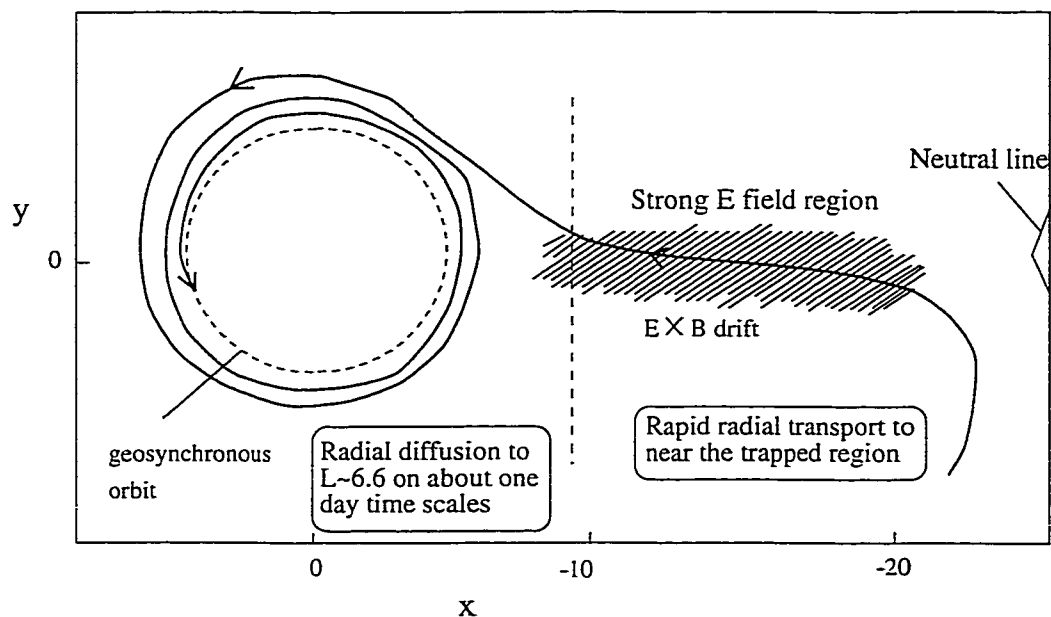


**Figure 4.3** A cartoon illustrating the substorm-associated injection and acceleration of plasma sheet electrons that are initially near the substorm neutral line. If particles encounter the region of rapid magnetic-field collapse, they can be transported rapidly earthward in the strong  $\mathbf{E} \times \mathbf{B}$  drift, before they have a chance to gradient drift eastward out of the tail. During the earthward transport, electrons can be accelerated to relativistic energy in the synchronous region.

the tail region and attempts to separate directly-driven effects from those of unstable energy release. The simulations start from a three dimensional realistic tail equilibrium obtained through relaxation from an initial non-equilibrium state. This approach is used to include the important transition region between the tail and the dipole field.

The simulation consists of two phases, a “growth phase” of externally driven current sheet thinning from  $t = -8\text{min}$  to  $t = 0$  and a “breakup” or “expansion” phase of dynamic evolution initiated at  $t = 0$  by imposing finite resistivity. During the growth phase an external (dawn to dusk) electric field is applied at the high latitude boundary of the simulation box. The associated inflow of magnetic flux peaks at midnight and falls off to zero at the flanks. It is applied only over a finite period, leading to an increase of the lobe field strength by 50% at  $x = -5R_E, y = 0$ . The most significant consequence is the formation of a thin current sheet in the near tail with a current density enhancement by a factor of about 5. This thin-current-sheet formation appears to be characteristic for the late growth phase and is presumably crucial for the onset of an instability that initiates the breakup phase. In the MHD simulation the breakup of this current sheet is initiated by imposing finite(uniform) resistivity. The  $(x', y', z')$  coordinate system used in the MHD field simulation is related to GSM coordinates  $(x, y, z)$  as follows:  $x' = -x - 5$ ,  $y' = -y$ , and  $z' = z$ . Throughout the thesis we will use GSM coordinates  $x, y$ , and  $z$ . The MHD simulation region covers  $-65R_E \leq x \leq -5R_E, 0 \leq y \leq 10R_E$ , and  $0 \leq z \leq 10R_E$ , with a dipole (outside the simulation box) at  $x = 0, y = 0, z = 0$ , assuming symmetry around  $y = 0$  and  $z = 0$ . The boundary conditions for the simulations of the energy release phase consist typically of solid, ideally conducting walls at each of the boundaries. No external electric field is imposed for the simulations of the unstable release process; all velocity components are set to zero except at the distant boundary in  $x$ , where a free outflow condition is assumed. Neumann boundary conditions ( $\partial/\partial n = 0$ ) are imposed on density, pressure, and the tangential magnetic field components, while the normal magnetic field is held fixed, except at the distant boundary, where  $B_y$  and  $B_z$  are convected with the plasma fluid. The grid consists of  $32 \times 20 \times 32$  cells for the full system. The grid size is uniform in  $x$  and  $y$ , but nonuniform in  $z$ , increasing from a spacing of 0.0625 around  $z = 0$  to  $\sim 1.5$  near  $|z| = 10R_E$ . The MHD run writes

out the electric and magnetic field values at time steps of 0.25 Alfvén times ( $\sim 1.5$  seconds).

Figures 4.4 to 4.6 illustrate the time evolution of electric and magnetic fields from the MHD simulation, showing 3-dimensional plots of equatorial values of  $E_y$  and  $B_z$  and magnetic field lines in  $x-z$  plane. Figure 4.7 shows the time evolution of  $B_z$  and  $E_y$  along the  $x$ -axis. The time at which resistivity is imposed is defined as  $t = 0$ . No external electric field is applied for  $t > 0$ . At  $t \sim 2$  min after the imposition of the resistivity, a neutral line forms at  $x \approx -23R_E$  from the center of the Earth dipole. At  $t \sim 5$  min, the electric field starts to change rapidly, leading to peak  $E_y$ -values of 10 – 20 mV/m. Interestingly, the largest values of  $E_y$  develop in the magnetic-field-collapse region, well earthward of the neutral line. The magnetic field also increases dramatically in that region. At  $t \sim 8$  min, dipolarization is clearly seen in the inner tail region. The region of strong  $E_y$  extends from  $x = -18R_E$  to  $-12R_E$ , and its maximum moves earthward.

#### 4.4 The particle tracer

The dynamics of a single charged particle in the non-zero electric and magnetic fields are governed by the Lorentz equation :

$$\frac{d\mathbf{p}}{dt} = \frac{e}{c} \frac{d\mathbf{r}}{dt} \times \mathbf{B}(\mathbf{r}, t) + e\mathbf{E}(\mathbf{r}, t) \quad (4.5)$$

where  $\mathbf{r}$  is the particle position,  $\mathbf{p}$  is its relativistic momentum  $\gamma m\mathbf{v}$ , and  $\mathbf{B}$  and  $\mathbf{E}$  are the magnetic and electric fields. When the first adiabatic invariant  $\mu$  is constant, the particle dynamics can be described by the motion of its guiding center. The relationship between the position of guiding center  $\mathbf{R}$  and the particle location  $\mathbf{r}$  is given as  $\mathbf{r} = \mathbf{R} + \boldsymbol{\rho}$ , where  $\boldsymbol{\rho}$  is a vector from the guiding center to the particle, given as  $\mathbf{p} \times \mathbf{B}/qB^2$ .

One can summarize the guiding center drifts that arise in particle motion as follows:

$$\mathbf{V}_\perp = c \frac{\mathbf{E} \times \mathbf{B}}{B^2} + \frac{m\gamma v_\perp^2 c}{2qB^3} (\mathbf{B} \times \nabla B) + \frac{m\gamma c v_\parallel^2}{qB^4} [\mathbf{B} \times (\mathbf{B} \cdot \nabla) \mathbf{B}] \quad (4.6)$$

The first term represents a  $\mathbf{E} \times \mathbf{B}$  drift, which is perpendicular to both the electric and magnetic fields; its magnitude is inversely proportional to the magnitude of  $\mathbf{B}$ . The

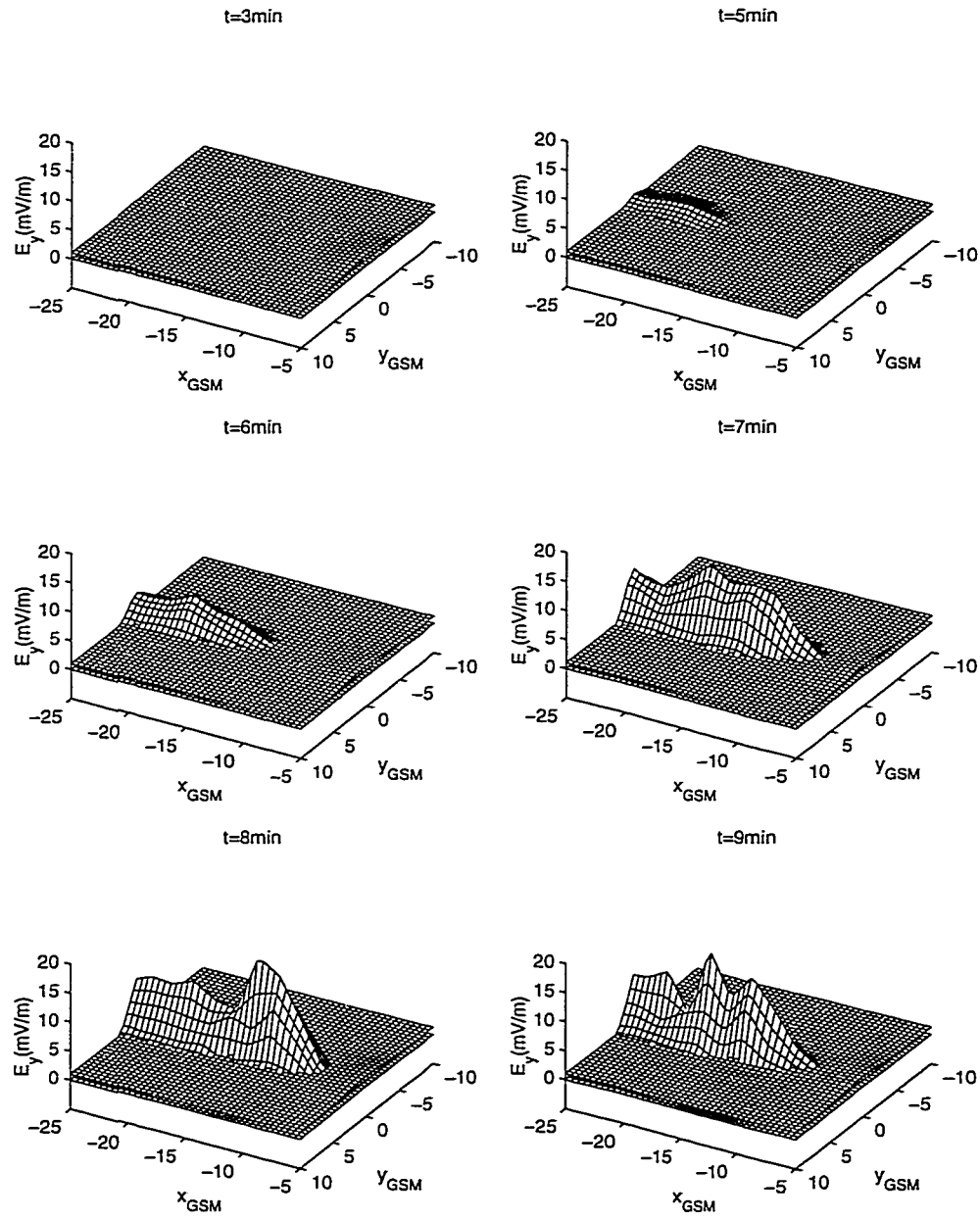


Figure 4.4 3-dimensional plots of  $E_y$  in the equatorial plane.

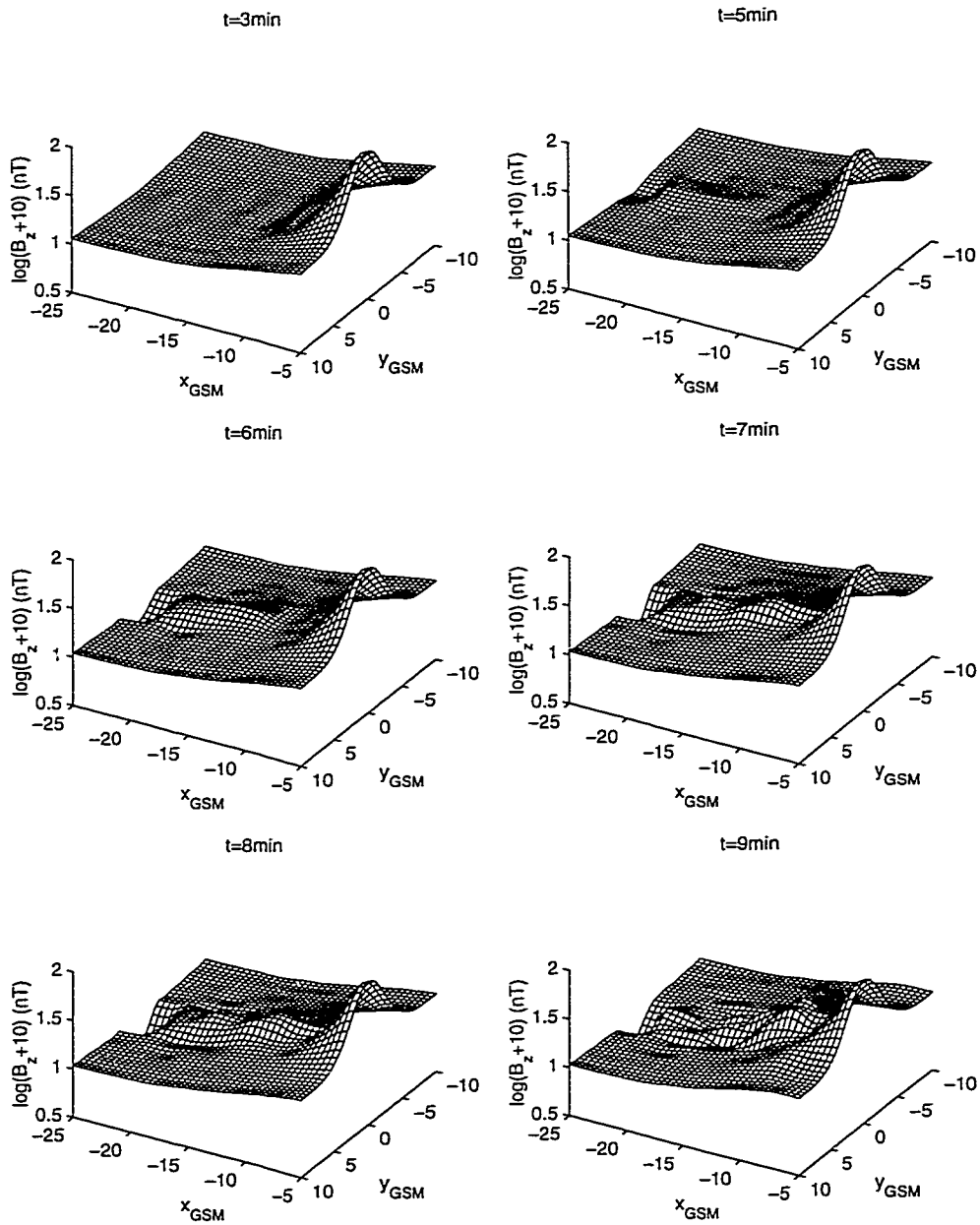


Figure 4.5 3-dimensional plots of  $B_z$  in the equatorial plane.

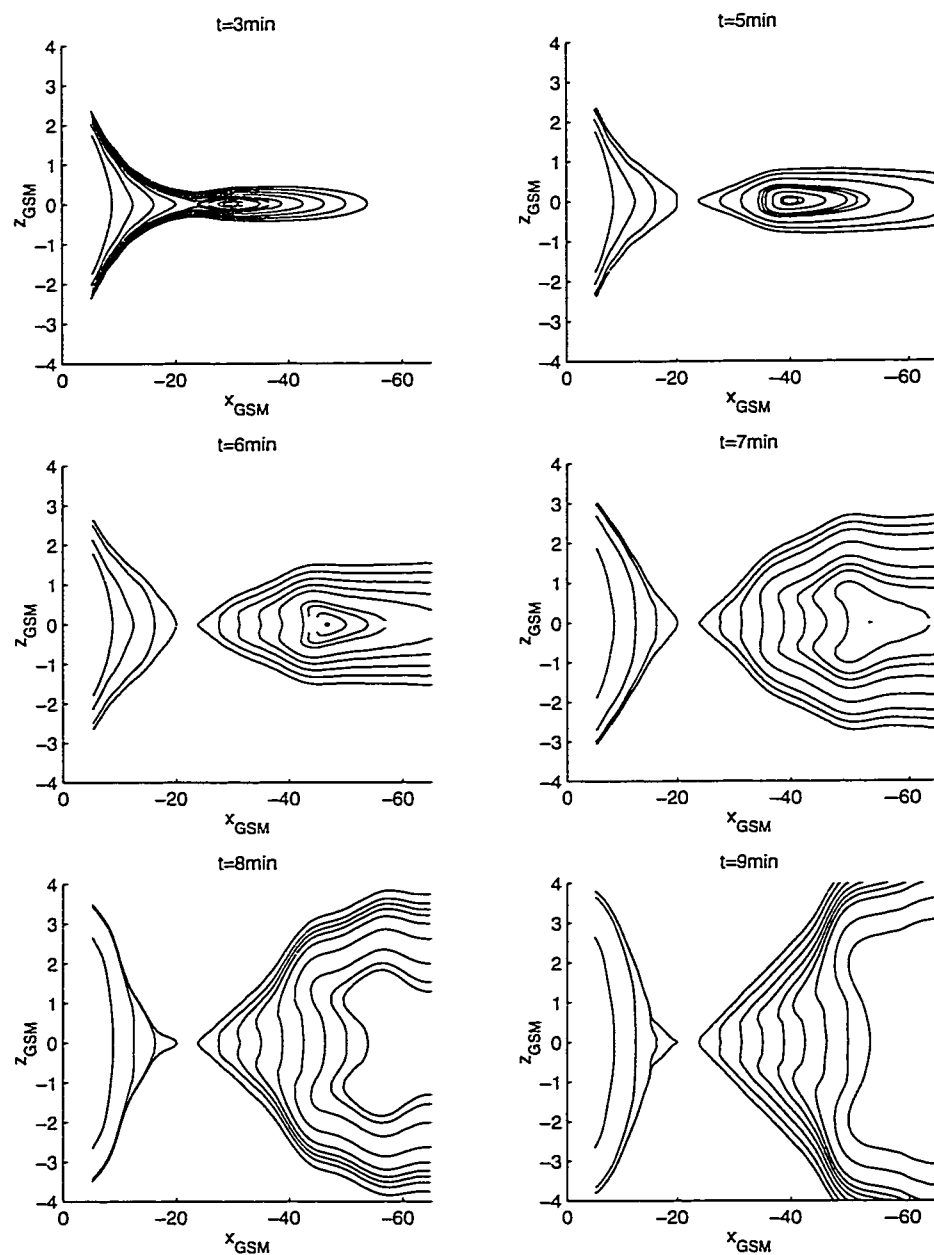
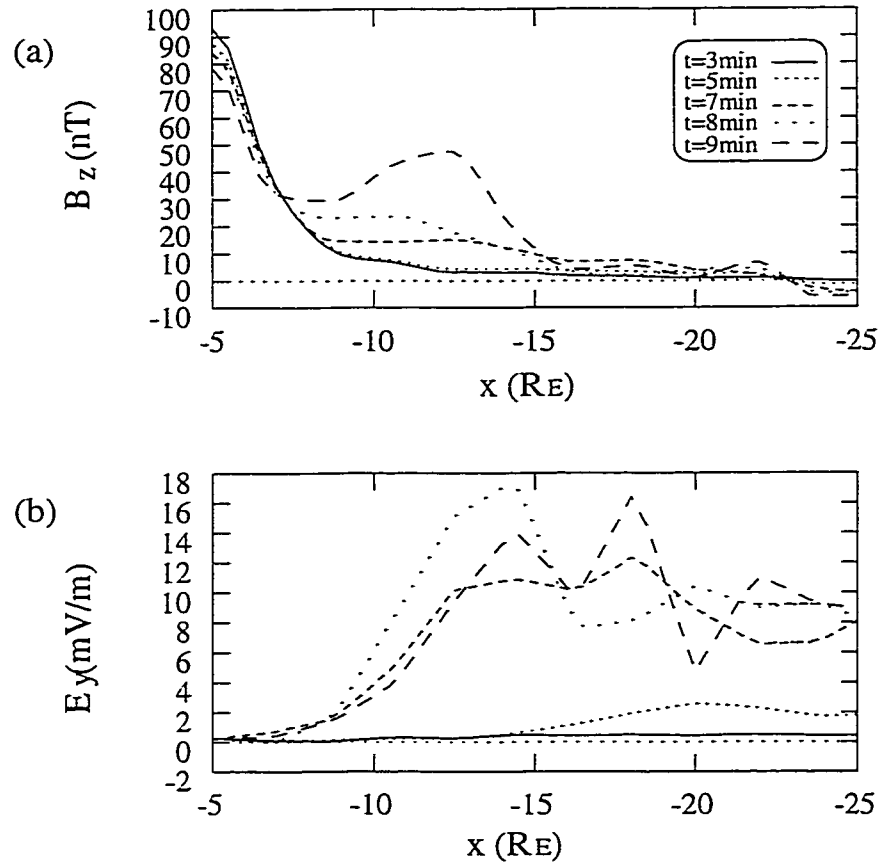


Figure 4.6 Magnetic field lines in the noon meridional plane.



**Figure 4.7** (a) Variations of  $B_z$  along  $x$ -axis and (b)  $E_y$  along  $x$ -axis for  $t = 3, 5, 7, 8$ , and 9 minutes.

second term represents a gradient drift which depends on the sign of the particle's charge, and so this drift will cause electric currents to flow across the magnetic field. And the third term gives the curvature drift, where the radius of curvature  $R_c$  is defined as  $\hat{n}/R_c = -(\hat{b} \cdot \nabla)\hat{b}$  with  $\hat{b}(= \mathbf{B}/B)$  a unit vector of  $\mathbf{B}$ . The last two drift terms are energy-dependent.

The particle tracer checks a validity condition for the guiding-center-drift approximation, and then solves either the guiding-center equation or the full Lorentz equation of motion. The drift approximation breaks down when the gyroperiod becomes comparable to the characteristic time for the field evolution, or when the gyroradius becomes comparable to the characteristic length scale of the underlying electric and magnetic field. In the evaluation of the second condition, we find that in general cases the shortest characteristic length scale is typically the magnetic field curvature radius at the equator. *Büchner and Zelenyi* [1989] introduced a  $\kappa_{orb}$  parameter, defined as the square root of the ratio of the minimum curvature radius of the magnetic field to the maximum Larmor radius, i.e.,  $\kappa_{orb}^2 = R_{c,min}/r_{L,max}$ . In our study the validity condition of the drift approximation is given by  $\kappa_{orb} \gtrsim 10$ . In the vicinity of the neutral line (located near  $x = -23R_E$ ) the drift approximation typically breaks down because the gyroradius becomes comparable to the curvature radius of the magnetic field at the equator (see Figure 4.8). In fact, one can see from the test-particle orbits that electron motion is highly non-adiabatic in the region near the neutral line, so that full orbit tracing is required.

At the near-Earth boundary particles were reflected back into the box, simulating mirroring closer to the Earth, but neglecting the loss cone and the short flight time from the boundary to the actual mirror point and back. The instantaneous local electric and magnetic fields were interpolated from the results of the MHD run, which were stored for time steps of 0.25 Alfvén times (corresponding to approximately 1.5 seconds). Consistency between the magnetic field gradients and the interpolated fields and continuity at the boundaries of the grid boxes require that the magnetic field be interpolated by third-order polynomials in the space coordinates. Since this can introduce spurious non-monotonic variations of the interpolated variables when the fields vary rapidly in space, a monotonicity-preserving algorithm was used to constrain the derivatives of  $\mathbf{B}$  [Hyman, 1983]. The electric field was interpolated

linearly in space. All field values were linearly interpolated in time. The numerical integration of the drift equations was performed using Gear's method for stiff ordinary differential equations. We checked the accuracy by integrating orbits in stationary magnetic fields on the same grid and found that the energy is conserved to within a few percent.

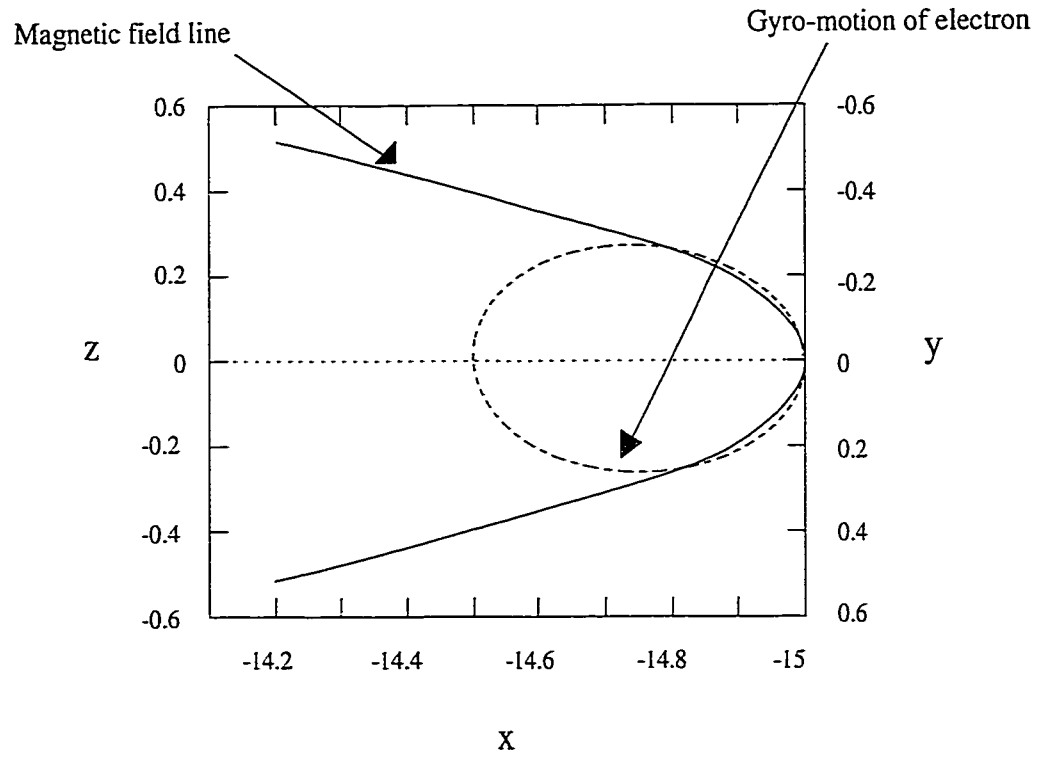


**Figure 4.8** A plot of a magnetic field line (in  $x - y$  plane) overlapped with a plot of a Larmor circle for the field configuration at  $t \sim 5$  min.

## Chapter 5

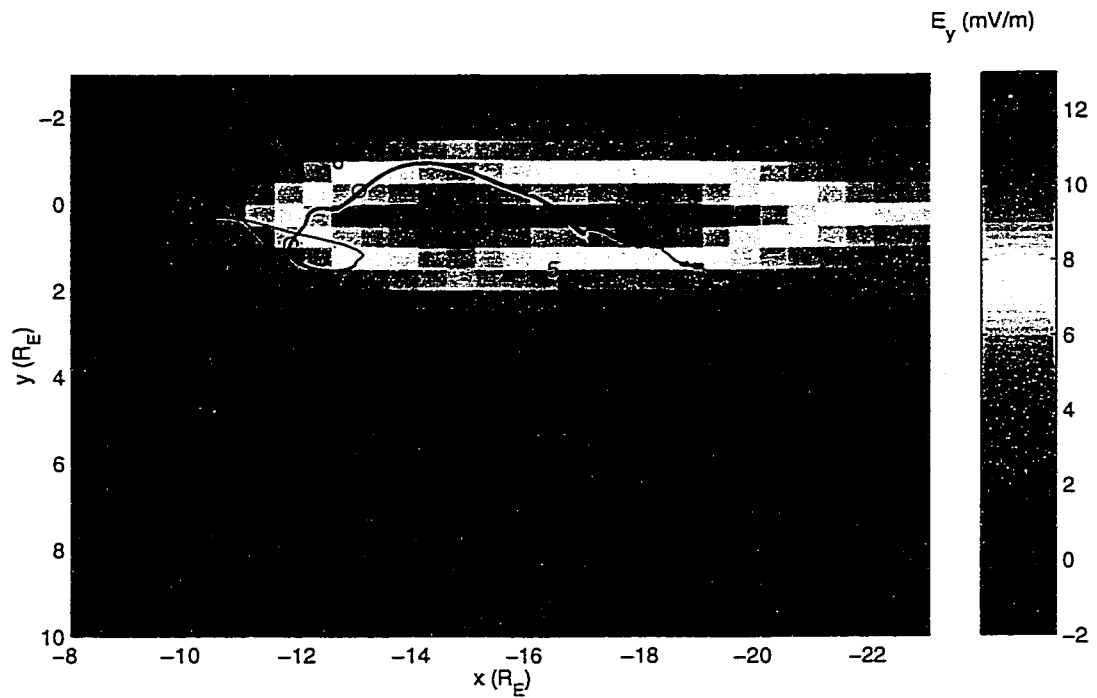
### Results for the substorm injection mechanism

#### 5.1 Characteristics of sample electron orbits

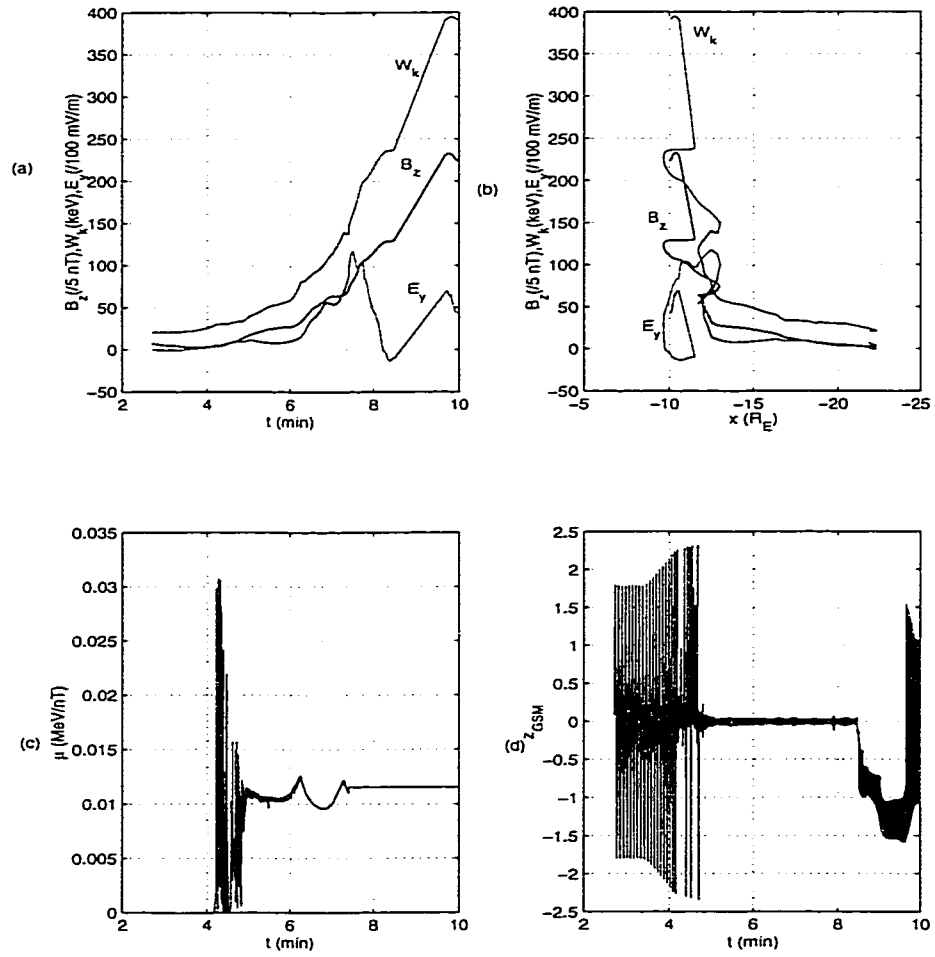
We started test-particle tracings at times and locations where the magnetic field was changing rapidly and induction electric fields were strong. Electrons were traced both forwards and backwards in time from the starting point. After experimenting with various initial conditions, we found that this way of tracing facilitated finding the electrons that undergo significant energization from strong electric fields as they were transported earthward from the tail (to  $x \sim -10R_E$ ). We often chose particles with equatorial pitch angles near 90 degrees, because they are the ones that gained the most energy: those particles spent most of their time near the equatorial plane, where the induction electric field was largest.

Figure 5.1 shows the equatorial crossing points of a representative electron trajectory. The electron first drifted from the duskside boundary toward midnight and toward the Earth. When it encountered the strong induction electric field, its earthward motion was accelerated by strong  $\mathbf{E} \times \mathbf{B}$  drift. During that Earthward drift, the electron gained energy more rapidly than it did in its earlier drift across the tail. The particle tracing stopped at the end-time of the MHD simulation ( $t = 10$  min); by then the electron had reached  $x \approx -10R_E$ .

Figure 5.2 exhibits various parameters for the particle of Figure 5.1. The plots of kinetic energy,  $W_k$ , versus time in Figure 5.2(a) and versus  $x$  along the trajectory in Figure 5.2(b) show when and where the most of energization occurred. Initially the electron entered from the dusk-side boundary in the far tail with energy  $W_k \sim 20$  keV. It gained energy slowly until  $t \sim 5$  min, when it was just outside the actively dipolarizing region. The particle then gained energy rapidly during its earthward injection by  $\mathbf{E} \times \mathbf{B}$  drift, with final energy  $W_k \sim 400$  keV at  $t = 10$  min. Changes in the instantaneous magnetic field  $B_z$  and electric field  $E_y$  values along the trajectory are also plotted in Figure 5.2(a) and (b), illustrating how the field configuration varied along the drift path. The time profile of  $W_k$  resembles that of  $B_z$ , because



**Figure 5.1** Equatorial crossing trajectory of an electron that was traced forwards and backwards in time from  $x = -12R_E, y = 0.5R_E, z = 0$ , at  $t = 6.8$  min. At the start time,  $W_k = 101.25$  keV and pitch angle  $\alpha_{eq} = 90^\circ$ . Colors indicate the cross-tail electric field for  $t = 7$  min. The numbers at circles indicate the time when the particle passed various locations.



**Figure 5.2** Variations of  $W_k$ ,  $B_z$ , and  $E_y$  along the trajectory versus time in (a) and versus  $x$  in (b), (c) magnetic moment  $\mu$  versus time, (d) mirror point  $z$  versus time.

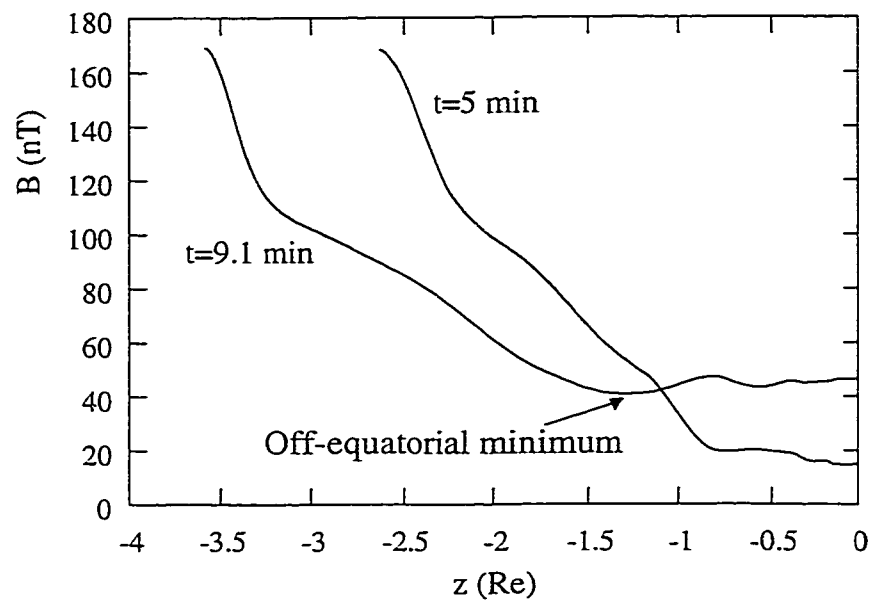
the acceleration process was adiabatic for most of the trajectory, except for the early cross-tail drift in the far tail, as shown in Figure 5.2(c).

Figure 5.2(c) shows that the first adiabatic invariant was broken at the beginning of the particle trajectory, near the neutral line where the magnetic curvature radius was comparable to the particle gyro-radius.

Figure 5.2(d) illustrates the complexity of the electron bounce motion. The dynamic MHD fields produced off-equatorial magnetic field minima, associated with MHD waves on the dipolarizing field lines. This resulted in bounce motion about off-equatorial bounce centers for  $t$  between approximately 8.5 and 9.5 min. Figure 5.3 illustrates the magnetic field values along the field lines for  $t = 9.1$  min and 5 min when the electron bounce center changed to the off-equatorial minimum from the equator. The second invariant is clearly broken during periods of off-equatorial bounce motion. These violations of the invariants are important for correctly calculating the particle trajectory, although they do not have a dramatic effect on the energy gain.

The loops in the orbit in Figure 5.1 resulted from gradient drift about a peak in the equatorial magnetic field. Figure 5.4 shows local peaks in the equatorial magnetic field formed at different times that seem to be associated with the loops in the particle trajectory. Of course, it is not possible to cleanly identify a trajectory loop with one local  $B_z$  peak at a certain time, because the magnetic field itself evolved rapidly as the electron drifted. The corresponding magnetic field gradient, which points toward the local peak in  $B$ , results in  $\nabla B$  drift around in a loop. As we will see, these loops turn out to be important features for particles that gain the most energy.

To better understand the characteristics of loops in the electron orbits we compare two electron orbits, one with a loop and one without. Figure 5.5(a) shows the equatorial crossing points of the two trajectories. Particle drift motion primarily consists of curvature drift,  $\mathbf{E} \times \mathbf{B}$  drift, and the  $\nabla B$  drift.  $\nabla B$  drift is most important when the electron motion is close to the equatorial plane and the electric field is relatively small. In trajectory (1), the drift direction was significantly affected by the changes in the magnetic field gradient, which occurred when the electron passed a local bump in the magnetic field configuration. A loop appeared in orbit (1) at  $t \approx 5$  min. The plot of energy versus  $x$  along the trajectory in Figure 5.5(b) shows that the electron



**Figure 5.3** Magnetic field values along the field lines for  $t = 5 \text{ min}$  and  $9.1 \text{ min}$  versus  $z$ . An electron can be trapped temporarily in off-equatorial magnetic minima during an off-equatorial bounce motion for  $t = 9.1 \text{ min}$ .

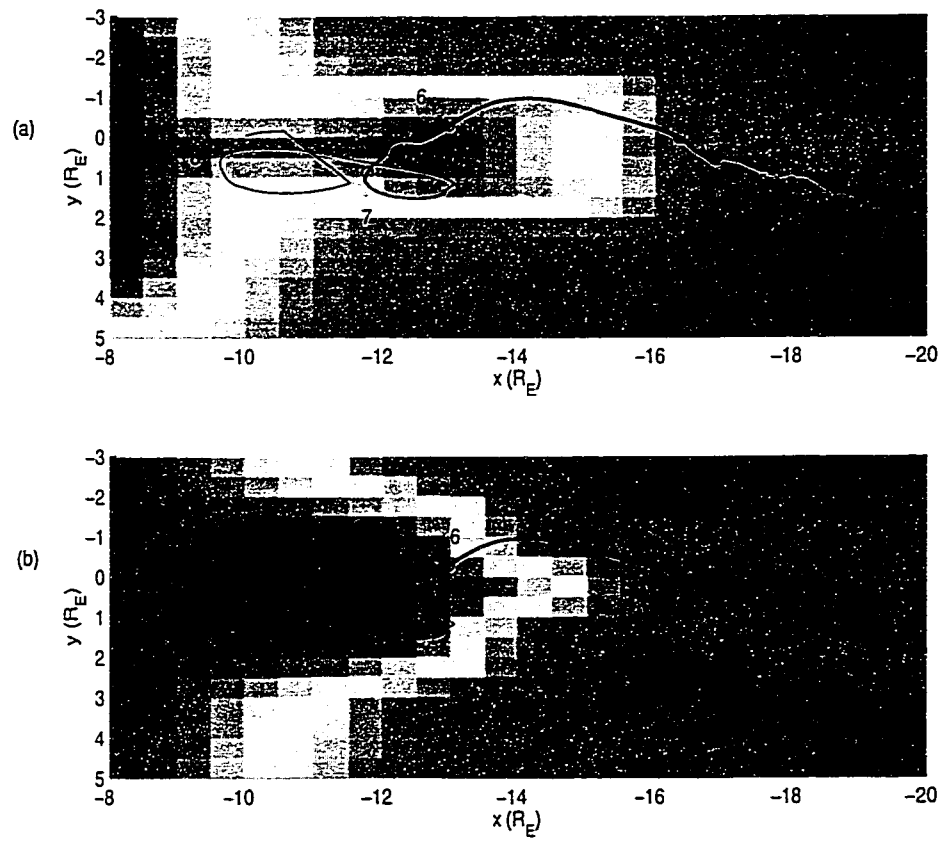


**Figure 5.4** Part of the trajectory in Figure 5.1, but now colors indicate the equatorial magnetic field for  $t = 7$  min in (a) and  $t = 8$  min in (b).

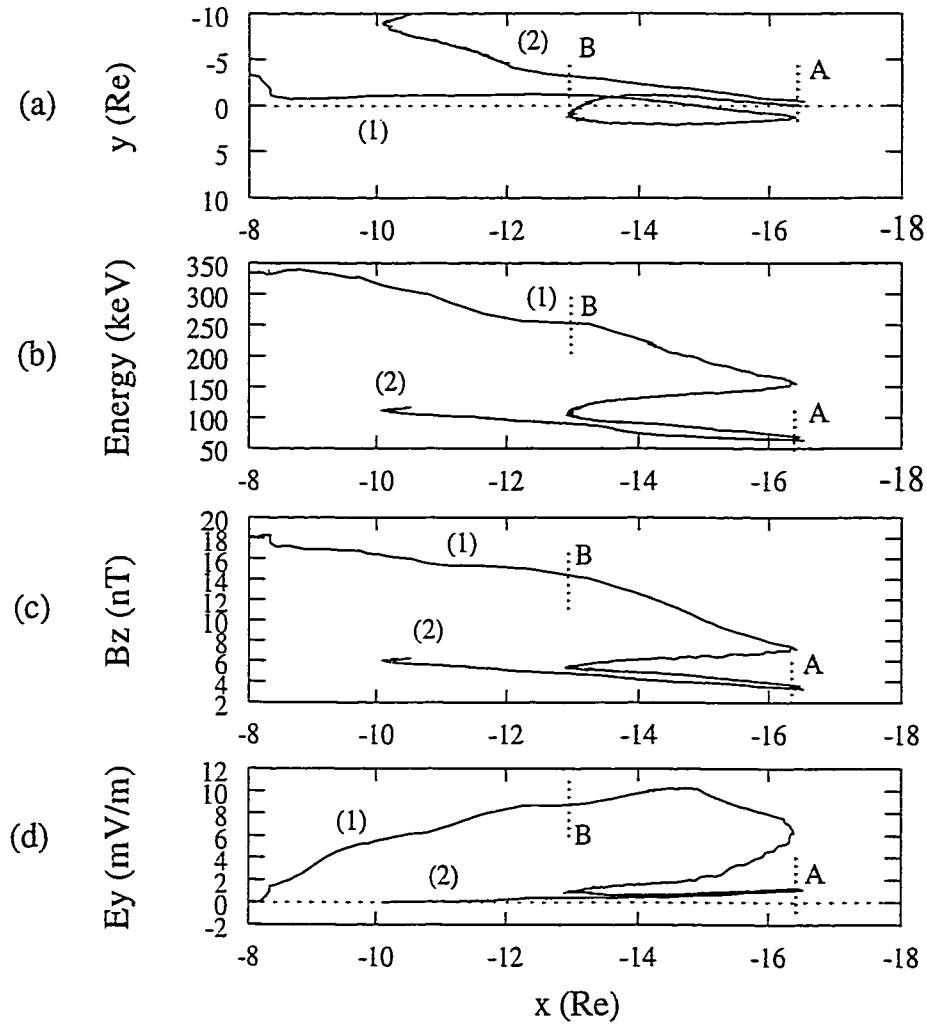


**Figure 5.5** (a) An equatorial crossing trajectory with a loop is labelled as (1), one without a loop as (2). Both traced particles started with  $x = -15.5 R_E$ ,  $\mu = 0.02$  MeV/nT,  $\alpha_{eq} = 90^\circ$ , and  $t = 5$  min. However, their initial  $y$ -positions differed by  $0.5 R_E$ . (b) Energy versus  $x$ , (c)  $B_z$  versus  $x$ , and (d)  $E_y$  versus  $x$  along the trajectory. A and B indicate the end points of a loop in the electron orbit.

gained more than half of its total energy between points A to B, the end points of the loop. The rest of the energy gain occurred during the earthward radial transport from point B to the end of the trajectory. The corresponding  $B_z$  and  $E_y$  values are shown in Figure 5.5(c) and (d) respectively. The orbit (1) electron experienced strong electric and magnetic fields during the rapid acceleration. On the other hand, the orbit (2) electron never entered the region of strong dipolarization and so simply drifted to the dawn side boundary with little energization.

In order to gain as much energy as possible from a substorm and to be transported from near the X-line to the trapping region inside  $10 R_E$ , an electron must spend as much time as possible in the region of the strong induction field. Loop trajectories help an electron to remain longer in that region and thus gain more energy. Although the MHD field model we adopted in this work is not expected to represent the substorm field configuration exactly, it seems likely that local maxima in equatorial field strength occur in nature.

Although the test particle tracing shown in Figures 5.1 and 5.2 ended at  $x \sim -10R_E$ , because the MHD simulation ended at that time, a real electron will undergo a subsequent radial transport, unless it immediately drifts through the magnetopause. Could the electron shown in Figures 5.1 and 5.2 be transported into a trapping region and reach geosynchronous orbit? In order to answer the question conclusively, we would need to continue to follow the electron in the evolving electric and magnetic fields. However, lacking a 3-dimensional dynamic magnetic field model that includes the dayside and inner regions of the magnetosphere, we cannot simulate the subsequent acceleration and transport. In this work, we will just assume that the electron that was substorm-injected to about  $10 R_E$  can be trapped in a field configuration which is moderately disturbed. Such an electron has a good chance of being gradually transported into the inner magnetosphere, unless it is lost to the atmosphere through pitch angle scattering. If the electron conserves its first invariant  $\mu$  during that radial transport, one can estimate the electron energy at the final location. For example, the electron described by Figure 5.1, which has an energy of about 390 keV at  $x = -10$  in a field strength of 45 nT, will have about 720 keV at geosynchronous orbit, where the field strength is about 100 nT and about 900 keV at  $L = 6$ , where the field strength is about 144 nT. Consequently, an electron of  $\sim 20$  keV energy initially located near

the X—line may be injected into the near geosynchronous region with an energy gain of about a factor of 45.

## 5.2 Estimation of the number of relativistic electrons generated in a substorm

Having found that some electrons are greatly energized during the substorm dipolarization, the next question is whether the process can generate a sufficient number of such electrons to provide an observed flux increase in the inner magnetosphere. There are at least two theoretical approaches to estimating the flux of inner magnetospheric relativistic electrons that can be generated by the magnetic reconfiguration that occurs during a substorm: (i) Connect the plasma sheet distribution function to the inner magnetospheric distribution function by Liouville's theorem. (ii) Calculate the number of electrons that a substorm can create with magnetic moments in the outer-belt relativistic electron range and compare that to the number required to match the high fluxes observed in the recovery phase of a magnetic storm.

### *Estimation of the electron fluxes using Liouville's theorem*

The estimation proceeds in two steps: 1. Calculate the electron flux at  $x \sim -10R_E$  after substorm-associated injection from the tail. 2. Transform the electron flux to the value at geosynchronous orbit, assuming that the radial transport conserves the first invariant.

The plasma sheet electron spectrum can be represented by a kappa distribution [Christon *et al.*, 1991] given as :

$$j = j_o \frac{E}{\left(1 + \frac{E}{\kappa E_o}\right)^{1+\kappa}} \quad (5.1)$$

The values of  $j_o$ ,  $\kappa$ , and  $E_o$  vary with conditions, with harder spectra being observed in more active conditions. Since relativistic electrons are observed following substantial magnetic storms, we choose values near the hard end of the range reported by [Christon *et al.*, 1991]:  $j_o = 5.5 \times 10^6 \text{cm}^{-2}\text{s}^{-1}\text{sr}^{-1}\text{keV}^{-1}$ ,  $\kappa = 3.5$ , and  $E_o = 1.14 \text{keV}$ . From Liouville's theorem and the relation between the phase space density and the

differential flux, i.e.,  $f = j/p^2$ , where  $p$  is relativistic momentum, we have

$$j_2 = \frac{p_2^2}{p_1^2} j_1 \quad (5.2)$$

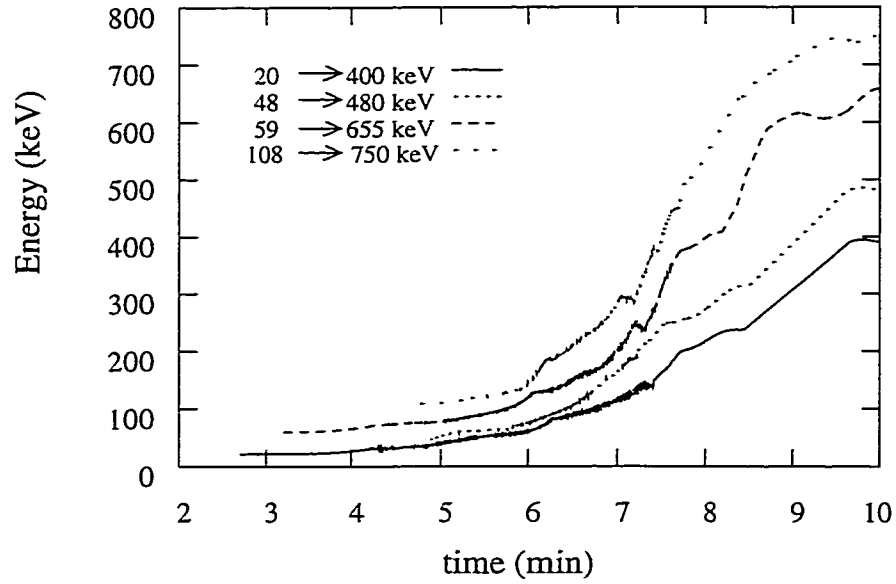
where the subscripts 1 and 2 represent values before and after the transport respectively for each step of the calculation. For step 1, the electron flux,  $j_2$ , after the substorm injection to  $x = -10R_E$  is calculated using Equation (5.1) and the energy gain (or momentum  $p_2$ ) obtained from the simulation. For step 2, we assume adiabatic radial transport to geosynchronous orbit. The electron flux  $j_2$ , after betatron acceleration to  $x = -6.6R_E$  is calculated from the initial electron flux calculated in the step 1 and the final energy (or momentum  $p_2$ ) determined from  $\mu$  conservation.

Figure 5.6 illustrates energy gains when plasma sheet electrons with initial energies of 20, 48, 59, 108 keV are injected to the outer magnetosphere ( $r \sim 10R_E$ ) from  $x = -20R_E$ . During the injection associated with the substorm reconfiguration, the electrons are accelerated up to several hundreds of keV. For the subsequent adiabatic radial diffusion to geosynchronous region, they are accelerated to relativistic energies. The energies at geosynchronous orbit,  $E_2$ , can be calculated from  $\mu$  conservation as follows:

$$E_2 = -mc^2 + \sqrt{m^2c^4 + \frac{B_2}{B_1}(E_1^2 + 2mc^2E_1)}. \quad (5.3)$$

For the magnetic field strengths,  $B_1 = 45$  nT at  $x = -10R_E$  and  $B_2 = 100$  nT at  $x = -6.6R_E$ , the electron energies become 707, 854, 1133, and 1282 keV, respectively. Figure 5.7 exhibits the electron fluxes calculated in the way described above for the four initial energies. The theoretical fluxes at the geosynchronous radius for particles with the largest energy gain are up to  $\sim 10000$  times greater than observed values. Thus the phase space density of selected plasma sheet electrons may be sufficient to supply the electrons at the geosynchronous region. However this number is strongly dependent on the particle initial conditions and an undetermined number of other plasma sheet electrons are lost from the magnetotail.

One disadvantage of using Liouville's theorem to estimate inner magnetospheric fluxes is that the relativistic electrons drift fast enough that we would expect their distribution function to have substantial fine structure, with substorm generated electrons from the tail very close, in phase space, to electrons with different histories. Using Liouville's theorem to relate the tail and inner magnetosphere may therefore



**Figure 5.6** Energy gains of four sample plasma sheet electrons with initial energies of 20, 48, 59, and 108 keV during the substorm injection to  $x \sim -10R_E$  from  $x \sim -20R_E$ . Initial conditions for each particles are as follows. For 20 keV,  $W_k = 101.25\text{keV}$ ,  $x_5, x = -12R_E, y = 0.5R_E, t = 6.8$  min. For 48 keV,  $W_k = 211.25\text{keV}$ ,  $x = -12R_E, y = 0.5R_E, t = 7.3$  min. For 59 keV,  $W_k = 77\text{keV}$ ,  $x = -14.5R_E, y = -1.0R_E, t = 5$  min. For 108 keV,  $W_k = 245\text{keV}$ ,  $x = -12R_E, y = 0.5R_E, t = 6.8$  min.

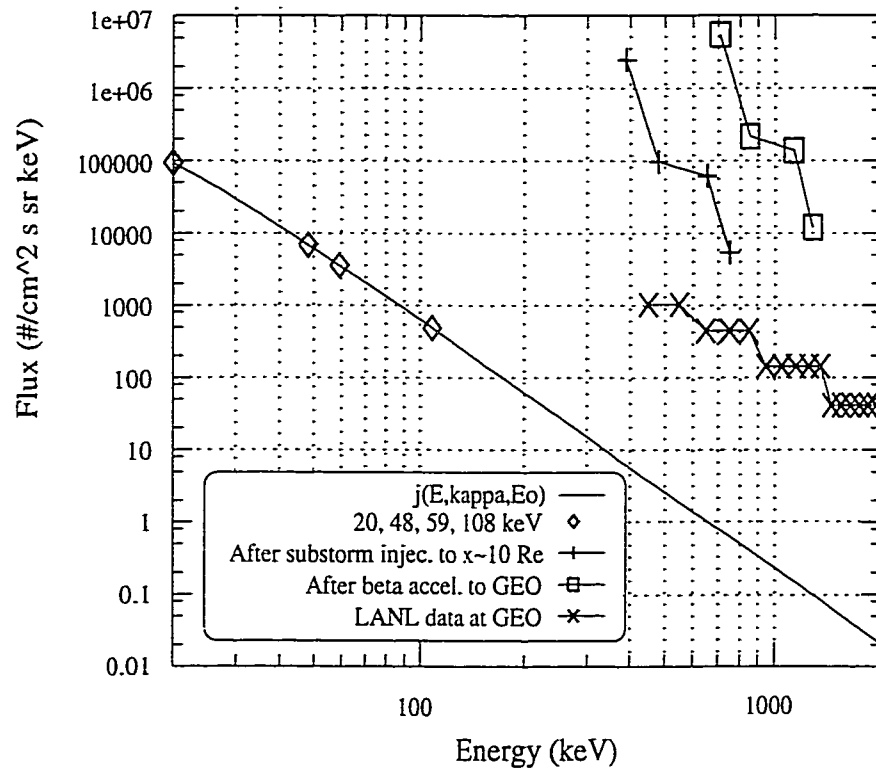


**Figure 5.7** Comparison of relativistic electron fluxes estimated using Liouville's theorem and LANL data. Plasma sheet electrons of 20, 48, 59, 108 keV energies are injected to a distance of  $\sim 10R_E$  from about  $x = -20R_E$  in the tail, with acceleration up to several hundreds of keV. They are further energized to relativistic energies ( $\sim \text{MeV}$ ) by adiabatic radial diffusion to the geosynchronous region. LANL data for November 1993 storm [Kim and Chan, 1997] are plotted for comparison.

give misleading results concerning the large-scale characteristics of the distribution function. Therefore, we also need to calculate the total number of relativistic electrons that a substorm can create (approach (ii)).

*Comparison of the number of source electrons to the number required*

We first estimate the number of MeV outer-belt electrons involved in a typical recovery phase enhancement. Because of the relationship between the distribution function and the differential flux,  $f = j/p^2$ , the number density above momentum  $p_{min}$  is given by

$$n(> p_{min}) = \int \int \int_{p>p_{min}} f d^3p = \int_{p_{min}}^{\infty} \int j d\Omega dp. \quad (5.4)$$

Since the volume of a dipole flux tube is approximately  $LR_E \times$  (equatorial cross section), we can write the total number of relativistic electrons between  $L_{min}$  and  $L_{max}$  as

$$N^{obs} \approx \int_{L_{min}}^{L_{max}} LR_E \times 2\pi LR_E^2 dL \int \int \int_{p>p_{min}} f d^3p \quad (5.5)$$

or

$$N^{obs} \approx \frac{8\pi^2 R_E^3}{3} (L_{max}^3 - L_{min}^3) \int_{p_{min}}^{\infty} \langle j \rangle dp \quad (5.6)$$

where  $\langle j \rangle$  represents an average over pitch angle and  $L$ -shell. Assume that the relevant part of the distribution function takes the simple form

$$\langle j \rangle = j_o \left( \frac{p_{min}}{p} \right)^q \quad (5.7)$$

where  $p_{min}$  is the momentum corresponding to 1 MeV. Substituting Equation (5.7) in Equation (5.6) and integrating over  $p$  gives

$$N^{obs} = \frac{8\pi^2 R_E^3}{3} (L_{max}^3 - L_{min}^3) j_o \left( \frac{p_{min}}{m_e c} \right) \frac{m_e c}{q-1} \quad (5.8)$$

For the November 1993 storm, the post-storm differential flux for 1 MeV is about  $100 \text{ cm}^{-2}\text{s}^{-1}\text{sr}^{-1}\text{keV}^{-1}$  and  $q \approx 2.45$ . Setting  $L_{max} = 7$ ,  $L_{min} = 4$ , and  $p_{min}/m_e c = 2.78$ , corresponding to 1 MeV kinetic energy, we estimate that

$$N^{obs} \sim 6 \times 10^{24}. \quad (5.9)$$

Next we estimate the number of source electrons. Figure 5.2, which shows typical source-electron trajectories, suggests that the particle's magnetic moment is approximately conserved through most of the acceleration process, though not in its earliest phase. We choose the electron shown in Figure 5.2, which winds up with a magnetic moment of about 0.012 MeV/nT and a kinetic energy of about 900 keV at  $L = 6$ , as having the minimum magnetic moment:

$$\mu_{crit} = 0.012 \text{ MeV/nT} \quad (5.10)$$

We define a prospective source electron as one that has  $\mu > \mu_{crit}$  and has a location and pitch angle that make it likely to have come from a region near the reconnection site ( $B < 1$  nT) and to lead to a trapped orbit. Once trapped about the Earth, we assume that it can be transported to  $L < 6.6$  by radial diffusion. Our orbit calculations suggest that the electrons that are most likely to be transported from the reconnection region to a trapped orbit in one substorm are those that ride the magnetic-field collapse Earthward, circling the local field maximum like electron (1) in Figure 5.5.

We write the number of source electrons as follows:

$$N_{source} = N_{substorms} \int_C B_e dA_e \int_C \frac{ds}{B} \int_C d\Omega \int_{\mu > \mu_{crit}} f p^2 dp \quad (5.11)$$

where  $N_{substorm}$  is the number of substorms that contribute to the phenomenon. The equatorial magnetic field is  $B_e$ , and  $dA_e$  is an element of area in the equatorial plane. The  $ds$ -integration covers a flux tube. The direction of particle momentum is indicated by  $d\Omega$ . The symbol  $C$  indicates integration over the region of phase space where the trajectories are trapped about the equatorial magnetic field maximum (as shown, for example, in Figure 5.4).

It is convenient to define an effective source volume

$$V = \int_C B_e dA_e \int_C \frac{ds}{B} \int_C \frac{d\Omega}{4\pi} \quad (5.12)$$

and a spectral factor

$$S = \frac{\int_{\mu > \mu_{crit}} \overline{f(E)} E^{1/2} dE}{\int_0^\infty \overline{f(E)} E^{1/2} dE} \quad (5.13)$$

The bars indicate appropriate pitch-angle averages. In writing Equation (5.13), we used a non-relativistic approximation for the plasma sheet source, assuming that the electrons become relativistic only after subsequent Earthward transport. With the definitions in Equations (5.12) and (5.13), Equation (5.11) becomes

$$N_{source} = N_{substorms} V n S \sim (2.6 \times 10^{26}) N_{substorms} \frac{V}{1 R_E^3} n (\text{cm}^{-3}) S \quad (5.14)$$

where  $n$  is the total number density of plasma-sheet electrons in the source region.

Assume that the distribution function in  $S$  is proportional to a kappa function:

$$f = \frac{K}{(1 + E/\kappa E_o)^{\kappa+1}} \quad (5.15)$$

where  $K$  is a normalization factor,

$$E_o = kT_e \left( \frac{\kappa - \frac{3}{2}}{\kappa} \right) \quad (5.16)$$

and  $3kT_e/2$  is defined to be the average energy of the distribution. The spectral factor  $S$  is then given by

$$S = \frac{\int_{E_{min}}^{\infty} \frac{E^{1/2} dE}{(1 + E/\kappa E_o)^{\kappa+1}}}{\int_0^{\infty} \frac{E^{1/2} dE}{(1 + E/\kappa E_o)^{\kappa+1}}} \quad (5.17)$$

The denominator becomes

$$\begin{aligned} \int_0^{\infty} \frac{E^{1/2} dE}{(1 + E/\kappa E_o)^{\kappa+1}} &= (\kappa E_o)^{3/2} \int_0^{\infty} x^{1/2} (1+x)^{-1-\kappa} dx \\ &= (\kappa E_o)^{3/2} \int_0^1 u^{1/2} (1-u)^{\kappa-3/2} du \\ &= (\kappa E_o)^{3/2} \frac{\sqrt{\pi} \Gamma(\kappa - 1/2)}{2\Gamma(\kappa + 1)} \end{aligned} \quad (5.18)$$

where  $u = x/(1+x)$ , and beta function is used:

$$\text{Beta Function } B(p, q) = \int_0^1 t^{p-1} (1-t)^{q-1} dt = \frac{\Gamma(p)\Gamma(q)}{\Gamma(p+q)} \quad (5.19)$$

For  $E_{min} \gg \kappa E_o$ , the numerator becomes

$$\int_{E_{min}}^{\infty} \frac{E^{1/2} dE}{(1 + E/\kappa E_o)^{\kappa+1}} = (\kappa E_o)^{3/2} \frac{1}{\kappa - 1/2} \left( \frac{kT_e}{E_{min}} \right)^{\kappa-1/2} (\kappa - 3/2)^{\kappa-1/2} \quad (5.20)$$

From Equations (5.18) and (5.20), Equation (5.17) simplifies to

$$S = \frac{2\Gamma(\kappa + 1) \left(\kappa - \frac{3}{2}\right)^{\kappa-1/2}}{\Gamma(\kappa + \frac{1}{2})\sqrt{\pi}} \left(\frac{kT_e}{E_{min}}\right)^{\kappa-1/2}. \quad (5.21)$$

If we choose  $\kappa = 3.5$  and  $kT_e = 2$  keV, corresponding to a plasma sheet electron spectrum that is on the hard end of the ones observed by *Christon et al.* [1991], and if we also choose  $E_{min} = 20$  keV, which was the initial energy of the electron shown in Figure 5.2, we find

$$S \approx 17.5 \left(\frac{kT_e}{E_{min}}\right)^3 \sim 0.0175. \quad (5.22)$$

To estimate the effective source volume  $V$ , we have followed electron trajectories starting at  $t = 5$ , from various locations near the  $B$ -field maximum. Figure 5.8(a) shows four selected electron orbits for  $\mu = 0.02$  MeV/nT,  $\alpha_{eq} = 90^\circ$ , and different starting locations. Electrons 1 and 2 spend little time near the  $B$ -field maximum and drift away from the substorm region. Electrons 3 and 4 loop around the field maximum and are swept deep into the magnetosphere, exhibiting a typical source-electron trajectory. Figure 5.8(b) illustrates the sensitive dependence on equatorial pitch angle. Only particles with pitch angles near  $90^\circ$  are trapped about the field maximum and transported to the inner magnetosphere.

Figure 5.9 illustrates the dependence on starting position and equatorial pitch angle in a systematic way. Circles indicate the region where source-electron trajectories were found, and the numbers inside the circles indicate the minimum pitch angles. The earthward boundary of the region is somewhere between  $x = -13.5$  and  $-14.0R_E$ . For the investigated sample electrons, the average minimum equatorial pitch angle  $\alpha_{min}$  is about  $75^\circ$ .

To estimate the source volume  $V$  using the results shown in Figure 5.9, we first note that the integral over solid angle in Equation (5.12) can be written

$$\int_C \frac{d\Omega}{4\pi} = \frac{1}{2} \int_{\alpha_{min}}^{\alpha_{max}} \sin \alpha d\alpha = \cos \alpha_{min} = \sqrt{1 - \frac{B(s) \sin^2 \alpha_{e,min}}{B_e}} \quad (5.23)$$

Substituting Equation (5.23) in Equation (5.12) gives

$$V = \int_C dA_e \int_{-s_{max}}^{s_{max}} ds \frac{B_e}{B(s)} \sqrt{1 - \frac{B(s) \sin^2 \alpha_{e,min}}{B_e}} \quad (5.24)$$

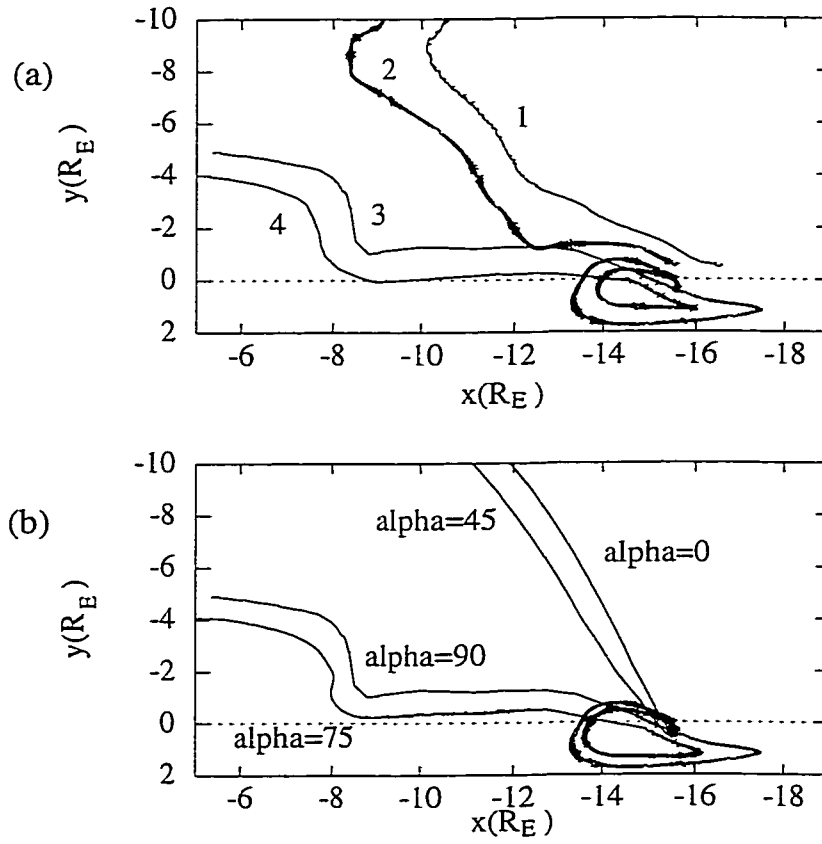


**Figure 5.8** (a) Equatorial crossing trajectories for four different starting points,  $x = -16.5, y = 0.5$  for orbit 1,  $x = -15.5, y = 0.5$  for orbit 2,  $x = -15.5, y = 0.0$  for orbit 3, and  $x = -15.5, y = -0.5$  for orbit 4, with initial values of  $\mu = 0.02$  MeV/nT,  $\alpha_{eq} = 90^\circ$ , and  $t = 5$  min. (b) Equatorial crossing trajectories with different initial pitch angles, i.e.,  $\alpha_{eq} = 0, 45^\circ, 75^\circ$ , and  $90^\circ$ , for orbit 3 (above).

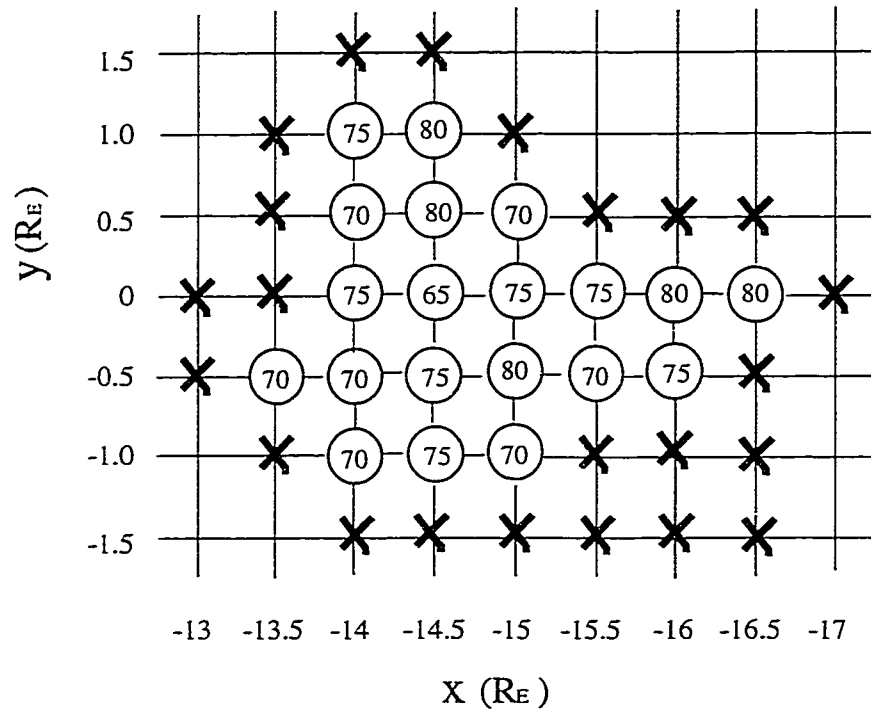


**Figure 5.9** A map of the region where source electrons are found which is indicated by circles. The numbers inside the circles indicate the minimum pitch angles for electrons that are likely undergo major energization, as discussed in the text.

By carrying out the numerical integrations indicated for the magnetic field configuration for  $t = 5$  and the values of  $\alpha_{e,min}$  shown in Figure 5.9, we find that

$$V \approx 0.06 R_E^3. \quad (5.25)$$

The volume is small because the model substorm current sheet is thin.

Substituting Equations (5.22) and (5.25) in Equation (5.14) and taking  $n = 0.5 \text{ cm}^{-3}$ , we find that

$$N_{source} \sim 1.3 \times 10^{23} N_{substorms} \quad (5.26)$$

or, comparing with Equation (5.9),

$$\frac{N_{source}}{N_{obs}} \sim 0.02 N_{substorms} \quad (5.27)$$

Our rough estimate thus suggests that the single substorm described by the simulation of *Birn and Hesse* [1996] would provide only  $\sim 0.02$  of the relativistic electrons needed to produce a typical killer-electron event, even assuming an electron temperature that is at the high end of the observed range. And it should be emphasized the number in Equation (5.27) is extremely sensitive to the assumed electron temperature.

Of course, we would not want our model to predict that every substorm will produce a major enhancement of the outer belt. We are comfortable with the fact that our estimates of source strength are “borderline” and that we have to call upon a series of substorms and/or an unusually strong substorm, to produce a major enhancement in the belts.

It should be noted that Equation (5.27) estimates the number of electrons with  $\mu > 0.012$  delivered to  $x \approx -10 R_E$ . Radial diffusion will transport only a fraction of that number to geosynchronous orbit. On the other hand, our estimate of  $N_{source}$  is conservative in several respects:

- Our model substorm has a width  $\Delta y \sim 3 R_E$  at a distance of  $\sim 15 R_E$  from Earth which corresponds to  $\sim 0.8$  hr of local time. A big substorm—the kind that really injects the storm-time ring current—is likely to be significantly wider. Thus our estimate of the source volume  $V$  may be a substantial underestimate for some substorms that occur in a major storm.

- If the substorm region had greater  $y$  extent, it will take an electron longer to drift across the substorm-disturbed region (mostly by gradient/curvature drift). Perhaps some electrons can be swept to the inner magnetosphere even if they do not circle a local peak in equatorial field strength. Thus the number of source electrons may actually increase with at a greater-than-linear rate with  $\Delta y$ .
- We implicitly assumed that an electron that leaves from the collapsing-field region and resumes its cross-tail drift will escape from the magnetosphere and never become part of the outer radiation belt. However, that is not necessarily true. Some of those “lost electrons” may actually get trapped on outer-magnetospheric Earth-circling orbits that cross the dayside mirroring in the polar cusp. Such particles would have many chances at experiencing another substorm as they repeatedly cross the nightside.

### 5.3 Summary and Discussion

We have studied a substorm-associated acceleration mechanism, based on tracing test particles in three-dimensional MHD simulations of substorm dipolarization. We used electric and magnetic fields obtained from the MHD simulations by *Birn and Hesse* [1996]. Test particles were traced both forwards and backwards in time, starting from a time and location where the magnetic field was rapidly evolving and the induction electric field was strong.

The essential results of our calculations are the following:

1. Following test-particle electrons through an MHD simulation of a substorm, we found that some electrons can be accelerated from  $\sim 20$  keV in a 1 nT field at  $x \sim -20R_E$  to  $\sim 400$  keV in a 45 nT field at  $x \sim -10R_E$ . If such an electron is later transported earthward to  $L \sim 6$  by radial diffusion which conserves the first invariant, it will have  $\sim 1$  MeV energy and contribute to the outer-belt relativistic-electron population. The radial diffusion from  $L \sim 10$  to  $L \sim 6$  was not considered in detail in this work but merely assumed to occur.
2. Both adiabatic invariants are strongly violated in the weak-field region near the X-line. However, the first invariant is approximately conserved in the region nearer the Earth where most of the acceleration takes place.

3. In the stronger-field region where the first invariant is conserved, an electron can violate its second invariant, particularly when it mirrors temporarily about an off-equatorial field-strength minimum.

4. The particle gains most of its energy well earthward of the neutral line, in the region of collapsing magnetic field and strong westward induction electric field.

5. The value of the distribution function for 20 keV plasma-sheet electrons is larger than the value for MeV electrons observed at geosynchronous orbit during an injection event. Thus the idea that substorms generate outer-belt MeV electrons passes the simplest test with Liouville's theorem.

6. The number of prospective killer electrons produced in the single modest substorm described by the MHD simulation is too small, by a factor  $\sim 50$ , to produce a typical killer-electron event, even if we assume a plasma sheet electron temperature that is at the high end of the observed range. However, it seems likely that a sequence of substorms, some of them significantly larger than the simulated event, could produce a sufficient number of electrons.

The particle dynamics and the energy gain are sensitive to the magnitude and the cross tail extent of the induction electric field  $E_y$ . The simulated substorm used in this study represented an event of moderate size. A large, strong substorm could be more effective in producing MeV electrons in the inner magnetosphere, possibly including direct injection to the geosynchronous region in extreme cases. Further test particle simulations with substorms of different sizes would advance our understanding of this mechanism. Also, more work is needed to better justify our assumption that enhanced radial diffusion can transport electrons from the outer trapped region to the inner magnetosphere on time scales of about one day.

## Chapter 6

### Summary and Discussion

Relativistic electron fluxes in the outer radiation belt are highly dynamic, especially during geomagnetically active times. Intense electron fluxes are hazardous to spacecraft electronic systems and to astronauts who will work in space constructing the International Space Station. Because of these practical concerns, understanding and predicting variations in relativistic electron fluxes has recently become one of the most important problems in magnetospheric physics. The work presented in this thesis was thus motivated by practical concerns as well as academic interest.

This work focused primarily on electron events that often occur associated with high speed solar wind streams. This type of event occurs with relatively regular 27-day periodicity during the declining phase of the solar cycle. The next declining phase is expected to occur between years 2002 and 2007, and many high-speed-stream events are expected in that interval. Typically, the relativistic electron flux at geosynchronous orbit decreases by orders of magnitude when a magnetic storm develops and increases to about  $10 - 10^2$  times the prestorm fluxes on a time scale of about one day during the recovery phase of the storm. To understand the physical mechanisms responsible for the relativistic electron flux variations, we examined two physical processes: the *fully-adiabatic* effect and the *delayed substorm injection* process.

Particle fluxes change in a fully adiabatic manner when the particles are subjected to slow changes in magnetic fields, so that all three adiabatic invariants are conserved. Specifically, all three adiabatic invariants are conserved when the time scale for variations in the magnetic field is much longer than the particle drift time. We simulated fully-adiabatic electron fluxes for the special case of equatorially-mirroring electrons. We used Rice magnetic field models and a quiet-time electron flux model constructed from CRRES spacecraft data. For a storm with a minimum *Dst* value of approximately  $-100$  nT, we found that the fully-adiabatic effect can cause a flux decrease as much as almost 2 orders of magnitude, consistent with observed flux decreases. Overall we conclude that the fully adiabatic effect can account for a significant frac-

tion of observed flux decreases and that differences between the observed and the fully adiabatic fluxes help to clarify when and where additional loss and source mechanisms exist. Possibilities for further extension of this work include (1) Extension to non-equatorially mirroring electrons and comparison with observed pitch angle distributions, and (2) Incorporation of the effects of solar wind conditions to vary standoff distances in the field model and tilt of the Earth's magnetic field.

We also simulated acceleration and injection of plasma sheet electrons during substorms using a 3-dimensional dynamic MHD field model. The test particle traces showed that tens-of-keV plasma sheet electrons can be accelerated up to several hundreds of keV during a substorm, as the particles are transported from  $x \sim -20R_E$  to  $x \sim -10R_E$ . We assume that the particles are subsequently accelerated to relativistic energies during subsequent diffusive transport to geosynchronous region, conserving their first invariants. During the substorm injection, a prospective radiation-belt electron gains most of its energy in the region of strong westward induction electric field. The first and second adiabatic invariants are broken to a moderate extent during the process.

Estimation of the number of accelerated plasma sheet electrons indicates that a single moderate substorm cannot produce enough energetic electrons to explain a typical relativistic-electron event. However, the numbers are very sensitive to electron temperature and to the assumed size of the substorm. Our study suggests that a series of substorms, some of them large, may be capable of producing such an enhancement. More work is needed to improve the estimates and also to illuminate the physics of the diffusive process that we have assumed to transport electrons from  $x \sim -10R_E$  to  $x \sim -6R_E$ . Test particle simulations with various sizes of substorms is also an important remaining work to advance our understanding on this mechanism.

The overall conclusion of our study is that the fully-adiabatic effect and the delayed substorm injection mechanism may account for a significant fraction of the relativistic electron flux variations that are observed during a typical relativistic electron event. However, more extensive observational and theoretical work will be required to fully understand the storm-time flux variations of outer-belt relativistic electrons.

When we can conclusively identify physical mechanisms responsible for the flux variations, we will hopefully be able to predict those variations. That is indeed a

major long-range goal of this area of magnetospheric physics. This thesis represents a step toward that goal.

## Bibliography

Baker, D., et al., A strong CME-related magnetic cloud interaction with the Earth's magnetosphere: ISTP observations of rapid relativistic electron acceleration on May 15, 1997, *Geophys. Res. Lett.*, *25*(15), 2975, 1998a.

Baker, D. N., P. R. Higbie, E. W. Hones, Jr., and R. D. Belian, High-resolution energetic particle measurements at 6.6  $r_e$ , 3, low-energy electron anisotropies and short-term substorm predictions radiation zone?, *J. Geophys. Res.*, *83*, 4863, 1978.

Baker, D. N., J. B. Blake, R. W. Klebesadel, and P. R. Higbie, Highly relativistic electrons in the Earth's outer magnetosphere 1. Lifetimes and temporal history 1979–1984, *J. Geophys. Res.*, *91*, 4265–4276, 1986.

Baker, D. N., J. B. Blake, L. B. Callis, R. Belian, and T. E. Cayton, Relativistic electrons near geostationary orbit: evidence for internal magnetospheric acceleration, *Geophys. Res. Lett.*, *16*, 559, 1989.

Baker, D. N., J. B. Blake, L. B. Callis, J. R. Cummings, D. Hovestadt, S. Kanekal, B. Klecker, R. A. Mewaldt, and R. D. Zwickl, Relativistic electron acceleration and decay time scales in the inner and outer radiation belts: SAMPEX, *Geophys. Res. Lett.*, *21*, 409, 1994a.

Baker, D. N., S. Kanekal, J. B. Blake, B. Klecker, and G. Rostoker, Satellite anomalies linked to electron increase in the magnetosphere, *EoS, Trans. AGU*, *75*(35), 401, 1994b.

Baker, D. N., et al., Recurrent geomagnetic storms and relativistic electron enhancements in the outer magnetosphere: ISTP coordinate measurements, *J. Geophys. Res.*, *102*, 14,141, 1997a.

Baker, D. N., X. Li, J. B. Blake, and S. G. Kanekal, Strong electron acceleration in the Earth's magnetosphere, *Adv. Space Sci.*, *in press*, 1997b.

Baker, D. N., et al., Coronal mass ejections, magnetic clouds, and relativistic magnetospheric electron events: ISTP, *J. Geophys. Res.*, *103*(A8), 17279, 1998b.

Belian, R. D., D. N. Baker, P. R. Higbie, and E. W. H. Jr., Timing of energetic proton enhancements relative to magnetospheric substorm activity and its implication for substorm theories, *J. Geophys. Res.*, *86*, 1415–1421, 1981.

Birn, J., and M. Hesse, Details of current disruption and diversion in simulations of magnetotail dynamics, *J. Geophys. Res.*, *101*(A7), 15345–15358, 1996.

Birn, J., M. F. Thomsen, J. E. Borovsky, G. D. Reeves, D. J. McComas, and R. D. Belian, Substorm ion injections: Geosynchronous observations and test particle orbits in three-dimensional dynamic MHD fields, *J. Geophys. Res.*, *102*, 2325–2341, 1997.

Birn, J., M. F. Thomsen, J. E. Borovsky, G. D. Reeves, D. J. McComas, R. D. Belian, and M. Hesse, Substorm electron injections: Geosynchronous observations and test particle simulations, *J. Geophys. Res.*, *103*(A5), 9253, 1998.

Blake, J. B., M. S. Gussenhoven, E. G. Mullen, and R. W. Fillius, Identification of an unexpected space radiation hazard, *IEEE Trans. Nucl. Sci.*, *39*, 1761–1764, 1992.

Brautigam, D. H., M. S. Gussenhoven, and E. G. Mullen, Quasi-static model of outer zone electrons, *IEEE Trans. Nucl. Sci.*, *39*, 1797–1803, 1992.

Büchner, J., and L. M. Zelenyi, Regular and chaotic charged particle motion in magnetotaillike field reversals 1. basic theory of trapped motion, *J. Geophys. Res.*, *94*, 11821, 1989.

Burton, R. K., R. L. McPherron, and C. T. Russell, An empirical relationship between interplanetary conditions and dst, *J. Geophys. Res.*, *80*, 4204, 1975.

Chan, A. A., and M. K. Hudson, Phase-space structure of drift-resonant interactions between relativistic electrons and hydromagnetic waves, 1998.

Christon, S. P., D. J. Williams, D. G. Mitchell, C. Y. Huang, and L. A. Frank, Spectral characteristics of plasma sheet ion and electron populations during disturbed geomagnetic conditions, *J. Geophys. Res.*, *96*, 1–22, 1991.

Dessler, A. J., and R. Karplus, Some effects of diamagnetic ring currents on Van Allen radiation, *J. Geophys. Res.*, *66*, 2289–2295, 1961.

Dichter, B. K., and F. A. Hanser, Development and use of data analysis procedure for the crres payloads afgl-701-2/dosimeter and afgl-701-4/fluxmeter and application of the data analysis results to improve the static and dynamic models of the earth's radiation belts, Tech. Rep. GL-TR-89-0284, Geophysics Laboratory, 1989.

Ding, C., Analytical and numerical modeling of the electromagnetic structure of geospace, Ph.D. thesis, Rice University, 1995.

Ding, C., T. W. Hill, and F. R. Toffoletto, Improvement of the Toffoletto-Hill open magnetosphere model, in *Physics of Space Plasmas (1995)*, no. 14, pp. 639–644. Editors T. S. Chang and J. R. Jasperse. MIT, 1996.

Freeman, J. W., T. P. O'Brien, A. A. Chan, and R. A. Wolf, Energetic electrons at geostationary orbit during the November 3-4, 1993 storm: Spatial/temporal morphology, characterization by a power-law spectrum and representation by an artificial neural network, *J. Geophys. Res.*, *103*, 26251, 1998.

Fujimoto, M., and A. Nishida, Monte Carlo simulation of energization of Jovian trapped electrons by recirculation, *J. Geophys. Res.*, *95*, 3841–3853, 1990.

Gussenhoven, M. S., E. G. Mullen, D. H. Brautigam, E. Holeman, and C. Jordan, Preliminary comparison of dose measurements on CRRES to NASA model predictions, *IEEE Trans. Nucl. Sci.*, *38*, 1655, 1991.

Hilmer, R. V., Analytical and numerical modeling of the electromagnetic structure of geospace, Ph.D. thesis, Rice University, 1989.

Hilmer, R. V., and G. H. Voigt, A magnetospheric magnetic field model with flexible current systems driven by independent physical parameters, *J. Geophys. Res.*, *100*(A4), 5613–5626, 1995.

- Hudson, M. K., S. R. Elkington, J. G. Lyon, V. A. Marchenko, I. Roth, and et al, Simulation of radiation belt formation during sudden storm commencements, *J. Geophys. Res.*, *101*, 14087, 1997.
- Hudson, M. K., V. A. Marchenko, I. Roth, M. Temerin, J. B. Blake, and M. S. Gussenhoven, Radiation belt formation during sudden storm commencements and loss during main phase, *Adv. Space Res.*, *21*(4), 597–607, 1998.
- Hyman, J. M., Accurate monotonicity preserving cubic interpolation, *SIAM J. Sci. Stat. Comput.*, *4*, 645, 1983.
- Kahler, S. W., Solar flares and coronal mass ejection, *Annu. Rev. Astron. Astrophys.*, *30*, 113, 1992.
- Kim, H.-J., and A. A. Chan, Fully-adiabatic changes in storm-time relativistic electron fluxes, *J. Geophys. Res.*, *102*, 22107–22116, 1997.
- Li, X., M. K. Hudson, A. A. Chan, and I. Roth, Loss of ring current  $O^+$  ions due to interaction with Pc 5 waves, *J. Geophys. Res.*, *98*, 215–231, 1993.
- Li, X., D. N. Baker, M. Temerin, and J. B. Blake, SAMPEX observations of outer zone electrons November 3–4, 1993, Presented at the Chapman Conference on Magnetic Storms, JPL, February 12–16, 1996, 1996.
- Li, X., D. N. Baker, M. Temerin, D. Larson, R. P. Lin, G. D. Reeves, M. Looper, S. G. Kanekal, and R. A. Mewaldt, Are energetic electrons in the solar wind the source of the outer radiation belt?, *Geophys. Res. Lett.*, *24*, 923, 1997a.
- Li, X., et al., Multisatellite observations of the outer zone electron variation during the November 3–4, 1993, magnetic storm, *J. Geophys. Res.*, *102*, 14,123, 1997b.
- Li, X., et al., Energetic electron injections into the inner magnetosphere during the January 10–11, 1997, magnetic storm, *Geophys. Res. Lett.*, *25*(14), 2561, 1998.
- McIlwain, C. E., Ring current effects on trapped particles, *J. Geophys. Res.*, *71*, 3623–3628, 1966.

- Nagai, T., Space weather forecast: prediction of relativistic electron intensity at synchronous orbit, *Geophys. Res. Lett.*, *15*(5), 425–428, 1988.
- Nishida, A., Outward diffusion of energetic particles from the Jovian radiation belt, *J. Geophys. Res.*, *81*, 1771–1773, 1976.
- Nishida, A., IMF control of the Earth's magnetosphere, *Space Sci. Rev.*, *34*, 185, 1983.
- Paulikas, G. A., and J. B. Blake, Modulation of trapped energetic electron at 6.6  $R_E$  by the direction of the interplanetary magnetic field, *Geophys. Res. Lett.*, *3*, 277–280, 1976.
- Paulikas, G. A., and J. B. Blake, Effects of the solar wind on magnetospheric dynamics: Energetic electrons at the synchronous orbit, in *Quantitative Modeling of Magnetospheric Processes*, edited by W. P. Olson, vol. 21 of *AGU Geophysical Monograph Series*, pp. 180–202. American Geophysical Union, 1979.
- Reeves, G. D., et al., The relativistic electron response at geosynchronous orbit during the January 1997 magnetic storm, *J. Geophys. Res.*, *103*, 17559, 1998.
- Rinaldi, M. A., R. W. Nightingale, Y. T. Chiu, and M. Schulz, Short-term response of outer-belt relativistic electrons to *Dst* variations, *EoS, Trans. AGU*, *75*(44), 545, 1994.
- Roederer, J. G., *Dynamics of Geomagnetically Trapped Radiation*, vol. 2 of *Physics and Chemistry in Space*. Springer-Verlag, 1970.
- Rostoker, G., S. Skone, and D. N. Baker, On the origin of relativistic electrons in the magnetosphere associated with geomagnetic storms, *Geophys. Res. Lett.*, *25*(19), 3701, 1998.
- Schulz, M., and L. Lanzerotti, *Particle Diffusion in the Radiation Belts*. Springer-Verlag, New York, 1974.
- Sergeev, V. A., M. A. Shukhtina, R. Rasinkangas, A. Korth, G. D. Reeves, H. J. Singer, M. F. Thomsen, and L. I. Vagina, Event study of deep energetic particle injections during substorm, *J. Geophys. Res.*, *103*, 9217, 1998.

Sheldon, R. B., H. E. Spence, J. D. Sullivan, T. A. Fritz, and J. Chen, The discovery of trapped energetic electrons in the outer cusp, *Geophys. Res. Lett.*, *25*(11), 1825, 1998.

Spjeldvik, W. N., and P. L. Rothwell, The radiation belts, in *Handbook of Geophysics and The Space Environment*. Editor A. S. Jursa., 4th edn., 1985.

Su, S. Y., and A. Konradi, Magnetic field depressions at the earth's surface calculated from the relationship between the size of the magnetosphere and the *dst* values, *J. Geophys. Res.*, *80*, 195–199, 1975.

Sugiura, M., Quiet time magnetospheric field depression at 2.3–3.6  $R_e$ , *J. Geophys. Res.*, *78*, 3182–3185, 1973.

Summers, D., R. M. Thorne, and F. Xiao, Relativistic theory of wave-particle resonant diffusion with application to electron acceleration in the magnetosphere, *J. Geophys. Res.*, *103*(9), 20,487, 1998.

Temerin, M., I. Roth, M. K. Hudson, and J. R. Wygant, New paradigm for the transport and energization of radiation belt particles, *EoS, Trans. AGU*, *75*(44), 538, 1994.

Thorne, R. M., and C. F. Kennel, Relativistic electron precipitations during magnetic storm main phase, *J. Geophys. Res.*, *76*, 4446–4453, 1971.

Vampola, A. L., Electron pitch angle scattering in the outer zone during magnetically disturbed times, *J. Geophys. Res.*, *76*, 4685–4688, 1971.

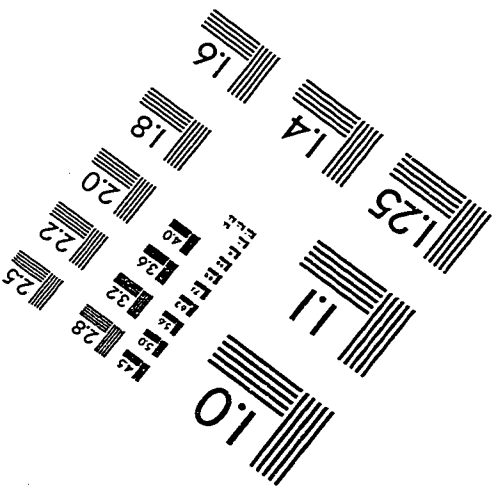
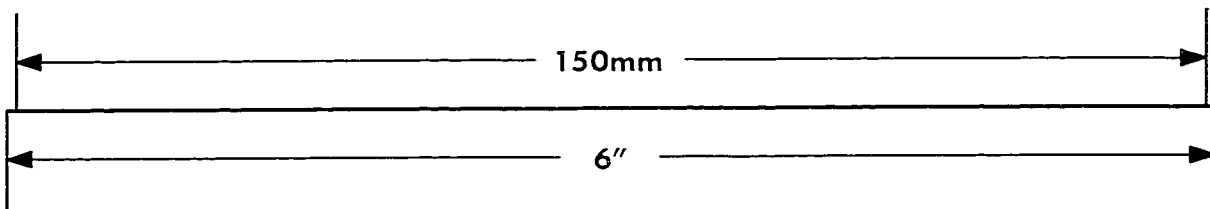
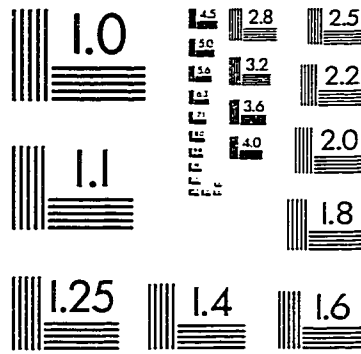
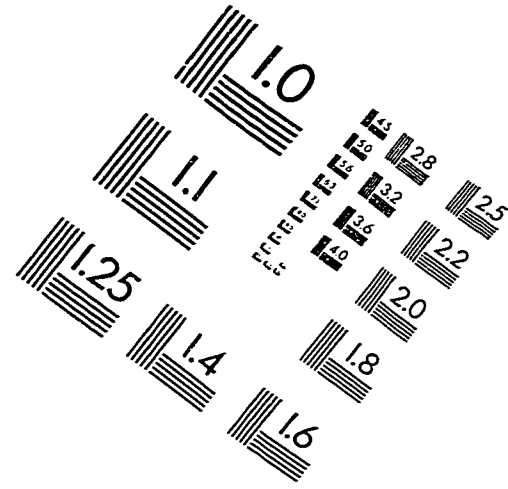
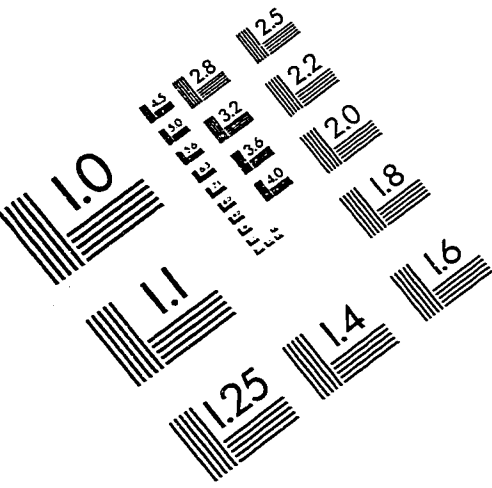
Vampola, A. L., J. V. Osborn, and B. M. Johnson, CRRES magnetic electron spectrometer AFGL-701-5A(MEA), *J. Spacecraft Rockets*, *29*, 592–595, 1992.

Voigt, G.-H., Influence of the interplanetary magnetic field on the position of the dayside magnetopause, in *Magnetospheric boundary layers*, edited by B. Battrock, pp. 315–321. ESA SP-148, Paris, 1979.

Williams, D. J., A 27-day periodicity in outer zone trapped electron intensities, *J. Geophys. Res.*, *71*(7), 1815–1826, 1966.

Williams, D. J., J. F. Arens, and L. J. Lanzerotti, Observations of trapped electrons at low and high altitudes, *J. Geophys. Res.*, 73(17), 5673–5696, 1968.

# IMAGE EVALUATION TEST TARGET (QA-3)



APPLIED IMAGE, Inc  
1653 East Main Street  
Rochester, NY 14609 USA  
Phone: 716/482-0300  
Fax: 716/288-5989

© 1993, Applied Image, Inc., All Rights Reserved

